WEAR OF ALUMINIUM MMCs

AGAINST AUTOMOBILE FRICTION MATERIALS

GAVIN JOHN HOWELL

A THESIS PRESENTED TO FULFIL THE REQUIREMENTS

FOR THE DEGREE OF

MASTER OF SCIENCE IN ENGINEERING

DEPARTMENT OF MATERIALS ENGINEERING
UNIVERSITY OF CAPE TOWN
NOVEMBER 1994

ACKNOWLEDGEMENTS

The author would like to thank the following people/organisations for their contributions:

In particular, my supervisor, Professor Anthony Ball for the initiation of the project and his guidance.

Mr David Rose of Duralcan U.S.A. for the provision of materials, technology and advice.

Dr Timothy Hurd of Hulett Aluminium for the provision of materials and finance.

Dr Scott Wilson for his useful advice in specimen preparation.

Mr Chris Drake, Mr Gavin Keen, Mr Fareed Mohammed, Mr Robin Bath and Mr Tony Brewin of BMW, Ferodo, and Mintex Don for the provision of materials.

The Foundation for Research and Development for the provision of finance.

Mr Glen Newins for the machining of rig components and testing samples.

Mr David Dean for the setting up and maintaining of testing apparatus electrical equipment.

Mr Bernard Greeves for the extremely prompt developing of photographs.

Mrs Jacky Sharland and Mrs Anne Ball for their administrative assistance.

ABSTRACT

Two magnesium/silicon aluminium alloys each reinforced with 20 vol. % SiC particulates have been worn against three different automobile friction linings (brake pads). Two of the friction linings are commonly used against cast iron brake rotors while the third has been formulated for use against aluminium MMC brake rotors.

Wear processes at the interfaces of the specific rotor - pad combinations have been characterised through the analysis of friction traces and the use of optical and electron microscopy. Models on the interdependence of friction and wear, and models of wear mechanisms for aluminium MMCs and cast iron sliding against friction materials have been proposed and discussed.

For an aluminium MMC sliding against an organic pad formulated for use against cast iron, wear rates are low and friction is constant due to the formation of a solid lubricant layer at the wear interface. When this MMC is worn against a semi-metallic pad formulated for use against cast iron, wear rates are extremely high due to two and three body abrasion which lead to subsurface delamination and early melt wear in the MMC.

For an aluminium MMC developed for its use in automobile brake rotors sliding against a semi-metallic pad specifically formulated for its use against MMC brake rotors, wear rates at low loads are low although friction traces are irregular and fracture of the SiC particulates occurs at the lowest load and sliding velocity. This fracture of SiC is caused by the abrasive action of hard alumina particles within the pad. At high loads and sliding velocities cohesiveness of materials within the pad is poor and the wear rate of the MMC is extremely high. At the highest load/sliding velocity combination, the wear resistance of the MMC is inferior to that of its unreinforced matrix.

If the structure and composition of friction linings are arranged correctly, the wear resistance and frictional performance of aluminium MMC brake rotors are superior to those of cast iron brake rotors. In addition, the lower density of aluminium MMCs provides for an economic advantage over cast iron with respect to efficient use of fuel, and fabrication expenses.

GLOSSARY

μ	= Friction coefficient
K	= Thermal conductivity ($W.K^{-1}.m^{-1}$)
ρ	= Density (kg/m^3)
C_p	= Specific heat for mass ($J.kg^{-1}.K^{-1}$)
$C_p \times \rho$	= Specific heat for volume ($J/m^3.K^{-1}$)
PV factor	= Measure of the rate of energy input into the sliding interface ($J.s^{-1}$ or $Pa.m.s^{-1}$)
G_{1c}	= Mode 1 fracture toughness (J)
σ_f	= Fracture stress (Pa)
ε_f	= Fracture strain
f_p	= Particle area fraction
a_c	= Critical crack length (m)
E	= Young's modulus (Pa)
SEM	= Scanning/secondary electron microscope/y
EDX	= Energy dispersive X-ray spectroscopy
BEM	= Back scattered electron microscopy
A357	= Magnesium silicon aluminium alloy
A357 MMC	= A357 alloy reinforced with 20 % SiC particulates by volume.

A359	= Magnesium silicon aluminium alloy containing copper.
A359 MMC	= A359 alloy reinforced with 20% SiC particulates by volume.
Cast iron	= Pearlitic grey cast iron.
MMC	= Metal matrix composite.

TABLE OF CONTENTS

CHAPTER **PAGE**

CHAPTER 1

Introduction

The strengthening of aluminium alloys with a dispersion of fine ceramic particulates has dramatically increased their potential for wear resistant applications[1,2,3,4] . One of these applications is the development of MMC aluminium alloy brake discs[5], with advantages over cast iron with respect to their high thermal conductivity and low density. Consideration of frictional properties is of paramount importance in the design of automobile braking systems and S. K. Rhee[6] found the frictional force in braking systems to be a power function of the applied normal load and sliding speed, at a fixed local contact temperature. In empirical equation form:

$$F = \mu(T) \times P^{a(T)} \times V^{b(T)} \quad \text{.....1.1}$$

Where F = frictional force

P = applied load

V = sliding velocity

$\mu(T)$ = coefficient of friction at temperature T

a(T) = load factor at temperature T

b(T) = velocity factor at temperature T

In common braking systems a(T) ranges between 0.8 and 1.25, while b(T) ranges between -0.25 and +0.25.

Thus, from Rhee's analysis, the frictional force varies with temperature. A decrease in frictional force (braking capacity) with an increase in contact temperature is referred to as brake fade[7,8] and it is the goal of engineers to design friction couples for which μ, a & b are independent of rotor temperatures. The ideal values of a & b being 1 and 0 respectively[9]. Further disadvantages of braking systems which induce high temperatures include the following:

- greater probability of brake fluid boiling -

- increased pad wear -

- increased tendency for rotor scoring -

- higher stresses in the rotor due to thermal gradients which can cause -

- rotor cracking and warping -

R. Limpert[10] found that the maximum brake rotor temperature for a specified heat flux and braking time decreases as an inverse function of the square root of the thermal conductivity, specific heat and density. Thus a rotor of high thermal conductivity will have a significant advantage over a rotor of low thermal conductivity provided the product of the specific heat and density remain the same.

A rotor of high thermal conductivity efficiently conducts heat away from the hot points on the outer rim of the rotor to the hub of the rotor which acts as a heat sink. Temperature gradients in the rotor are thus minimised decreasing the probability of rotor cracking through thermally induced stresses.

Table 1 below shows thermal conductivity K ($W.K^{-1}.m^{-1}$ - @25°C), specific heat C_p ($J.K^{-1}.kg^{-1}$ - @25°C), density ρ (kg/m^3), the product of the specific heat and density $C_p \times \rho$ ($J.K^{-1}/m^3$) and thermal diffusivity $K.C_p^{-1}.\rho^{-1}$ (m^2/s) values for a pearlitic grey cast iron commonly used in automobile brake rotors and an aluminium MMC developed by Duralcan USA for its use as a brake rotor material.

Table 1.1

Material	K	C_p	ρ	$C_p \times \rho$	$K/(C_p \times \rho)$
Cast iron	42	511	6.9×10^3	$3{,}53 \times 10^6$	1.18×10^{-5}
MMC	182	840	2.8×10^3	$2{,}35 \times 10^6$	7.74×10^{-5}

During light braking the product of the specific heat and density (i.e. the volumetric specific heat) more significantly affects the peak rotor temperature than does the thermal conductivity, but during moderate to heavy braking, thermal conductivity plays a predominant role in determining peak rotor temperatures[11]. It follows from Table 1 above that during light breaking, cast iron rotors will run cooler than aluminium MMC rotors but as the applied pressure and sliding velocity increase, aluminium MMC rotors with their high thermal conductivity (property governing heat flow at steady state) and their high thermal diffusivity (property governing transient heat flow) will run cooler and should show superior frictional stability over cast iron rotors. The thermal conductivity and expansion of MMC rotors can be adjusted by adjusting the level and distribution of particulate reinforcement[12,13].

Efficient use of fuel has become a critical factor in the design of automobile components and light weight vehicles constructed from light weight/low density components promise to be more fuel efficient than their heavier ancestors. In addition, lower density materials need less bulky casting, extrusion and forging machinery which leads to decreased overheads during fabrication. Aluminium MMC brake discs are now in production with properties of both the disc material and friction lining material being refined to meet friction, wear and fabrication criteria[14,15]. Friction and wear performance are, however, the most important considerations in the design of MMC brake rotors and it is the investigation of the interdependence of these two properties that comprise the bulk of this thesis.

Standard procedures exist for the testing of automobile braking systems SAE (Society of Automotive Engineers) J661a[16]. Testing of materials in this thesis has not strictly followed these standard testing procedures and has been more scientific in nature. The objective of this thesis is to develop an understanding of wear modes occurring at the friction interface when aluminium MMCs their matrices and cast iron are worn against a variety of automobile friction materials. These wear mechanisms determine the frictional behaviour of the sliding couple. By observing friction traces generated for each sliding velocity and contact pressure combination and then correlating this information with wear surface microscopy, one gains insight into the prevalent wear mechanisms for the specific velocity/pressure combinations. Usually, during standard brake testing, wear rate and frictional performance trends are established without investigating the wear mechanisms responsible for these trends. This has been the norm for recent testing of modern friction materials specifically formulated for use against aluminium MMC rotors[17]. An improvement in the materials' braking efficiency can only be facilitated once a thorough understanding of these wear mechanisms has evolved.

Testing of materials in this thesis has been conducted in two phases. The first phase is an investigation of a common magnesium/silicon aluminium alloy reinforced with 20 vol. % SiC particulates worn against two classes of commonly used brake pad materials. In this phase the evolution of transfer layers at the wear surface and their effect on friction and wear is investigated. This phase can be considered an introduction to the second phase where an aluminium alloy MMC specifically designed for its use as a brake rotor material is worn against a brake pad material specifically designed for its use against aluminium MMC brake rotors. In this phase the identification, through optical

and electron microscopy, of deformation and fracture wear mechanisms on the MMC wear surface is emphasised. The influence of transfer layers on friction and wear is again investigated in this testing phase.

During both phases of testing a pearlitic grey cast iron and the unreinforced matrices of the composites were tested under identical conditions for comparative purposes. Results of the two phases of testing are discussed in terms of the effect of contact pressure, sliding velocity and the evolution of transfer layers on the friction and wear mechanisms occurring at the sliding interface.

CHAPTER 2

Literature review

2.1 *Introduction*

Although much research has been done concerning the friction and wear behaviour of various rotor materials sliding against many different categories of friction linings, this behaviour has been analysed in terms of friction traces and mass loss wear rates only. Literature dealing with wear mechanisms and friction, on a microscopic scale, in automobile braking systems is extremely limited. For this reason, a wider approach to the literature is maintained in this section. Firstly theories on friction are analysed in terms of establishing its dependence on wear and vica versa. Relevant sliding wear mechanisms are then discussed followed by literature dealing with wear in unreinforced aluminium as opposed to wear in aluminium metal matrix composites. Finally, literature investigating friction and wear of cast irons and fibre reinforced phenolic resins is presented.

2.2 *The interdependence of friction and wear*

Frictional behaviour is important in tribology because it generally affects the wear behaviour. E. Rabinowicz[18] and N. Suh[19] found that delamination wear is affected by surface traction because of its affect on crack nucleation and propagation processes at the subsurface. Ploughing by wear particles and asperity deformation both affect the wear processes and frictional behaviour. To investigate the interdependence of friction and wear comprehensively, however, one needs to trace the development of theories on friction and the components of the coefficient of friction.

Early researchers into the mechanics of friction have forwarded the concept of asperities on sliding surfaces interlocking to form junctions which must be sheared to satisfy kinematic requirements[20,21,22]. In this adhesion theory of friction, the frictional force depends directly on the actual area of contact which is a function of the applied normal and tangential loads. Since the adhesion theory of friction emphasises the importance between the adhesion of asperities, the surface energy and the mutual solubility of contacting materials

have been considered to influence adhesion and hence the coefficient of friction at elevated interface temperatures[23].

More recently, it has been postulated that mechanical properties of materials affect the frictional behaviour to a greater extent than chemical properties and, further, that adhesion is not the only factor to be considered in the generation of friction. In one of the most comprehensive studies on friction N. Suh and H Sin[24] postulated that the coefficient of friction between sliding surfaces is due to the combined effects of an asperity deformation component μ_d, a component μ_p from ploughing by wear particles and hard surface asperities and a component μ_a from adhesion between smooth surfaces. The relative contributions to the actual friction coefficient by these components depend on the condition of the sliding interface which is affected by the history of sliding, materials used and the environment. This sliding-time dependent nature of the coefficient of friction can be understood qualitatively from the schematic below in fig 2.1:

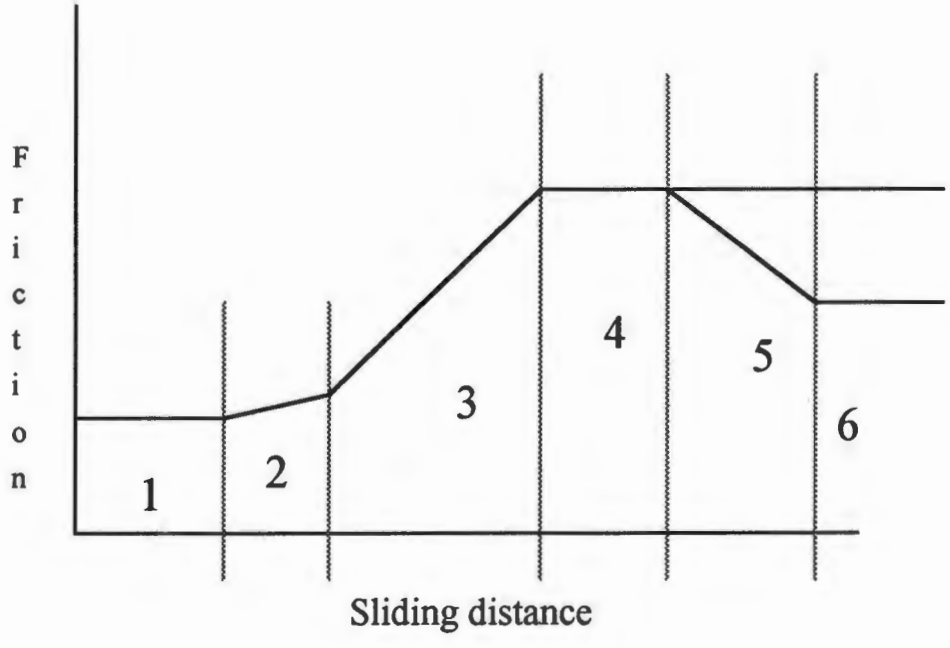

Fig 2.1: Six stages in the frictional force Vs distance relationship (after Suh et al[24])

In the above figure, stage 1 is dominated by the ploughing of the surface by asperities. the ploughing component μp of the friction coefficient will thus be

dominant during this stage. During stage 2 the frictional force begins to rise slowly because of an increase in adhesion. Stage 3 is characterised by a steep increase in slope due to a rapid increase in the number of wear particles entrapped between the sliding surfaces as a consequence of higher wear rates. Stage 4 is reached when the number of wear particles entrapped at the interface remains constant. When a hard material is worn against a soft specimen, the asperities of the hard surface are gradually removed (stage 5) creating a mirror finish. Here the frictional force decreases owing to a decrease in ploughing and asperity deformation. Eventually, in stage 6, the softer surface also acquires the same mirror finish and the frictional force levels off .

Sometimes when the hard surface is not stationary but is moving against the softer surface, the hard surface remains rough and stages 5 & 6 are absent. Suh and Sin found that values of μ_a (adhesion component of friction) can range from 0 to 0.4 and values of μ_p (ploughing component of friction) also from 0 to 0.4 under typical conditions. When the depth of penetration by wear particles is large, however, μ_p can be as large as 1. The asperity deformation component μ_d dictates the static coefficient of friction and can range from 0.43 to 0.75 depending on the slope of the asperities.

The role of asperities in the generation of friction has been investigated in other studies[25,26,27]. T. Ying and S. Hsu[28] simulated conditions of wear for a single asperity and found that one could define friction at an asperity level as the resistance to flow of the material. If the contact is lubricated and the load is low, the resistance is largely due to the interfacial shear strength of the interfacial layer or lubricating film. At high deformation loads, shear will occur within the bulk material. Ying and Hsu further found that the critical asperity friction coefficient for wear to occur is approximately 0.4 and that an increase in friction coefficient above this value will decrease the area of the plastic zone on the material surface. This decrease in thickness means that large plastic deformation is stored within a very small volume. Once the plastic strain is greater than the equivalent fracture strength of the material, wear will occur.

Wear mechanisms that have been found to contribute to an increase in friction are transfer, where transfer of material is involved in some transitions from smooth to rough sliding[29,30] and flaking where plastic flow occurs at discontinuities on the wear surface[31]. Parameters such as hardness ratios and the environment also effect friction and wear. some researchers have found oxidation greatly increases friction and wear[29,30], while others have

found the opposite[32,33]. The kind of materials used determines whether oxidation is benign or damaging to the wear surfaces. In some materials e.g. dual phase steels it is assumed that oxygen aids in the formation of wear debris by a process of oxygen embrittlement[34], thereby increasing friction and wear.

2.3 *Sliding wear mechanisms*

2.3.1 *Abrasive wear by plastic deformation*

Figure 2.2 shows an abrasive particle, idealised as a cone of semi-angle (α), being dragged across the surface of a ductile material which flows under an indentation pressure (P). It forms a groove in the material, and wear is assumed to occur by the removal of some portion of the material which is displaced by the particle from the groove. The normal load, (ω), carried by the particle is supported by plastic flow beneath the particle, which causes a pressure (P) to act over the area of contact between the particle and the surface. In equation form:

$$\omega = P \times \pi \times \frac{a^2}{2} = \frac{1}{2} \times P \times \pi \times x^2 \times \tan^2 \alpha \quad \text{.....2.1}$$

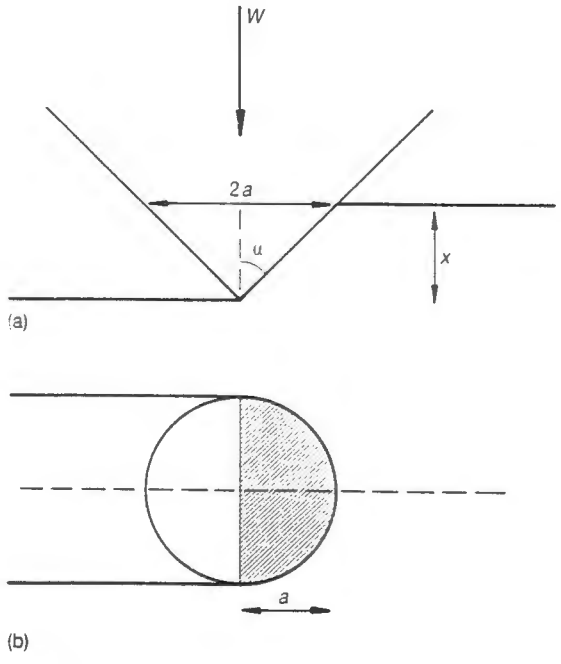

Fig 2.2: Geometry of contact between an idealised conical abrasive particle and a surface a). in elevation b). in plan view (after I. M. Hutchings[35])

The volume of material of material displaced from the groove by the cone in sliding a distance (l) along the surface is $l \times a \times x$, or $l \times x^2 \times \tan\alpha$. The quantities a and x are defined in fig 2.2. So if a fraction (η) of the material displaced from the groove is actually removed as wear debris, then the volume of wear debris produced by this one particle per unit sliding distance (q) will be given by:

$$q = \eta \times x^2 \times \tan\alpha \quad \text{.....2.2}$$

Substituting for x^2 in equation 2.1:

$$q = \frac{2 \times \eta \times \omega}{\pi \times P \times \tan\alpha} \quad \text{.....2.3}$$

Summing over many abrasive particles and assuming that P $\approx$ H, the indentation hardness of the material, it can then be shown that the total volume removed per unit sliding distance (Q) is given by:

$$Q = \frac{K \times W}{H} \quad \text{.....2.4}$$

Where (W) is the total applied normal load and the constant (K) depends on the fraction (η) of displaced material actually removed, and on the geometry of the abrasive particles (i.e. on α). The dimensionless wear coefficient (K) can be used as a measure of the severity of wear. Typical values of (K) in the two body abrasive wear of metals lie between ~5×10^{-3} and ~50×10^{-3}. As in the case of sliding wear, it is sometimes more useful to employ the dimensional wear coefficient (k) where $k = \frac{K}{H}$ with usual units $mm^3(Nm)^{-1}$.

Sometimes the severity of abrasive wear is expressed through the specific energy of material removal (U). In terms of the quantities discussed above:

$$U = \frac{\mu \times W}{Q} \quad \text{.....2.5}$$

where (μ) is the coefficient of friction between the sliding bodies. The value (U) can also be expressed in terms of (μ) and (k):

$$U = \frac{\mu}{k} \quad \text{.....2.6}$$

For two body abrasion of metals in air (μ) lies typically between 0.4 and 1, while for three body abrasion conditions it is often lower i.e. 0.2 to 0.5.

2.3.2 *Abrasive wear by brittle fracture*

Figure 2.3 shows how wear can occur in a brittle material for example cast iron that contains brittle graphite flakes. The frictional traction imposed on the surface as an abrasive particle slides across it causes cracks to open along the planes of the graphite lamellae lying normal (or nearly normal) to the sliding direction. Material is then detached by the propagation of shear cracks parallel to the surface, at a depth equal to the penetration of the abrasive particle.

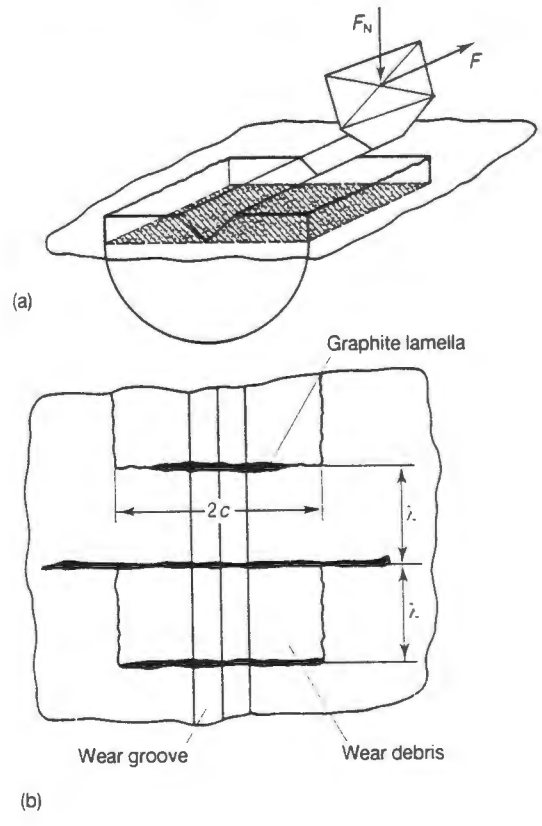

Fig 2.3: (a). Perspective and (b). plan views showing crack formation modified by the presence of weak graphite lamellae during the abrasive wear of grey cast iron[35].

The size of the debris fragment is defined by the depth of penetration of the abrasive particle, by the width of the cracks in the graphite flakes (2c in fig 2.3b) and by the mean separation of the graphite flakes λ. This model leads to a wear rate due to (N) particles given by:

$$Q = \beta \times N \times \frac{\omega^{3/2} \times H^{1/2}}{K_{1c}^2} \quad \text{.....2.7}$$

Where β is a factor which incorporates the coefficient of friction for the system, the geometry of the particles and the spatial distribution of the graphite lamellae. K_{1c} is the mode 1 fracture toughness of the grey iron.

The model for wear by brittle fracture of grey cast iron described above predicts considerably higher wear rates than for the model of abrasive wear by plastic deformation described in section 2.3.1.

2.3.3 *Oxidative wear*

Flash temperatures of several hundred degrees can be generated during sliding and the magnitude of these flash temperatures depends strongly on sliding velocity[36]. Only moderate sliding velocities are needed with most ferrous metals before these hot spot temperatures become high enough to cause significant surface oxidation. Growth of a substantial oxide film suppresses plasticity dominated wear mechanisms by reducing the shear strength of the interface and hence the development of large subsurface shear strains necessary for these mechanisms. In oxidative wear, debris is removed from the oxide layer.

At low temperatures, significant oxidation occurs only at asperity contacts and is associated with transient flash temperatures. The fact that some FeO is found in the wear debris of steels sliding at low bulk temperature, for example, suggests that it forms at the hot-spots rather than at the lower mean temperature of the surface. FeO grows under static conditions, only above 570°C. At higher temperatures, however, general oxidation of the surface outside the contact zone becomes more important and may even dominate. In the oxidative wear of ferrous metals, the predominant oxide present in the wear debris changes with sliding velocity. At low velocities and temperatures α-Fe_2O_3 dominates, at intermediate sliding velocities and temperatures Fe_3O_4

dominates and at high sliding velocities and temperatures FeO dominates. Oxide growth during sliding, like thermal oxidation under static conditions, obeys an Arrhenius equation:

$$k_p = A^{-\left(\frac{Q}{R \times T}\right)} \quad \text{.....2.8}$$

Where (k_p) is the parabolic rate constant for growth of the oxide film, (T) is the absolute temperature, (R) is the universal gas constant, (Q) is the activation energy for oxide formation and (A) is the Arrhenius constant.

There have been many proposals for detailed mechanisms by which oxide particles become detached as wear debris. Growth of oxide on an asperity tip immediately after it has been scraped clean by contact with the counterface may be followed by removal of that oxide in the next contact event. This process has been termed "oxidation-scrape-reoxidation" (o-s-r). The fine particles of oxide removed in this way might agglomerate into larger transfer particles before finally being released as debris.

Experimental evidence[34] suggests that under many circumstances an appreciable thickness of oxide (perhaps several micrometers) builds up on the metal surface before it becomes detached as debris particles. Mechanisms have been proposed in which "islands" of oxide grow until they reach a critical thickness at which stage they spall off. These islands may be homogeneous oxide layers growing by tribochemically enhanced oxidation of the wear surface. Alternatively, the oxide islands may be aggregates of fine particles generated at asperity contacts by o-s-r, or perhaps aggregates of fine metallic particles which have oxidised after detachments from asperity peaks.

The possibilities of transfer and back-transfer of oxide particles, and of abrasive wear caused by hard oxide particles, add further complexities to the range of oxidative wear mechanisms which have been put forward.

2.4 Alloying and its effect on the wear of aluminium

Silicon is one of the most common elements added to aluminium to increase its wear resistance, although consensus must still be reached as to whether

silicon does indeed serve this function. A. Sakar[37] and J. Clarke[38] concluded that the eutectic aluminium silicon alloy has the best wear resistance out of the Al-Si alloys. Silicon improves wear resistance by influencing the transition load from mild to severe wear. This transition is from equiaxed wear particle formation to delamination of plastically deformed material[39]. G. Meyer-Rodenbeck et al[40], however, postulated that course and brittle silicon rich phases in the soft aluminium matrix are responsible for the poor abrasion resistance of these alloys. The addition of magnesium up to 1 wt % has been found to reduce wear in aluminium silicon alloys. The magnesium combines with the silicon to form an $MgSi_2$ phase which improves material properties such as hardness[41,42].

Iron, if present alone, forms an intermetallic compound with aluminium at grain boundaries and impairs mechanical properties. When manganese, chromium, cobalt or molybdenum are present, iron combines with them to form less harmful compounds[41]. Copper is also added to aluminium to improve mechanical properties via solid solution strengthening and precipitation of their intermetallics. Silicon particle refining with strontium is also thought to improve wear resistance in aluminium silicon alloys.

2.5 *Wear in unreinforced aluminium alloys*

The effect of intermetallics on the wear of 99% purity aluminium slid against tungsten carbide has been investigated by C. Chiu et al[43] who found that exposed portions of these intermetallic particles serves two functions: 1 - severe local strain gradients around these particles may result in the nucleation of cracks that subsequently grow at an angle to the wear surface. The propagation of these cracks into the heavily deformed near wear surface layer can result in debris formation, 2 - the exposed portions of these particles create

a local milling action resulting in the formation of looses debris or back transfer from the tungsten carbide slider.

D. Rigney et al[44] investigated the wear behaviour of high purity aluminium sliding against tool steel where it was found that wear occurs mainly by extrusion at the exit side of the wear scar. Wear and seizure in binary aluminium silicon alloys has been investigated by A. Somi Reddy et al[45]. In their experiments, when these alloys were worn against hard steel they

assumed that silicon reduced the tendency to form adhesion welds at the wear surface. Adhesion welds contribute to seizure and the addition of 7 wt % silicon to pure aluminium allows the sliding process to continue without seizure up to 2.5 times higher loads than pure aluminium. Silicon also allows for higher wear surface temperatures without seizure. It was also found that in alloys containing up to 17 wt % silicon, a layer of compacted debris forms on the surface, protecting the alloy against wear. A transition from mild to severe wear occurs owing to the destabilisation of the protective layer by subsurface flow arising from silicon contents in excess of 17 wt %.

Work done by H. Torabian et al[46] reveals that when aluminium silicon alloys are worn against high carbon chromium steels, oxidative wear is experienced at low loads, combined oxidative and metallic wear at intermediate loads and metallic wear at high loads. The wear rate of aluminium silicon alloys is also sensitive to sliding velocity. Torabian et al found that the wear rate of aluminium silicon alloys initially decreases with increasing sliding velocity up to a certain value beyond which wear increases rapidly. Wear fragments in these alloys are produced by cracking and spalling of oxides, adhesion, abrasion and/or delamination of surface layers.

2.6 ***Wear in aluminium metal matrix composites***

2.6.1 *The effect of transfer layers*

The evolution of transfer layers is important in braking systems since these layers should have a marked effect on friction and wear. Scant mention is made of these transfer layers in the literature. This section will thus emphasise transfer layers observed in other wear systems.

Yang and Chung[47] investigated wear rates of an aluminium silicon eutectic alloy reinforced with bauxite particles sliding against a hardened steel

counterface. When 3 wt % graphite was added to an alloy containing 8 wt % bauxite particles it displayed a wear rate some seventeen times below the unreinforced matrix alloy. This extremely low wear rate was attributed to the formation of a graphite solid lubricant layer on the steel surface. Some studies on other metal to metal sliding couples have shown that their friction and wear behaviour can be significantly affected by the formation of wear transfer layers[48]. The composition of transfer layers is a good indication of the

cohesive strengths of the two wearing materials in the couple where the direction of transfer is usually from the cohesively weaker material to the cohesively stronger material[49,50]. The formation of transfer layers in some MMCs is considered to be one of the major reasons for composites displaying improved wear behaviour over that of their respective unreinforced matrix alloys[51,52].

When Alpas and Zhang[53] investigated an aluminium silicon alloy reinforced with silicon carbide sliding against a steel counterface they detected the presence of an iron rich transfer layer at low loads. X-ray analysis of the transfer layer revealed that it consisted primarily of iron oxide and silicon carbide debris. When the loads were increased above a critical point, wear rates of the composites increased to those of their respective matrix alloys and very little material transfer was found on the composite surfaces.

Sliding wear tests conducted by Pan et al[54] on an alumina and silicon carbide reinforced aluminium silicon alloy against steel also reported the formation of iron rich transfer layers on the worn composite surfaces. The worn surface of the alumina reinforced alloy showed a significantly higher iron concentration in comparison to that of the silicon carbide reinforced composite. This was attributed to the chemical reaction between the oxide surface of the alumina particulates to produce an alumina iron oxide interface. Anand and Kishore[55] have also reported the transfer of steel counter material to the worn surfaces of the reinforced aluminium composites.

Recent approaches in the processing technologies of metal matrix composites have provided new means of producing composites for tribological applications. One approach has been to incorporate shearable particles like graphite or mica into cast or sintered aluminium alloys[56,57,58,59]. Rohatgi and co-workers have shown that this type of composite derives its sliding wear resistance from the formation of graphite layers that act as solid lubricants at the contact surfaces[60,61]. The factors that influence the wear resistance of graphite/particulate reinforced aluminium alloys have been studied by Das et al[62] and Rohatgi et al[63] where the formation of graphite solid lubricant layers has been an important wear rate controlling factor.

2.6.2 *The effect of elevated temperature*

An increase in braking pressure and relative sliding velocity will always result in an increase in temperature at the sliding interface provided all other variables

remain constant. These temperatures can reach levels close to those of either, artificial ageing temperatures, or melting temperatures of aluminium MMCs. It is important, therefore, to be aware of high temperature effects , in particular, on the interface between the reinforcing particulates and the surrounding aluminium matrix.

A number of researchers[64,65,66] have found that Al_4C_3 formation is one of the main reactions in aluminium/silicon carbide systems which is known to significantly degrade the properties of the material. The formation of small $MgAl_2O_4$ particles have also been reported at the interfaces of as cast Mg-Si MMCs under high temperatures[67,68,69,70,71]. These interface embrittling effects occur at close to or above the melting point of aluminium. Only under extreme conditions do braking systems reach these temperatures. The consideration is still important, however, since contacting asperities on the wear surfaces can experience flash temperatures up to five times as high as the bulk material directly beneath it[72].

M. Martinez et al[73] investigated the wear of aluminium silicon alloys and aluminium silicon alloys reinforced with silicon carbide particulates at ambient and elevated temperatures. Aluminium silicon (7 wt %), aluminium silicon (12 wt %) were the matrices for the composites which were reinforced with 20 vol. % SiC particulates and were all worn against tempered steel counterfaces at temperatures ranging between 20°C and 200°C. It was found that at ambient temperature the reinforced alloys displayed lower wear rates and lower coefficients of friction than their unreinforced matrices. These ambient wear properties are maintained up to a temperature of 150°C where a sharp transition is found and the reinforced alloys do not show any better wear resistance than their unreinforced matrices. This phenomenon was attributed to large plastic strains arising in the matrix at elevated temperatures, bringing the matrix into direct contact with the steel. The strain gradients generated

beneath the contact surface led to subsurface crack propagation and wear proceeded through subsurface delamination. The transition to severe wear for the unreinforced alloys occurred at a temperature of 110°C. Other researchers have also noted improved thermal stability imparted to aluminium matrices through the addition of silicon carbide particulates[74]. Matrix microhardness far away from the contact surface was lower for composites tested at 200°C than at ambient temperature, suggesting overageing of the matrix in the composites at elevated temperatures. Studies have shown[75] that the presence of silicon carbide accelerates ageing in aluminium silicon alloys and it

is thought that reinforced aluminium alloys undergo more severe ageing than their unreinforced counterparts during sliding wear testing at elevated temperatures.

In a recent study by Z. Ma et al[76] the high temperature properties of in situ AL_4C_3 dispersoid and SiC particle mixture reinforced aluminium were investigated. This composite was prepared by ball milling commercially pure aluminium powder with 3 wt % graphite powder and 10 vol. % SiC particles in a high energy attritor for 1.5 hours and then heat treating at 600°C for 1 hour. This composite exhibits high strength and stiffness and an especially excellent elevated temperature strength at above 300°C. A few silicon carbide particles were even found to be fractured after tensile tests due to the increase in matrix strength resulting from Al_4C_3 dispersion strengthening. This technique may need to be investigated further for its potential with respect to increasing the high temperature strength of automobile brake rotors.

In their work in analysing thermal residual stresses in particle reinforced viscoplastic metal matrix composites, M. Suery et al[77] found that reheating aluminium after heat treatment and quenching can result in decohesion at the particle/matrix interface. The particular method of processing aluminium MMCs should also be chosen carefully since these processes can directly affect their high temperature performance during their subsequent application[78,79,80].

2.6.3 *Surface fracture and subsurface deformation*

In the analysis of surface fracture and subsurface deformation in MMCs it is useful to consider models developed to understand wear in general and surface fracture of MMCs in particular.

In Ball's analysis[81],wear occurs by a two stage process. Plastic strain is first accumulated and microfracture then occurs. For a virgin surface, the initial strain accumulation occurs during an incubation period, while strain accumulation and microfracture occur simultaneously and continuously during steady state abrasion, erosion or sliding wear.

If the effect of localised heating is ignored, the situation on the surface of the material being subjected to any type of wear is depicted below in fig 2.4.

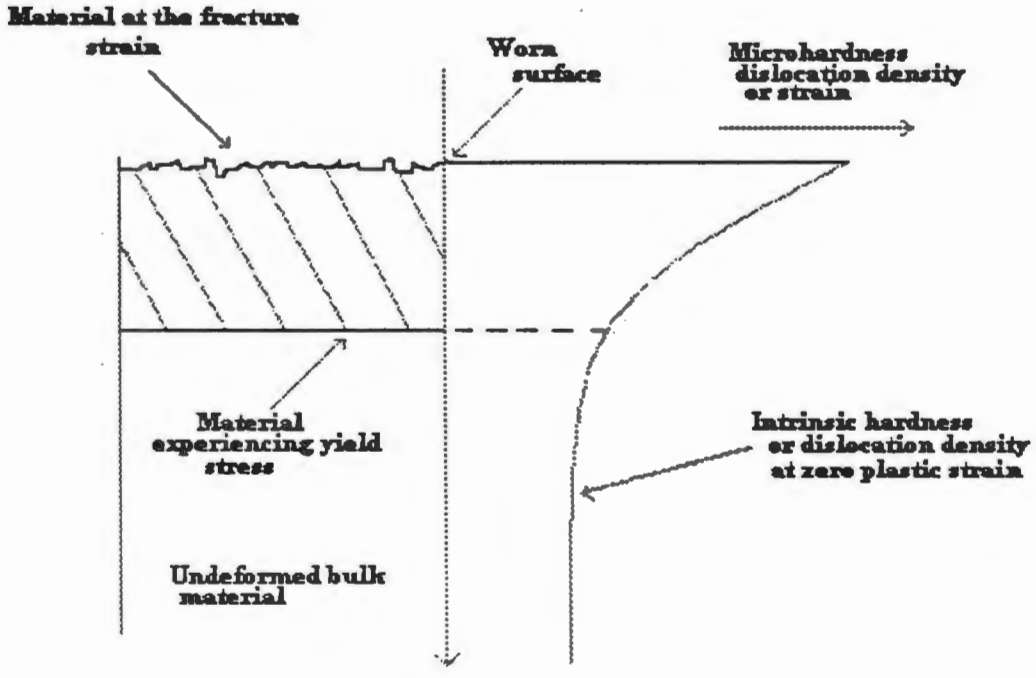

Fig 2.4: A schematic illustration of the deformed layer beneath the worn surface. The strain increases from the bulk value to a critical value at the surface. Microhardness and dislocation density increase correspondingly. (after Ball[81])

Irrespective of wear conditions, the material at the wear surface in the figure above, has reached a critical strain with a corresponding σ_f as the microfracture stress. A wear surface is therefore, by definition, a surface layer that has reached its critical strain. At some depth (t), the damage due to wear will be zero and the strain will be that of the initial bulk material. Assuming no influence of localised heating, the hardness and dislocation density will increase continuously as the surface is approached from the bulk material.

S. Wilson et al[1] studied the wear resistance of a range of aluminium MMCs under abrasive and sliding wear conditions. He found that the higher yield stresses arising in the matrix alloy as a consequence of increased matrix protection and constraint effects by the reinforcing particulates, introduce a "pseudo - brittle" effect in the matrix. Thus, the failure of the constrained matrix alloy in the composite, occurs at lower levels of plastic strain and work hardening than those found in the matrix alloy. This observation is illustrated schematically in fig 2.5.

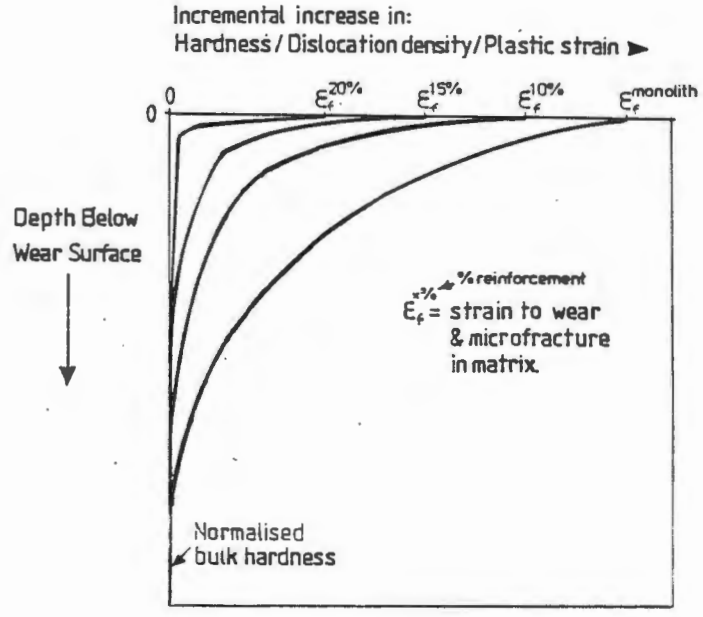

Fig 2.5: Schematic illustrating the effect of particulate additions on plastic strain accommodation in an aluminium alloy, below the sliding wear surface. (after S. Wilson et al[1])

Alpas et al[82] investigated the effect on wear of reinforcing an A356 aluminium silicon alloy with silicon carbide particulates. The composite was then worn against steel at low, intermediate and high loads. The wear processes at low loads in these composites are modelled below in fig 2.6.

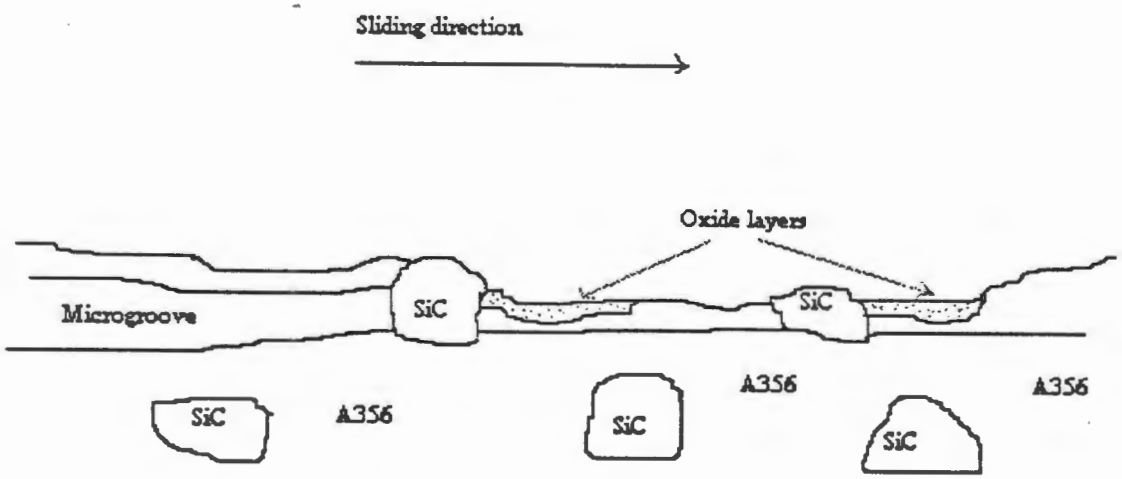

Fig 2.6: A schematic of the sliding wear mechanism in particulate aluminium composites at low loads - note how the silicon carbide particle on the left bears most of the load. (after Alpas et al[82])

A prerequisite for this type of wear is that the silicon carbide particles remain intact during wear to support the applied load and act as effective abrasive elements. When the applied load induces stresses that exceed the fracture strength of the silicon carbide particles, these particles fracture and lose their effectiveness as load bearing components. Shear strains are then transmitted to the matrix alloy and wear proceeds by a subsurface delamination process.

A criterion for the transition load between these two mechanisms could be established in terms of the fracture strength σ_f of the silicon carbide particles. Considering the applied load 'F' is solely supported by the silicon carbide particles on the surface of the composite, the normal stress on the particle (σ) is given by:

$$\sigma = \frac{F}{A \times f_p} \quad \text{.....2.9}$$

Where A = nominal contact area and
f_p = particle area fraction

As a first approximation, it may be assumed that all the SiC particles contain defects so the fracture strength of the particles is given as:

$$\sigma_f = \left(\frac{G_{1c} \times E}{\pi \times a_c}\right)^{1/2} \quad \text{.....2.10}$$

Where G_{1c} = mode 1 toughness and
a_c = fracture crack length

The critical defect size can be taken as proportional to the particle size 2r. Consequently:

$$\frac{F}{A} = n(G_{1c} \times E)^{1/2} \times \frac{f_p}{\sqrt{2r}} \quad \text{.....2.11}$$

Where n = number of particles

Accordingly, the highest applied load which can be supported by the silicon carbide particles should increase with silicon carbide volume fraction. When the applied load exceeds the critical load, wear occurs through a process of delamination by subsurface crack growth as displayed in fig 2.7:

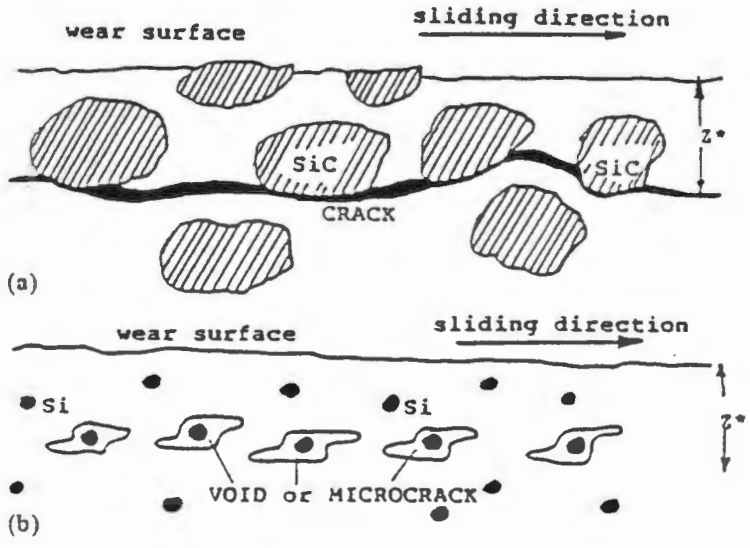

Fig 2.7 Schematic representation showing mechanisms of subsurface crack initiation and growth, (a) for microstructures involving coarse SiC particles, (b) for microstructures containing spherical silicon particles. (after Alpas et al[82])

The large plastic strains in the deformed layer gives rise to void nucleation around the silicon particles within the matrix alloy and subsurface crack propagation at the silicon carbide particle interfaces (decohesion).

Returning to Alpas and Zhang's hypothesis that the highest applied load which can be supported by the silicon carbide particles should increase with the silicon carbide volume fraction: M. Kulkarni et al[83] have observed that the fracture toughness of a 7075 aluminium alloy increased up to a volume fraction of 13% silicon carbide particles where the initiation of voids in the matrix was followed by crack arrest at the silicon carbide particles. Above 13 vol. % silicon carbide the fracture toughness decreased and failure was due to void nucleation at the particle/matrix interface leading to particle fracture and interface debonding. Alpas and Zhang's hypothesis may therefore only be true up to a certain limit of particle reinforcement concentration.

Fatigue failure in aluminium MMCs may be important with respect to their application in automobile braking systems and the fatigue behaviour of a 7091

aluminium alloy reinforced with 20 vol. % silicon carbide particulates has been studied by R. Ritchie et al[84], where evidence for crack bridging was found. The uncracked ligaments were found to be predominantly co-planar with the crack and directly associated with the fracture of silicon carbide particles ahead of the crack tip. Further studies of fatigue fracture in silicon carbide reinforced aluminium alloys have been conducted by H. Kim et al[85].

In their studies on silicon carbide reinforced 7091 aluminium alloy sliding against stainless steel, Wang et al[86] proposed that the non oxide nature of the wear debris was an indication that fatigue related surface cracking was the predominant wear mechanism. The influence of matrix strength and plasticity on the fracture of silicon carbide reinforced A356 aluminium alloys has recently been investigated by S. Corbin et al[87,88] where it was found that damage accumulation in the composite is largely dependent on heat treatment procedures prior to its application. Composites in the overaged (OA300) condition displayed a lower level of damage accumulation than those in the peak aged (T6) condition.

Rosenfield's[89] theories on subsurface dislocation networks can be used to understand the evolution of microhardness towards the wear surface in MMCs. Subsurface dislocation networks in MMCs have recently been studied by S. Wilson et al[1] where cell-like subsurface networks and persistent slip band ladder substructures were observed.

2.7 *Wear of cast iron against metals and phenolic resin friction materials*

As was mentioned at the beginning of this chapter, literature concerning the investigation of wear mechanisms occurring at the wear surfaces of metals and cermets slid against automobile friction linings is extremely limited. In this section the effects of sliding velocity and braking pressure on the dependent variables wear rate and coefficient of friction, will be emphasised, investigations of which are plentiful in the literature.

At low braking temperatures (i.e. low velocities) the wear rate in braking systems is controlled primarily by adhesive and abrasive mechanisms. At higher braking temperatures (i.e. higher velocities) other mechanisms such as melt wear and oxidation come into play[90]. In their comparative study by vehicle testing of copper and grey iron brake rotors S. Rhee et al[7] found that an increase in braking velocity led to a decrease in friction coefficient and

braking torque. This was attributed to the evolution of gases at the braking interface. The wear surfaces, however, were not microscopically examined. Y. Zhang et al[91] investigated the wear behaviour of phosphorous cast irons with differing graphite morphologies sliding against a chromium alloyed steel. The friction coefficient was found to be strongly dependent on load and sliding velocity i.e. with an increase in load or sliding velocity the friction coefficient was found to decrease greatly initially and then level out to a constant value.

With an increase in load, wear rates would increase greatly regardless of graphite morphology. With an increase in velocity wear rates would increase at first then decrease rapidly. No microstructural examination of the wear surfaces was conducted. Figure 2.8 below shows the dependence of wear rates and friction on load and sliding velocity:

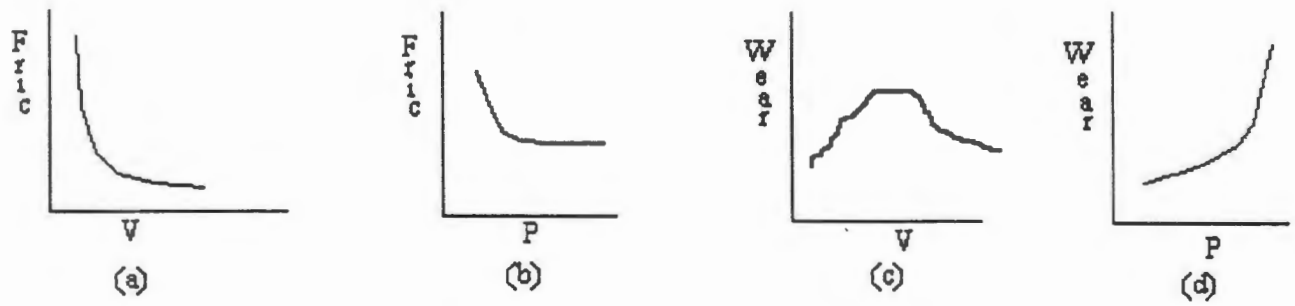

Fig 2.8: Graphs showing the relationships between (a) friction and velocity, (b) friction and load, (c) wear rate and velocity and (d) wear rate and pressure for cast iron sliding against stainless steel (after Y. Zhang et al[91]).

A. Verma et al[92] studied the effect on reinforcement on friction and wear of fabric reinforced phenolic resin composites sliding against cast iron. reinforcements used were kevlar 49, E glass and high strength carbon fibres. friction and wear were found to be strongly dependent on the fabric reinforcement within the phenolic resin. The lowest wear rates yet highest friction coefficients were recorded for the kevlar 49 reinforced composite. The high wear rates in the E glass reinforced composite was attributed to the abrasive nature of the wear debris. Wear debris from the kevlar 49 reinforced composite was found to be far less abrasive.

CHAPTER 3

Materials and experimental methods

3.1 *Materials*

The materials tested can be divided into two categories:

1. Automobile brake rotor materials

2. Automobile disc brake friction linings (brake pads)

3.1.1 *Rotor materials*

Five materials are compared for their use as rotor materials. The order in which they are presented will be maintained throughout this thesis. Exceptions to this ordering system will occur only in the microstructural characterisations in chapter 4, section 4.2 and in the conclusions in chapter 6. Aluminium MMCs are presented first since they are being investigated for their application in automobile braking systems. Cast iron is presented second since this is the material that aluminium MMCs must compete with and unreinforced aluminium alloys are presented last as control materials illustrating the benefits/disadvantages of reinforcing aluminium with SiC particulates.

a) An A357 cast magnesium/silicon aluminium alloy reinforced with 20 wt% SiC particulates. This material was supplied by Hulett Aluminium (South Africa) in ready cast solid cylinders and was heat treated to the T6 condition prior to testing.

b) An A359 cast magnesium/silicon aluminium alloy reinforced with 20 vol% SiC particulates supplied by Duralcan USA. This is a precision cast composite specifically designed for its application in brake rotor materials. This material was heat treated by Duralcan USA according to the Duralcan T71 heat treating procedure which involves solutionising the alloy at 538°C for 15 hours, quenching in hot water and artificial ageing at 246°C for 3 hours. This heat treatment places the composite in an overaged temper.

c) A pearlitic grey cast iron used in the rotors of modern light sedan disc brakes. This material was supplied by BMW (South Africa) and was machined into test samples from a brake rotor. This cast iron has a type B size four

(ASTM designation A257) rosette graphite flake distribution.

d) Unreinforced A357, being the matrix of the reinforced composite in (a) above - supplied in ready cast solid cylinders by Hulett Aluminium (South Africa) and tested after heat treatment to the T6 condition.

e) An unreinforced magnesium/silicon A359 cast aluminium alloy supplied by Hulett Aluminium (South Africa). This material is the matrix of the composite in (b)above and was heat treated according to the Duralcan T71 process prior to testing.

Table 2 below shows the actual wt % chemical composition (vol % for SiC) and Vickers bulk hardness of the five rotor materials - note that the lighter elements are not represented:

Table 3.1 - Rotor materials

Material	Si	Fe	Cu	Mg	Ti	Al	SiC	HV_{20kgf}
A357-MMC	6.0	0.45	-	0.23	-	73.32	20	118
A359-MMC	8.67	0.16	0.16	0.51	0.18	70.32	20	125
Cast iron	3.2	93.2	-	-	-	1.2	0	200
A357	6.2	0.42	-	0.24	-	93.14	0	61
A359	9.35	0.08	0.12	0.42	0.04	89.99	0	65

3.1.2 *Friction lining materials*

Automotive friction linings usually consist of several ingredients bound into a composite. These ingredients can be classified as fibrous reinforcement, binder, filler and friction modifier. Accordingly modern friction materials may be classified into three categories viz.: metallic linings (consisting of metal only), semi-metallic linings containing metal chips and organic fibres bound together with resins, and finally, organic linings containing organic constituents only. Of the above three lining categories only the latter two were considered for testing. Three makes of friction lining materials were tested against the rotor materials in the following order and this order will be maintained throughout the thesis:

a) Organic pad

This friction lining is currently used in the disc brake systems of heavier vehicles and has been developed for use against cast iron rotors. It is composed of organic fibres, rubber, graphite and internal lubricant, bound together with phenolic resins. It must be noted that this friction lining contains a small percentage of copper (0.6 wt%) which is added to improve the lining's thermal conductivity. Although, by definition, this friction lining is semi-metallic, it will be referred to as organic to provide clear distinction between it, and friction linings with high metallic constituents.

b) Semi-metallic pad A

This friction lining material is used in the front disc brake system of medium sized sedans and has also been developed for use against pearlitic grey cast iron rotors. It is a complex composite containing copper, aluminium and iron metallic chips or fibres in addition to rubber and graphite fillers all held together with phenolic resin binder.

c) Semi-metallic pad B

This friction lining has been specifically developed for its use against aluminium MMC rotors. It has copper aluminium and iron as its metal constituent embedded in a matrix of compressed paper. This pad also has an internal lubricant and contains no graphite nor rubber fillers, but does contain a small percentage of alumina.

Table 3 below details approximate composition (wt %), density ($g/cm^{3)}$ and hardness values for the three friction lining materials:

Table 3.2 - lining materials

Lining	Cu	Fe	Al	organic binder	graphite	rubber	paper	alumina	organic fibre	other	ρ
Organic	0.6	-	-	43	15	2	15	-	20	4.4	2.49
Semi-met A	15	43	3	25	7	5	-	-	-	2	3.12
Semi-met B	15	3	2	16	4	-	52	5	-	3	2.36

3.2 *Experimental procedure*

3.2.1 *Chemical composition*

Actual chemical composition of the five rotor materials was obtained through the use of energy dispersive X-ray analysis operating in conjunction with a scanning electron microscope. Chemical composition of lining materials was determined partly through the energy dispersive X-ray facility and partly through manual separation and weighing of constituents. A margin of error of 10% is to be expected with the percentages of organic constituents in linings.

3.2.2 *Testing apparatus*

An ARBOGA 2512 vertical drilling machine was modified to allow for a testing system where the rotor materials are attached to and revolve with the drill spindle to wear against the friction linings which are the stationary counterface. A schematic of the testing apparatus is shown below in fig 3.1. A torque cell underneath the stationary friction lining material continuously monitors the frictional force at the wear interface fig 3.2. A detailed view of the testing apparatus is shown in fig 3.3.

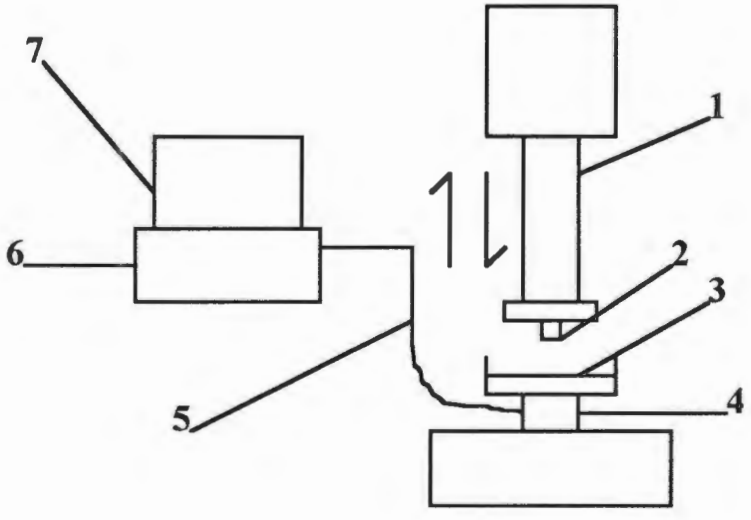

Fig 3.1: Testing apparatus, 1 - revolving drill spindle, 2 - attached cylinder (rotor material), 3 - fixed counterface (friction lining material), 4 - torque cell, 5 - electrical cable transferring channel signals to computer, 6 - Sperry XT computer, 7 - STATUS 30 display and processing.

Fig 3.2 - Revolving cylinder and stationary counterface

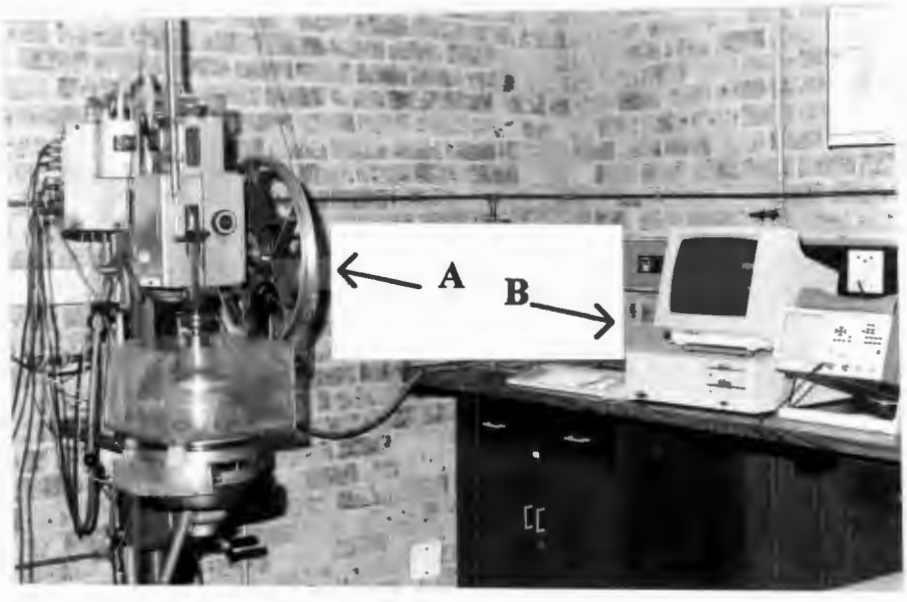

Fig 3.3: Photograph of the testing apparatus. A). signal generation section. B). data capture and display section.

The analogue electrical signal from the torque cell is converted to a digital signal through a PC30 analogue to digital signal processor interfacing with a Sperry XT computer. Load is applied through a leverage system using a load

cell positioned under the friction lining material to monitor and calibrate the correct loadings. The STATUS 30 version 2.01 A-D signal processor program was used to display and process information from the torque, load and spindle rotational velocity cells. Altogether, seven analogue signals are generated from the drilling machine and these may be tabulated in their respective channels:

Channel 0 - ground
Channel 1 - drill electrical power consumption
Channel 2 - load cell
Channel 3 - torque cell
Channel 4 - linear variable directional transducer
Channel 5 - spindle rotational velocity transducer
Channel 6 - alternative torque cell

Calibration equations for the torque and load cells are as follows:

$$\text{Torque (Nm), channel 3} = 1.33 \times \text{analogue voltage(channel 3)} + 13.33 \quad \ldots\ldots 3.1$$

$$\text{Load (N), channel 2} = 165 \times \text{analogue voltage(channel 2)} + 1057.6 \quad \ldots\ldots 3.2$$

$$\text{Then coefficient of friction } \mu = \frac{Torque(i.e.eqn{:}3.1)}{\frac{Ro - Ri}{2} \times Load(i.e.eqn{:}3.2)} \quad \ldots\ldots 3.3$$

Where Ro = outer radius of cylinder
and Ri = inner radius of cylinder

Care must be taken when using STATUS 30 Ver 2.01 to calibrate the computer system clock to correspond with normal time reference. In the case of the Sperry XT computer used, the system clock must be set to 4.65 MHz. This frequency may differ depending on the make of computer. When determining duration of testing, factors to be considered are the following:

1]. Number of samples per channel

2]. Number of channels to be sampled

3]. Frequency of sampling

4]. System clock frequency

When the system clock is calibrated correctly, the duration of the sampling period is equal to the number of samples to be taken multiplied by the number of channels to be sampled divided by the frequency of sampling.

The calibration equation for the chart recorder used to monitor thermocouple voltage difference (temperature) at the sliding interface is as follows:

$$\text{Temperature } (^{\circ}C) = 22 + (2 \times 10^{4} \times V) \quad \text{.....3.4}$$

Graph 3.1 below shows the relationship between the chart recorder voltage reading and bulk surface temperature.

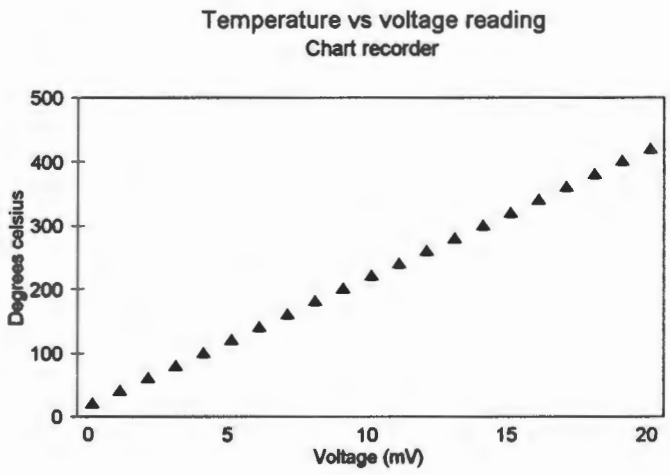

Fig 3.4: Graph showing the relationship between the chart recorder voltage reading and bulk surface temperature.

3.2.3 *Format and sequence of testing*

Testing was conducted in two phases. In the first phase, the 20%SiC reinforced A357 aluminium composite, its matrix alloy, and the pearlitic grey cast iron were worn against both the Semi-metallic pad A and the organic pad. A loading of 1.034 MPa and three sliding velocities ranging between 0.52m/s and 3.16m/s were employed during phase one of testing. The load employed is that recommended in SAE J661a. Table 4 below outlines the salient features of testing in phase 1:

Table 3.3 - Phase 1 testing matrix

Rotor materials	worn against	Lining materials	at	Sliding velocities	at	Load	with	Objectives
\V/		\V/		\V/		\V/		\V/
A357 MMC		Organic		0.52m/s		1.034 MPa		Investigate effect of transfer layers on friction and wear
Cast iron		Semi-met A		0.85m/s				
A357				3.16m/s				

Phase 2 of testing can be considered a special case of the introductory testing of general materials in phase 1. During phase 2 an aluminium MMC specifically designed for its use in braking systems, its matrix and the pearlitic grey cast iron are worn against a lining specifically formulated for its use against aluminium MMC rotors. Materials in this phase are worn against each other under two loads and four speeds. Table 5 below illustrates the testing features of phase 2.

Table 3.4 - Phase 2 testing matrix

Rotor materials	worn against	Lining materials	at	Sliding velocities	at	Load	with	Objectives
\V/ A359 MMC Cast iron A359		\V/ Semi- met B		\V/ 0.52m/s 0.85m/s 1.44m/s 3.16m/s		\V/ 0.517 MPa 1.034 MPa		\V/ investigate effect of transfer layers on friction and wear. Observe fracture and deformation features on wear surfaces

During both phases of testing, rotor and lining materials were worn against each other over varying distances depending on levels of safety and up to a maximum of 500m. Before and after each test the rotor and lining samples were weighed to gauge the wear per unit pressure per unit distance.

The use of the linear variable direction transducer for the continuous monitoring of wear rate was considered, but there are difficulties involved with this method. Firstly it is impossible to discern what fractions of wear recorded are attributable to either the rotor material or to the lining material. Secondly the evolution of transfer layers at the wear surfaces prevents accurate sampling.

Prior to each test, rotor material cylinders were ground down to standard surface finish on 600 grit emery pads and then run in at 1.44m/s and 230 kPa over a 50m sliding distance. Identical surface finishing and running in procedure was followed for the friction lining materials.

The testing sequence for each friction test was as follows:

1. Grind materials down to required surface finish

2. Weigh rotor and friction lining samples to an accuracy of 0.01 grams

3. Align and affix rotor materials and friction lining materials in testing apparatus.

4. Run materials in over 50m at prescribed load and sliding velocity.

5. Set up chart recorder monitoring post test wear interface temperatures.

6. Set number of samples and sampling frequency in status 30 display program. The number of samples and sampling rate ranged between 512 samples and 1024 samples, and 0.5 Hertz and 2 Hertz respectively.

7. Adjust sliding velocity and load to correspond with requirements for specific test.

8. Run friction test

9. Trap thermocouple at sliding interface immediately after cessation of relative sliding.

10. Monitor thermocouple voltage difference.

11. Remove wear debris from specimen surfaces with compressed air unless this debris is required for observation in the SEM.

12. Weigh worn rotor and friction lining materials to an accuracy of 0.01grams.

13. Process mass loss wear data on computer.

14. Import friction trace voltage data from status 30 display program into spreadsheet analysis program.

15. Convert friction trace voltage data in spreadsheet program to friction coefficient data.

16. File wear and friction trace data.

17. Print hard copies of processed friction and wear data.

18. Inspect wear surfaces and wear debris under optical microscope or in the SEM.

3.2.4 *Optical microscopy*

All MMC specimens and their matrices were wet ground and diamond polished to a finish of 1μm to reveal their microstructures. No etching was conducted on the MMCs and their matrices as etching confuses detail on dendrites. Cast iron microstructures were revealed by etching in a 2.5% nital solution for approximately 5 seconds. Cast iron specimens had been wet ground and diamond polished to 0.25μm finish before etching.

Optical microscopy was also conducted on ultrasonically cleaned post friction tested rotor materials. Under identical magnifications wear scar topography on the wear surfaces of the rotor materials could be compared. In some instances, Nomarsky microscopy was used to obtain a slight improvement in contrast between the silicon phase and the silicon carbide reinforcing particulates in the MMCs.

Matrix microhardness tests were conducted on samples of worn MMCs and cast iron cut perpendicular to the wear surface. These specimens were cut with a diamond blade microslicer at a slow feed rate and then polished to a surface finish of 1μm starting from an 800 grit emery pad.

3.2.5 *Scanning electron microscopy*

Wear scar topography, surface fracturing and transfer layers were investigated with an S200 scanning electron microscope. Post friction tested samples were coated with gold/palladium to render the surface material electrically conductive. This was particularly important in the case of the brake lining materials. Vacuum - up time during coating and electron microscopy may be greatly decreased by placing the lining materials in a furnace at 80°C for and hour before preparation for coating. Back scattered electrons generated by the electron microscope were employed to differentiate between materials of different atomic mass on the wear surfaces and within the samples.

Constituents of transfer layers and composition of materials embedded in the rotor wear surfaces were identified through an energy dispersive X-ray facility attached to the electron microscope. Wear debris generated during wear testing was affixed with resin to a steel surface then coated with gold/palladium before analysis in the electron microscope.

Chapter 4

Results

4.1 *Introduction*

The results of microstructural examinations of rotor and friction linings are followed by the results of testing phase-1 which are presented in a set order with organic pad friction traces first followed by the friction traces of semi-metallic pad A. The results of testing phase-2 are also presented in a set order with friction traces for low applied loads first followed by friction traces for high applied loads. Finally the results of an investigation into the reproducibility of friction traces is presented.

4.2 *Microstructures*

4.2.1 *Rotor materials*

During solidification of the unreinforced A357 aluminium, the silicon rich (darker) phase nucleates at the primary aluminium grain boundaries and grows dendritically inwards towards the centre of these grains - fig 4.1a. The dendritic silicon phase has a plate-like morphology with an average surface area 25μm^2 per plate - fig 4.1b.

a

Fig 4.1a: Dendritic structure of silicon phase within aluminium. Micrograph is unetched as etching confuses detail on dendrites.

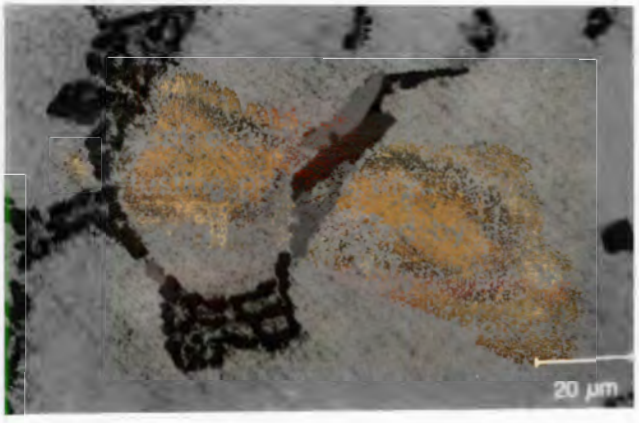

b

Fig 4.1b: Microstructure of unreinforced A357 aluminium showing plate-like morphology of the silicon dendrites.

In the A357 MMC, the dendritic network morphology is retained in the composite with the SiC particulates concentrating around the silicon dendrites - fig 4.2.

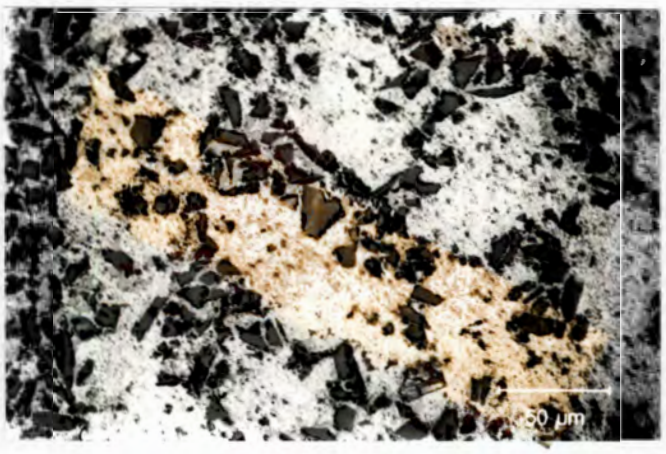

Fig 4.2: Morphology of the A357 MMC. Note the clustering of SiC particulates at the primary aluminium grain boundaries. The SiC particulates have an aspect ratio in the range 2:1 to 5:1 and an average size of 16µm.

The unreinforced A359 aluminium alloy contains more silicon and copper than the A357 alloy. The silicon phase has a needle-like (script) morphology in the unreinforced A359 - fig 4.3.

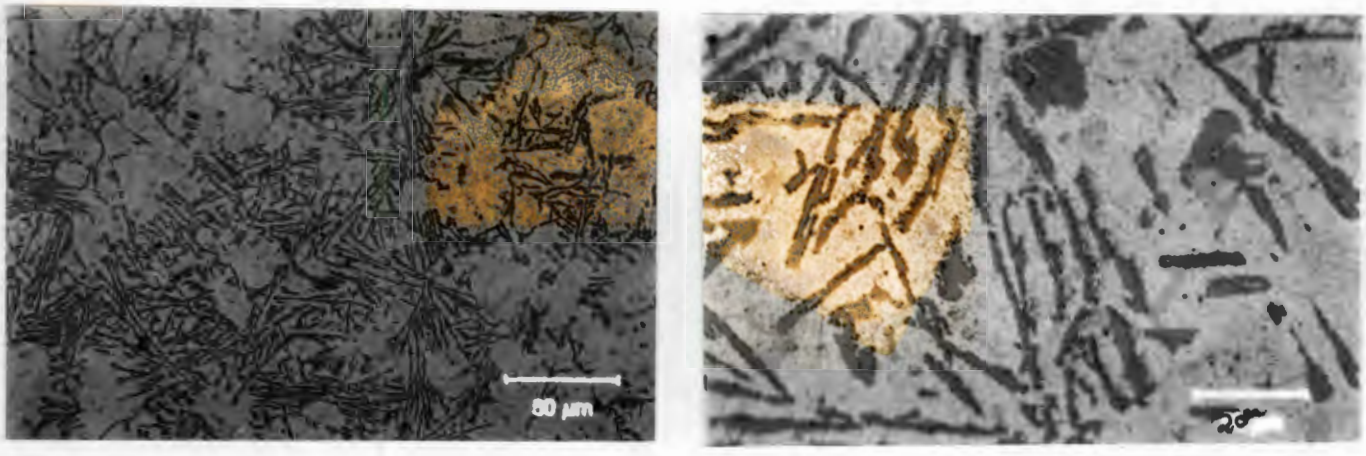

a b

Fig 4.3: Microstructure of the unreinforced A359 aluminium alloy a). needle-like (script) morphology of the silicon phase b). magnification of the silicon needles.

The microstructure of the A359 MMC is shown in fig 4.4.

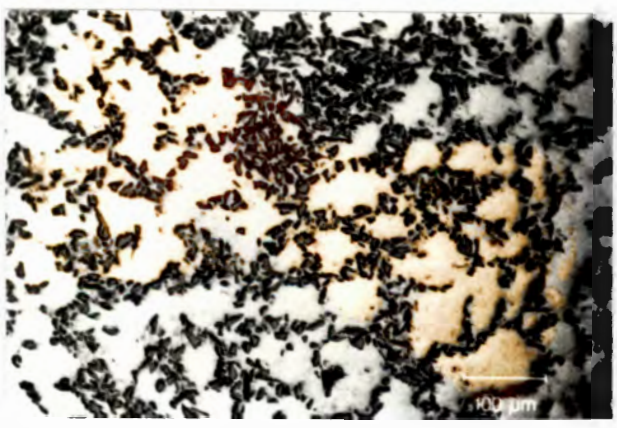

Fig 4.4: Microstructure of the A359 MMC. The aspect ratio and size of the SiC particulates is similar to that in the A357 MMC. The A359 MMC has a significantly lower porosity content than the A357 MMC.

The pearlitic grey cast iron tested in both testing phases has a random graphite flake distribution with the graphite flakes embedded in a matrix of pearlite and steadite. Figure 4.5 reveals the microstructure of this cast iron where the light areas in fig 4.5b constitute the steadite phase and the dark areas the fine pearlitic phase. Graphite flakes are an average of 120μm in length and 8μm in width.

a

Fig 4.5a: Microstructure pearlitic grey cast iron - unetched.

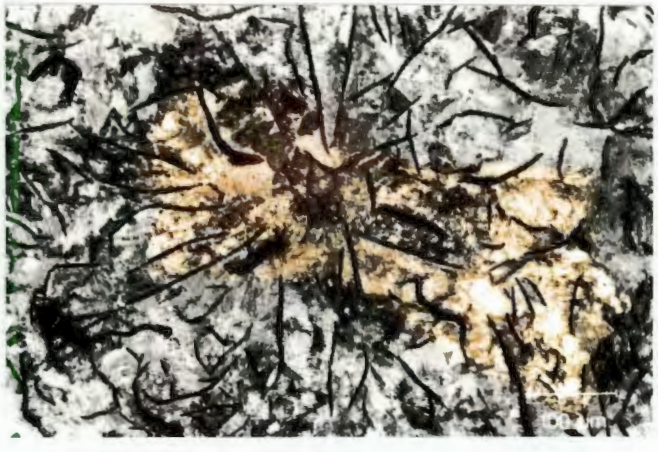

b

Fig 4.5b: Microstructure of pearlitic grey cast iron - steadite and pearlite between graphite flakes - etched with 5% nital solution.

4.2.2 *Friction lining materials*

Optical micrographs of the organic, semi-metallic pad A and semi-metallic pad B are shown in fig 4.6a, b and c respectively.

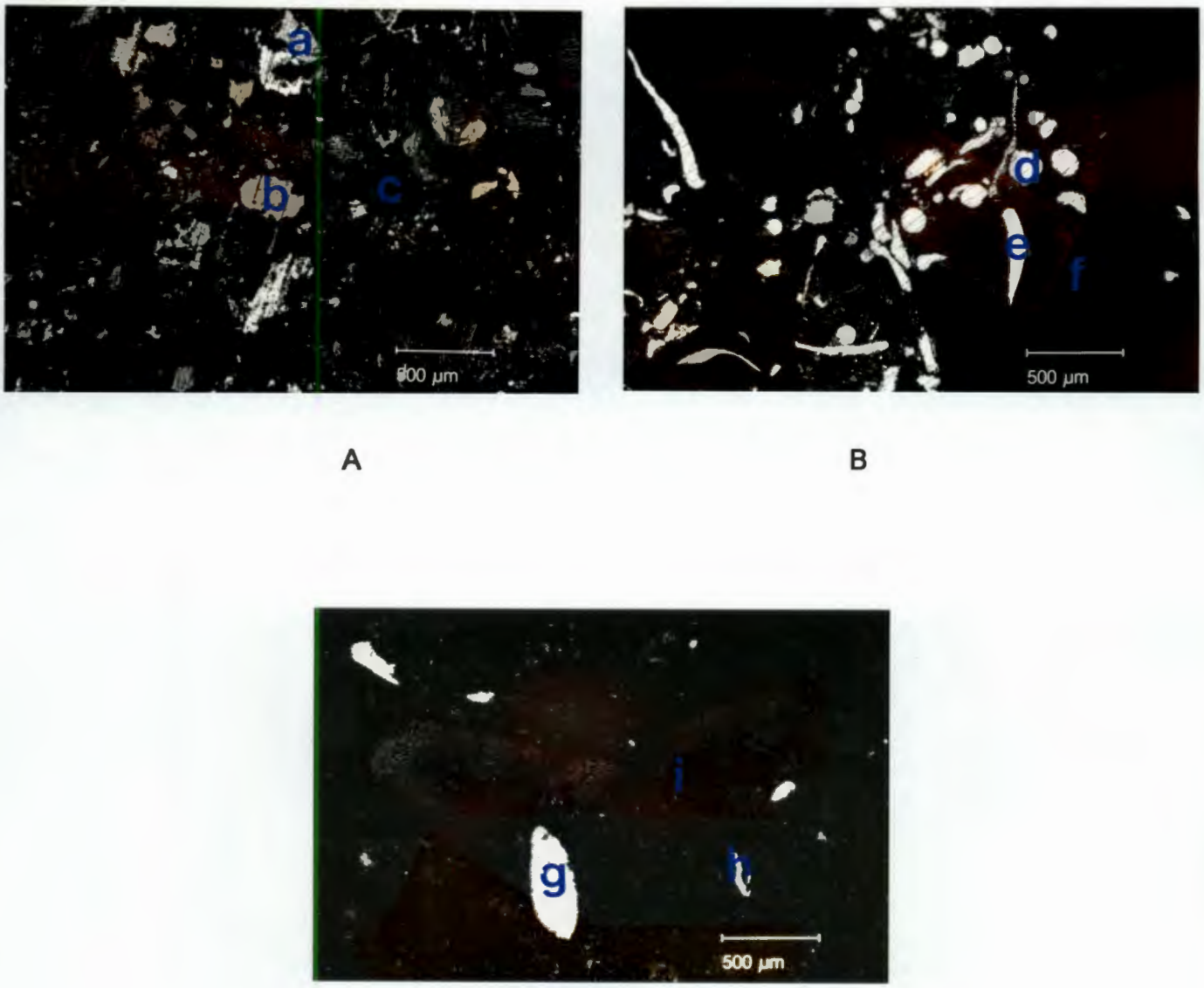

Fig 4.6: Optical micrographs of the friction lining materials A). organic pad. B). semi-metallic pad A. C). semi-metallic pad B.

Key for figure 4.6

a - copper	d - copper	g - copper
b - talc/mica	e - iron	h - iron
c - graphite/binder	f - graphite/binder	i - paper/binder

In the organic pad the organic (carbon) fibres, graphite, binder and paper are compressed to high density (2.49 g/cm^3). The organic fibres have a diameter of approximately 15μm and an average length of 250μm. The structure of the organic pad is revealed in fig 4.7.

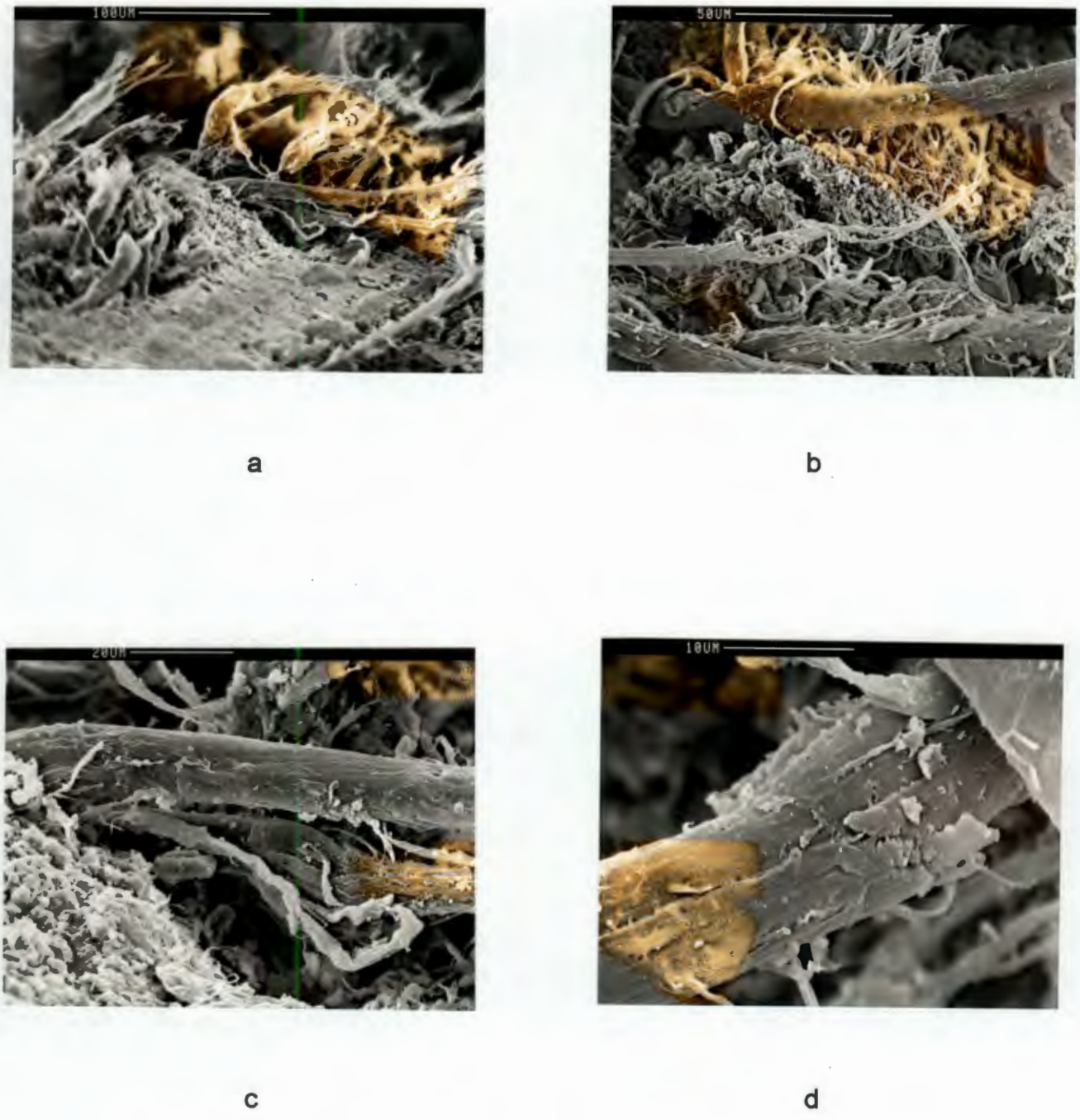

Fig 4.7: Structure of the organic pad a). general fibrous structure b). interaction of organic binder and fibres. c). loosened binder material attached to fibre d). cracking in organic fibre.

Semi-metallic pad A is more porous than the organic pad, although semi-metallic pad A has a higher overall density (3.12 g/cm^3) due to its high metallic constituent. The structure of semi-metallic pad A is shown in fig 4.8.

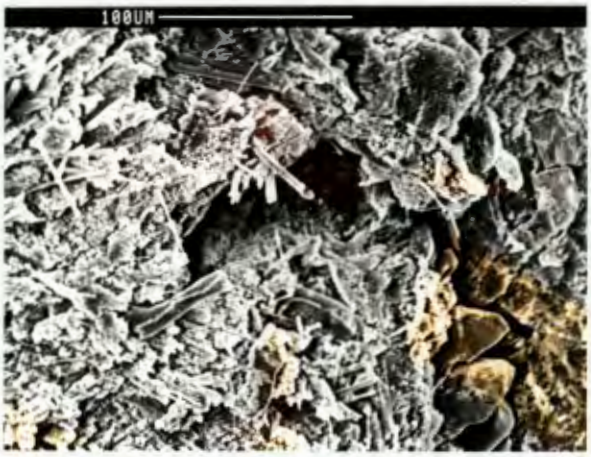

Fig 4.8: Structure of Semi-metallic pad A. The sharp angular metal chips can be seen in the bottom right hand corner of the micrograph. The rest of the micrograph shows metallic fibres enmeshed in a matrix of phenolic binder, rubber and graphite.

Semi-metallic pad B is very densely compacted, but has the lowest overall density (2.36 g/cm^3) due to its large paper content . The structure of semi-metallic pad B is shown in fig 4.9.

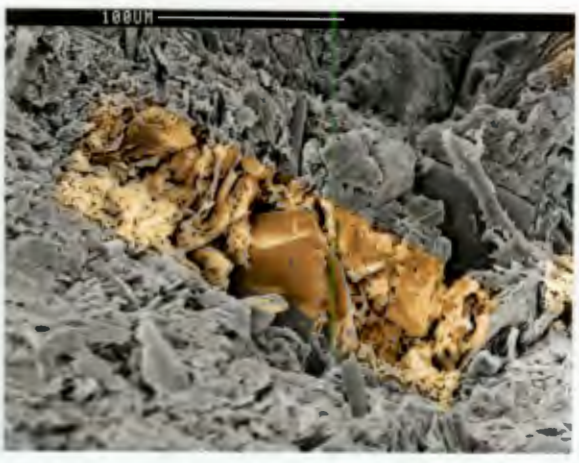

a

b

Fig 4.9: Structure of semi-metallic pad B a). general structure of the pad showing alumina particle embedded in a matrix of paper and organic binder. Alumina particles are an average of 150μm in diameter. b). magnified view of alumina particle in (a)

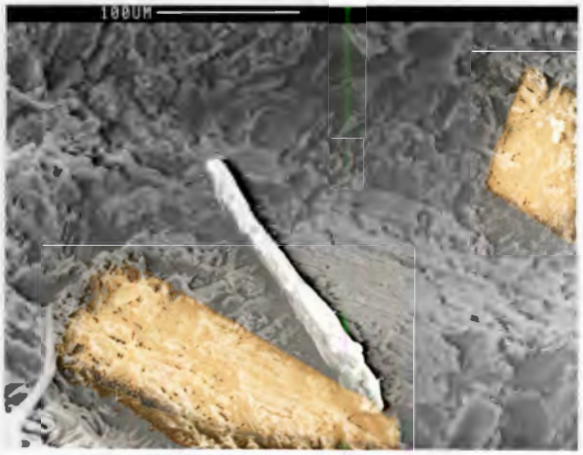

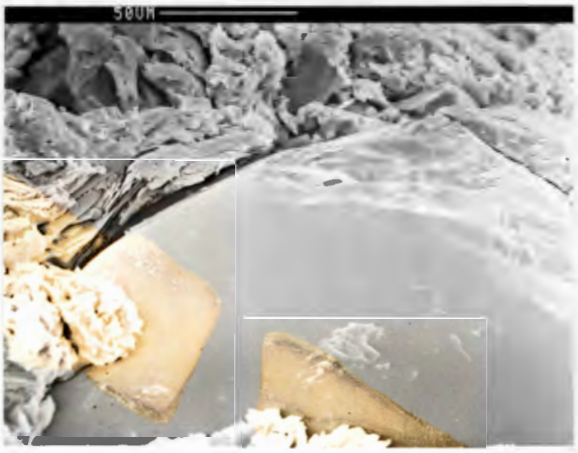

c d

Fig 4.9 Structure of semi-metallic pad B c). loose copper strip from pad. The average length of the copper strips in semi-metallic pad B is 200 μm d). micrograph showing poor bonding between pad material and an alumina particle within the pad.

4.3 *Testing phase-1 results*

* For a revision of testing phase-1 materials, consult table 3.3.

4.3.1 *Friction traces (rotor materials vs organic pad)*

Friction traces generated during the sliding of testing phase-1 materials against the organic pad are shown in fig 4.10. Both the A357 MMC and cast iron display a stable coefficient of friction over most of the sliding distance at all velocities. The unreinforced A357 aluminium was tested at the lowest sliding velocity only. This was due to the fact that this material experienced more than five times the wear of the other two rotor materials after sliding a tenth of their sliding distance. The mechanism of wear, therefore, for this material is much the same at higher velocities until the melt wear regime is reached.

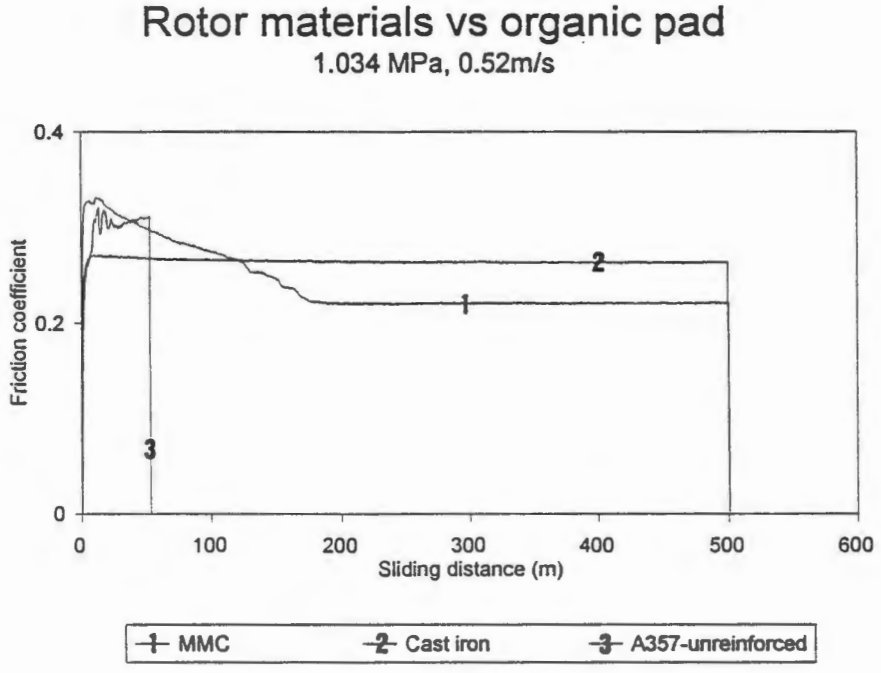

a

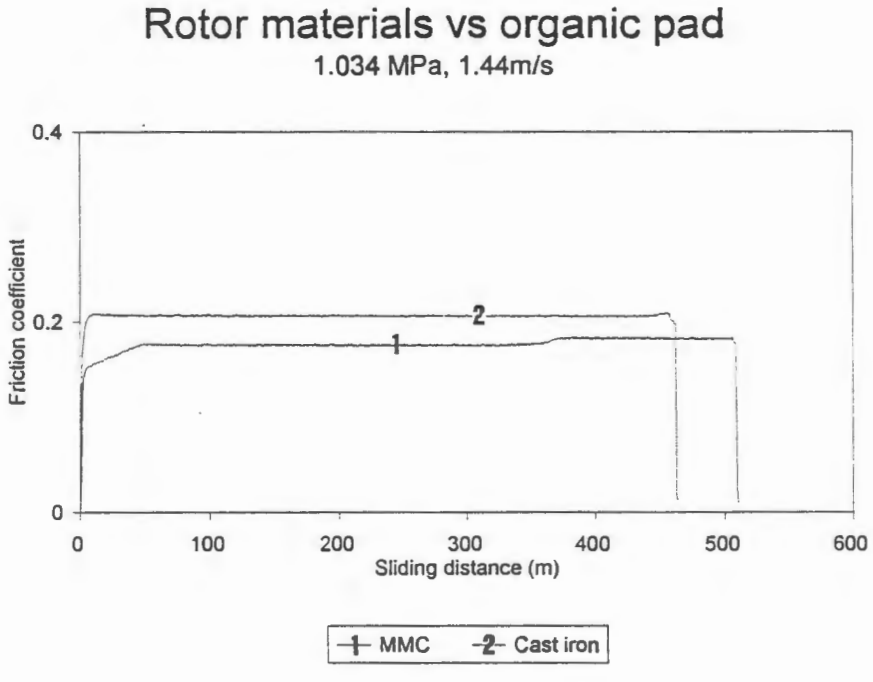

b

Fig 4.10a&b: Testing phase-1 friction traces of the A357 MMC, cast iron and the unreinforced A357 sliding against organic pad under a load of 1.034 MPa. a). All three materials at a sliding velocity of 0.52 m/s. b). Only the A357 MMC and cast iron at 1.44m/s.

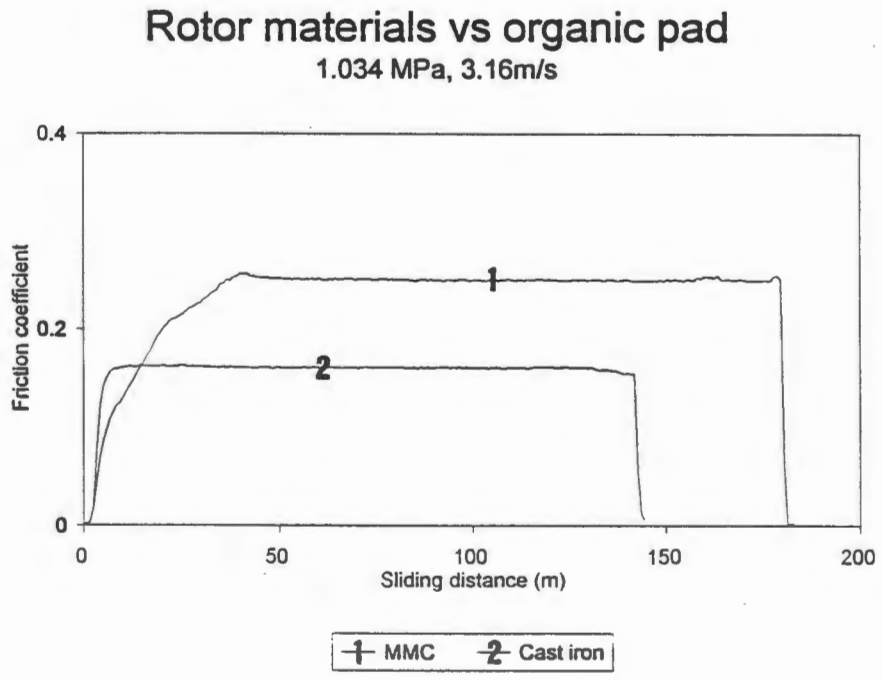

C

Fig 4.10c: Testing phase-1 friction traces of the A357 MMC, cast iron and the unreinforced A357 sliding against organic pad under a load of 1.034 MPa. c). Only the A357 MMC and cast iron at 3.16 m/s.

4.3.1.1 *The influence of sliding velocity on friction and wear*

The influence of sliding velocity on the steady state coefficient of friction for rotor materials sliding against organic pad is shown in fig 4.11. The A357 MMC first shows a decrease in friction coefficient with increasing sliding velocity and then a rapid increase.

Cast iron shows a decrease in friction coefficient over all sliding velocities - fig 4.11. This result (fade) is consistent with that of other researchers[7,8]. The unreinforced A357 alloy has the highest friction coefficient at the lowest sliding velocity.

The largest percentage deviation from the mean (8%) was recorded for the A357 MMC at 3.16m/s sliding velocity. This error limit is included in fig 4.11.

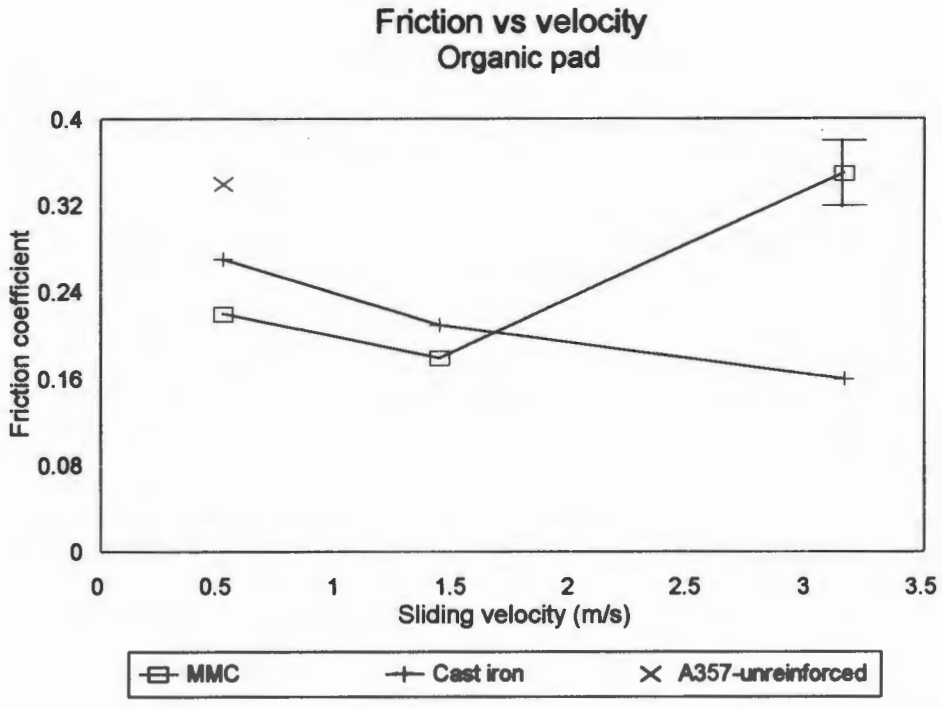

Fig 4.11: The relationship between steady state friction coefficient and sliding velocity for testing phase-1 materials sliding against the organic pad.

The concept of "Allowable wear rates" is important from an economic point of view in the engineering of modern automobile braking systems. Conventional cast iron brake rotors have a design life of 40 000 kilometres on average. If aluminium MMCs are to be competitive, they need to have a comparable "Kilometres in service" before replacement. The allowable wear rate for aluminium MMC brake rotors will be different to that of cast iron brake rotors of identical dimensions due to their difference in density.

For a brake rotor with average dimensions aluminium MMCs will have an allowable wear rate of 3.18×10^{-11} $g.Pa^{-1}.m^{-1}$ whilst cast iron will have an allowable wear rate of 7.82×10^{-11} $g.Pa^{-1}.m^{-1}$. (For derivations of allowable wear rates consult Appendix 1). These two limits are marked on all graphs of rotor material wear rate versus sliding velocity. The allowable wear rate for aluminium MMCs is indicated by the horizontal line marked 'A' and the allowable wear rate for cast iron is indicated by the horizontal line marked 'B' on all the graphs of rotor material wear rate versus velocity. It must be stressed, however, that the inclusion of wear limits in the wear rate versus velocity graphs is a qualitative tool to aid in performance comparisons between

aluminium MMCs and cast iron. The wear rate for these rotor materials during actual vehicle testing is expected to be lower than that recorded in this thesis. This is due to differences in geometry which allow for higher rates of thermal energy dissipation from the wear interface during actual vehicle testing.

Figure 4.12a illustrates the relationship between wear rate and sliding velocity for rotor materials sliding against the organic pad. Wear rate increases with increasing sliding velocity for the MMC and cast iron rotor materials. Over the sliding velocity range, the A357 MMC has a comparable, if not higher wear resistance than the cast iron. At the highest sliding velocity, the wear rate of both the A357 MMC and cast iron exceed their allowable wear rates. Note the high wear rate of the unreinforced A357 material (fig 4.12a) and its correspondingly high pad wear rate (fig 4.13b). The A357 MMC and the cast iron generate close to the same amount of pad wear in the organic pad - fig 4.12b.

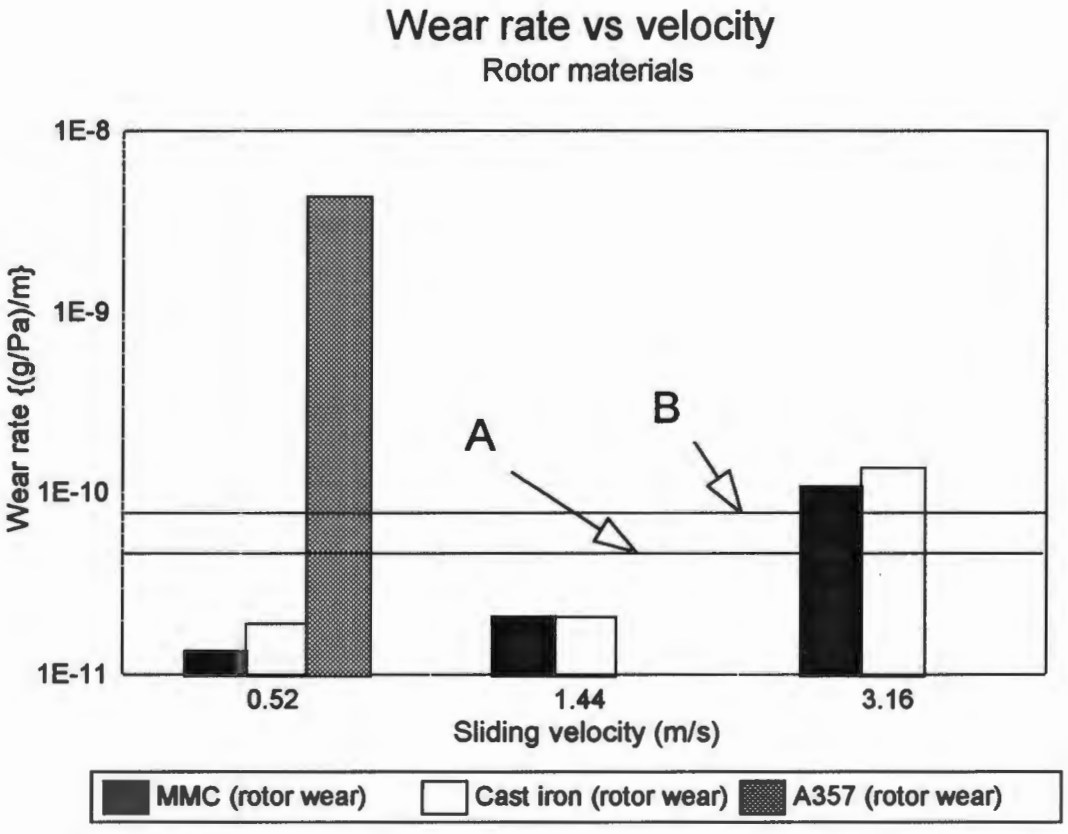

Fig 4.12a: The relationship between rotor material wear rate and sliding velocity for testing phase-1 rotor materials sliding against the organic pad. Note that 1E - 11 on the Y-axes indicates a wear rate of 1×10^{-11} $g.Pa^{-1}.m^{-1}$. Lines A and B indicate the allowable wear rates of the MMC and cast iron respectively.

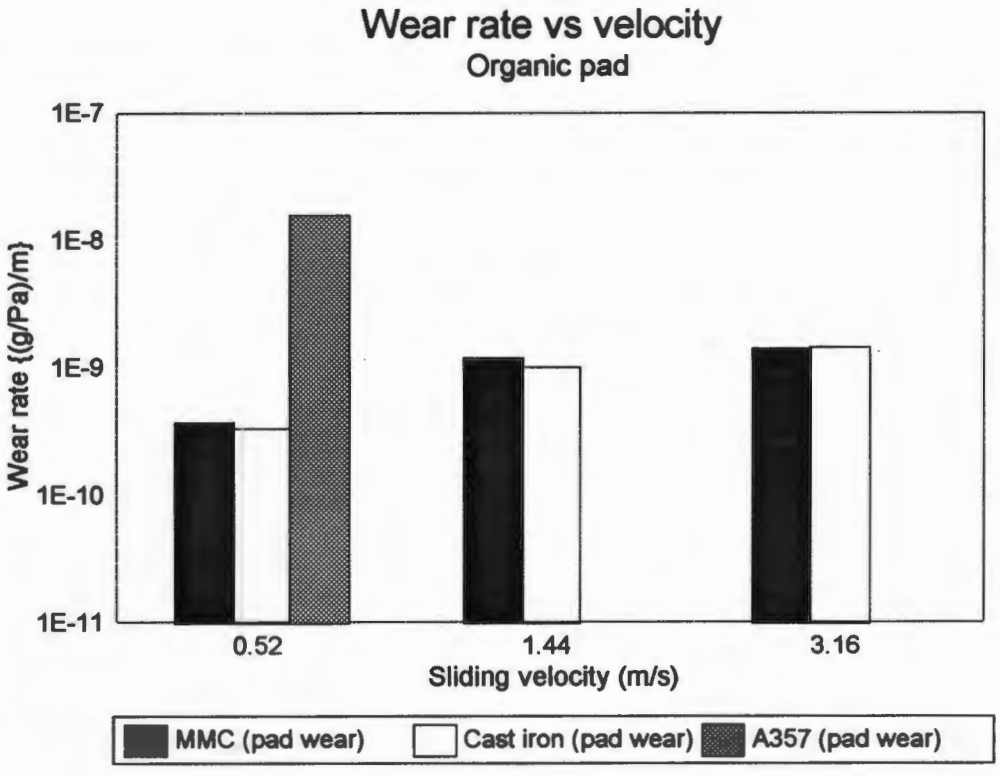

Fig 4.12b: The relationship between pad wear rate and sliding velocity for testing phase-1 rotor materials sliding against the organic pad. Note that 1E - 11 on the Y-axes indicates a wear rate of 1×10^{-11} $g.Pa^{-1}.m^{-1}$.

4.3.1.2 *Characterisation of wear surfaces*

Macro inspection of the wear surfaces of the A357 MMC and its matrix worn against the organic pad (fig 4.13) reveals the formation of a smooth and continuous solid lubricant layer on the MMC-worn pad surface at the lowest sliding velocity - fig 4.13A. As sliding velocity increases, this layer looses its continuity - fig 4.13B&C. The excessive pad wear induced by the unreinforced A357 material at the lowest sliding velocity is apparent in fig 4.13D.

Figure 4.13...

Fig 4.13: Macro photograph of organic pad and corresponding cylinder wear surfaces. A). A357 MMC and organic pad wear surfaces for a sliding velocity of 0.52m/s. B). A357 MMC and organic pad wear surfaces at 1.44m/s. C). A357 MMC and organic pad wear surfaces at 3.16m/s. D). A357 unreinforced alloy and organic pad wear surfaces at 0.52m/s. Large amounts of pad and aluminium wear debris have been displaced to the perimeter of the pad. The flaky wear closer to the centre of the pad is graphite. There is no evidence of a solid lubricant layer on the unreinforced A357 wear surface.

The solid lubricant layer has more continuity on the wear surface of the cast iron than on the wear surface of the A357 MMC - fig 4.14. On the MMC surface this layer coagulates in patches(black). A thin continuous layer forms on the cast iron surface. Shear is partially dissipated by the cracking of this layer.

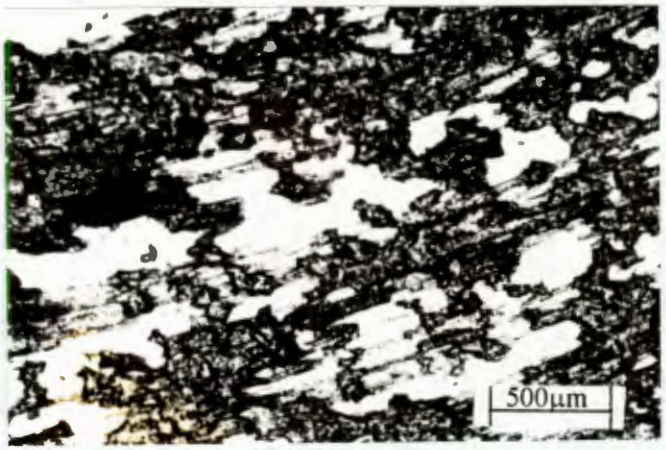

a

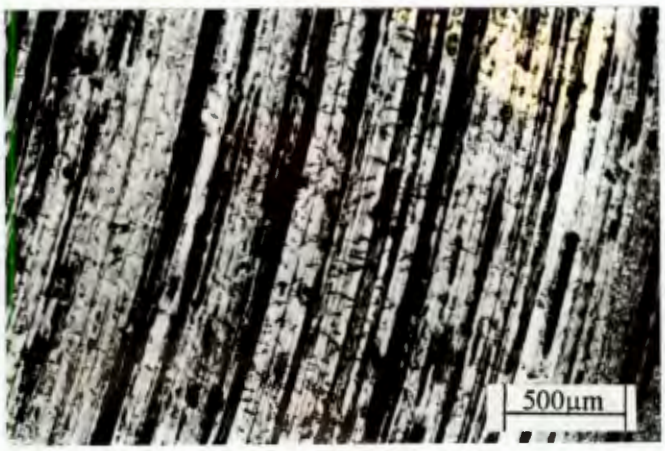

b

Fig 4.14: Optical micrographs of the wear surface of the A357 MMC and cast iron worn against the organic pad at a sliding velocity of 0.52 m/s and under a load of 1.034 MPa. a). MMC wear surface displaying a discontinuous solid lubricant layer. b). cast iron wear surface, displaying a fine wear scar topography and cracking in the solid lubricant layer.

Scanning electron microscopy of the A357 MMC worn surfaces identified a solid lubricant layer approximately 250μm thick. This solid lubricant layer is shown in fig 4.15. The layer was absent on the wear surface of the unreinforced A357. The presence of a solid lubricant layer was also identified on the cast iron surface although it was thinner than that for the A357 MMC.

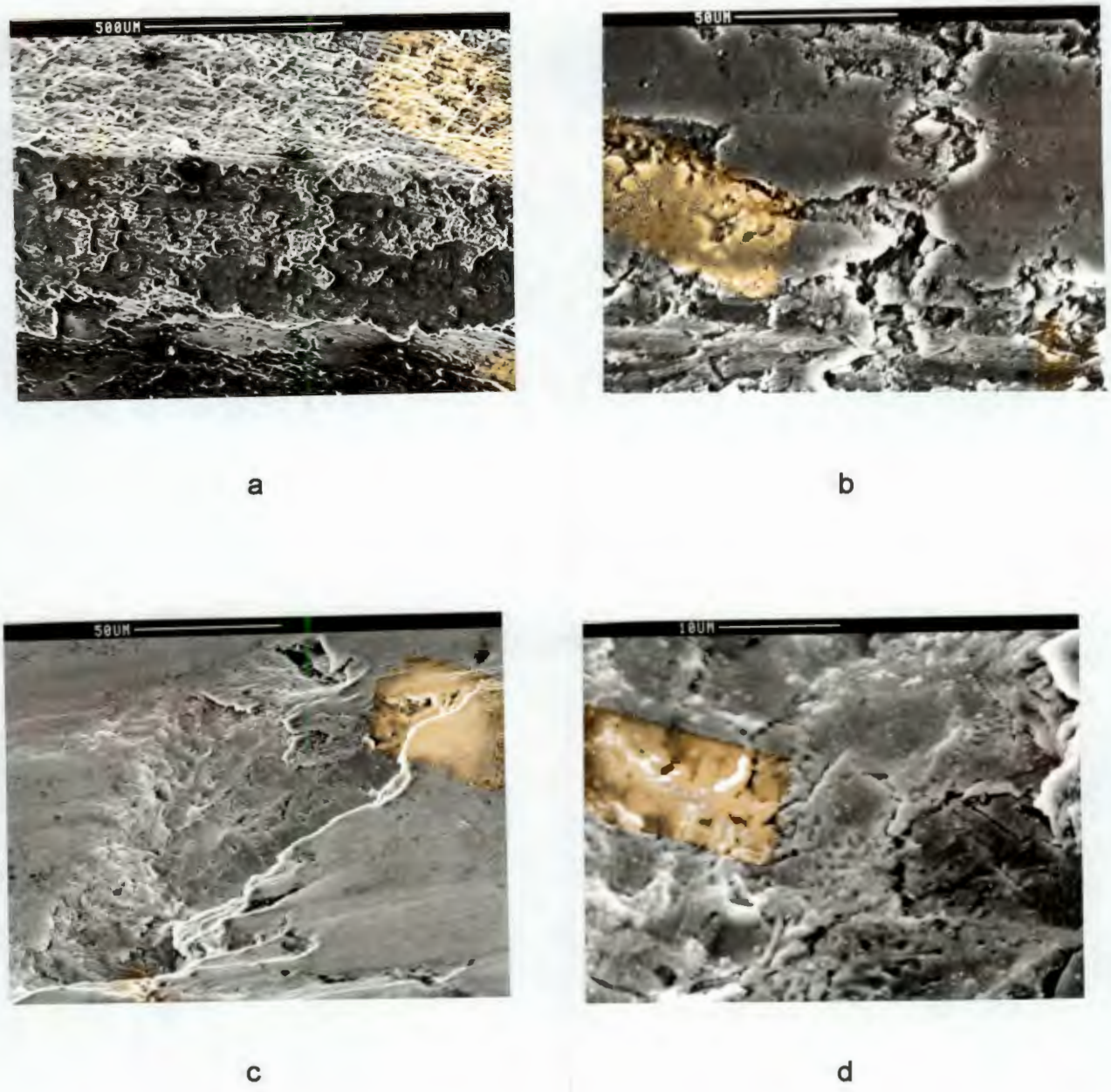

Fig 4.15: Solid lubricant layer on the surface of the A357 MMC after sliding against organic pad under a load of 1.034 MPa and a sliding velocity of 0.52 m/s. a). Edge on view of the layer, showing a layer thickness of approximately 250μm. The top third of the photograph is the wear surface, the middle third reveals the thickness of the layer and the bottom third is the bulk MMC material. b). Magnification of the edge on view of the layer in (a) above. Note the lubricative nature of the layer and hence its capacity for shear dissipation at the wear interface. c). accumulation of the solid lubricant layer in hole on cast iron wear surface. d). structure of layer in hole.

Figure 4.16 shows the wear surface of the A357 MMC after sliding against the organic pad at 3.16m/s. Material in the right hand corner of the micrograph is closest to the centre of the cylinder.

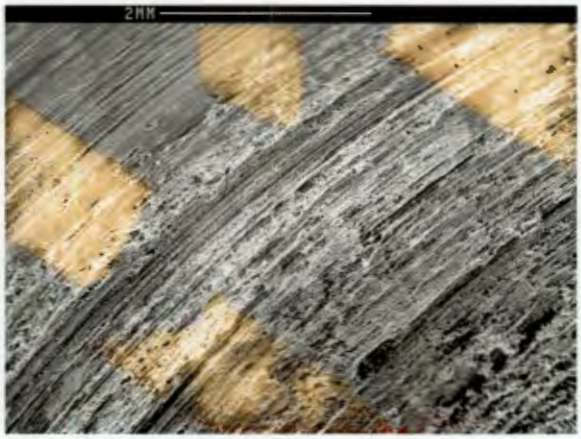

Fig 4.16: Wear surface of the A357 MMC after sliding against the organic pad at 3.16 m/s.

No evidence of fractured SiC particulates was found upon inspection of solid lubricant layers on the wear surfaces of the A357 MMC at all sliding velocities against the organic pad.

4.3.2 *Friction traces (rotor materials vs semi-metallic pad A)*

Friction traces for rotor materials worn against semi-metallic pad A are displayed in fig 4.17. From fig 4.17 the relationship between coefficient of friction and sliding distance for the A357 MMC is irregular over all sliding velocities and there is no clear relationship between the friction coefficient of the A357 MMC and sliding distance or sliding velocity. This fact in itself, however, provides useful information. Cast iron displays stable frictional properties with sliding distance, but a decrease in friction coefficient with sliding distance at the highest sliding velocity - fig 4.17. The unreinforced A357 displays a stable coefficient of friction over the distance tested at the lowest sliding velocity but experiences more than a hundred times the wear rate of the cast iron at the same sliding velocity - fig 4.18.

Tests for the MMC sliding against semi-metallic pad A at the lowest and highest velocity (friction trace 1 in fig's 4.17a&c) were terminated before steady states were reached in order to prevent damage to the torque cell. A steady state coefficient of friction for the MMC was attained at 1.44m/s (fig 4.17b) after melt

wear was allowed to proceed. The steady state friction coefficient for cast iron first increases and then decreases with increasing sliding velocity - fig 4.17.

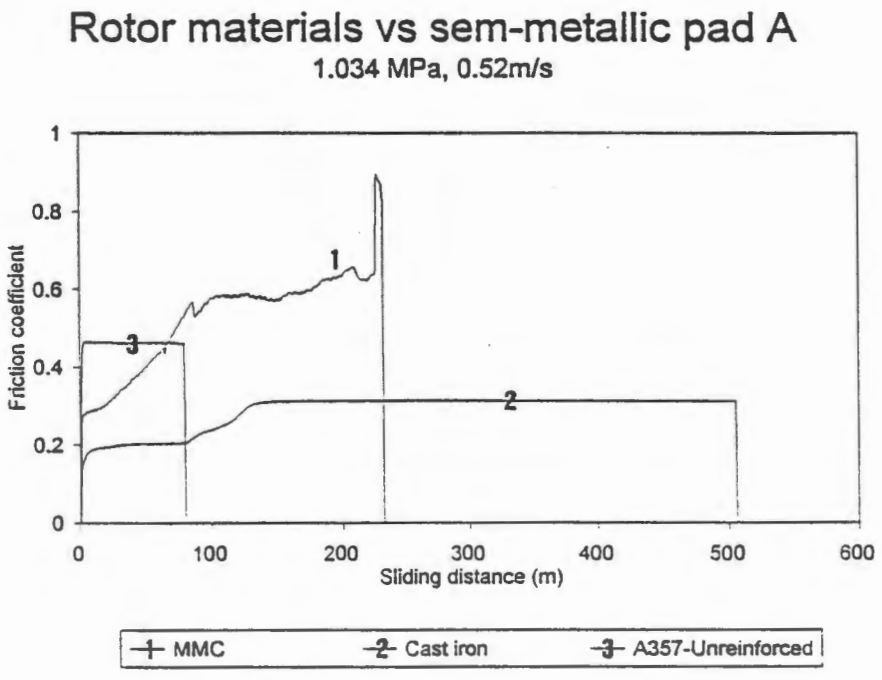

a

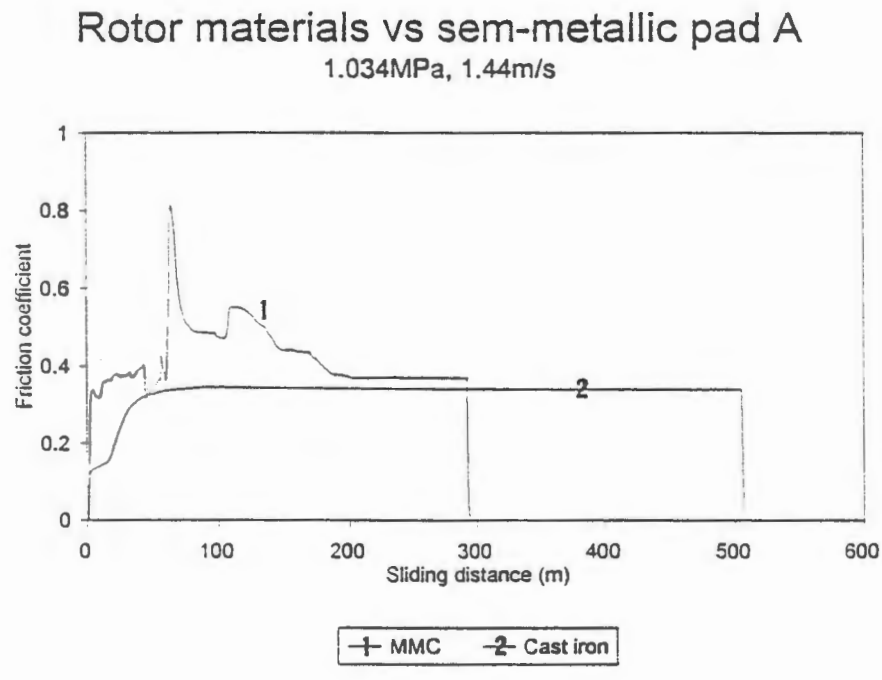

b

Fig 4.17a&b: Testing phase-1 friction traces of the A357 MMC, cast iron and the unreinforced A357 sliding against seem-metallic pad A under a load of 1.034 MPa. a). All three materials at a sliding velocity of 0.52 m/s. b). Only the A357 MMC and the cast iron at 1.44 m/s.

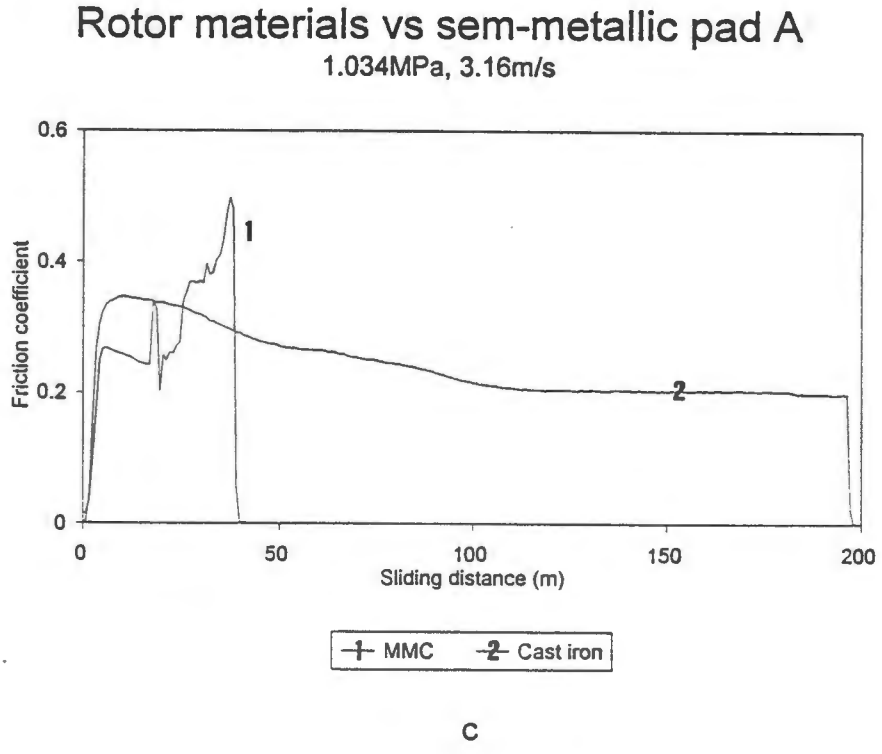

Fig 4.17c: Testing phase-1 friction traces of the A357 MMC, cast iron and the unreinforced A357 sliding against seem-metallic pad A under a load of 1.034 MPa. c). Only the A357 MMC and cast iron at 3.16 m/s.

4.3.2.1 *The influence of sliding velocity on wear (rotor materials vs semi-metallic pad A)*

The relationship between wear rate and sliding velocity for rotor materials sliding against semi-metallic pad A is shown in fig 4.19a. Note the poor wear resistance of the A357 MMC and the unreinforced A357 alloy compared with the high wear resistance of the cast iron. The wear rate for the A357 MMC far exceeds its allowable wear rate (line A, fig 4.19a) over all sliding velocities whilst the wear rate for cast iron is within its allowable rate (line B, fig 4.19a) over all sliding velocities.

The wear rate of semi-metallic pad A is shown in fig 4.19b. The negative pad wear induced by the A357 MMC illustrated at 1.44m/s indicates MMC melt transfer to the pad. This melt wear corresponds with friction trace 1 in fig 4.18b.

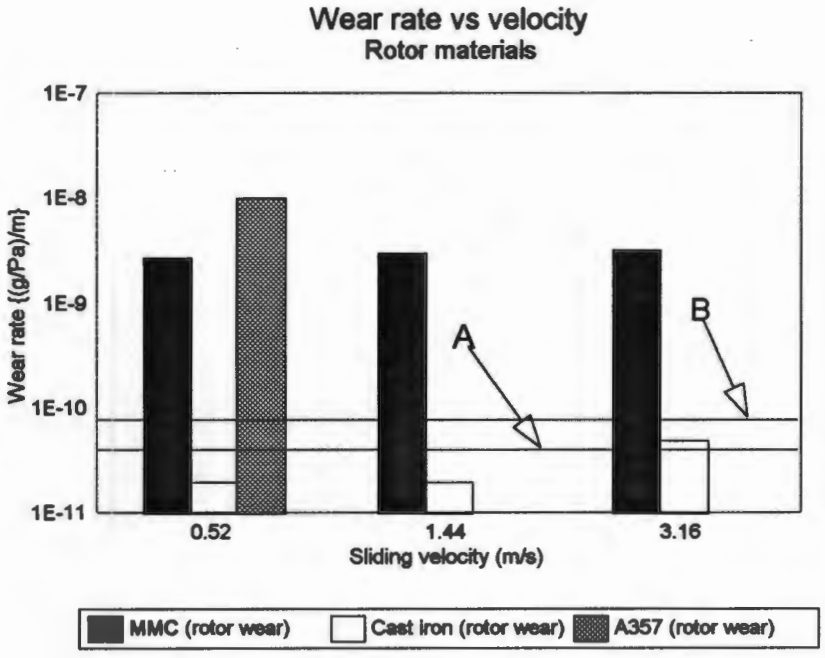

Fig 4.18a: The relationship between rotor material wear rate and sliding velocity for testing phase-1 rotor materials sliding against semi-metallic pad A. Note that 1E - 11 on the Y-axes indicates a specific wear of 1×10-11 $g.Pa^{-1}.m^{-1}$. Lines A and B indicate the allowable wear rates of the MMC and cast iron respectively.

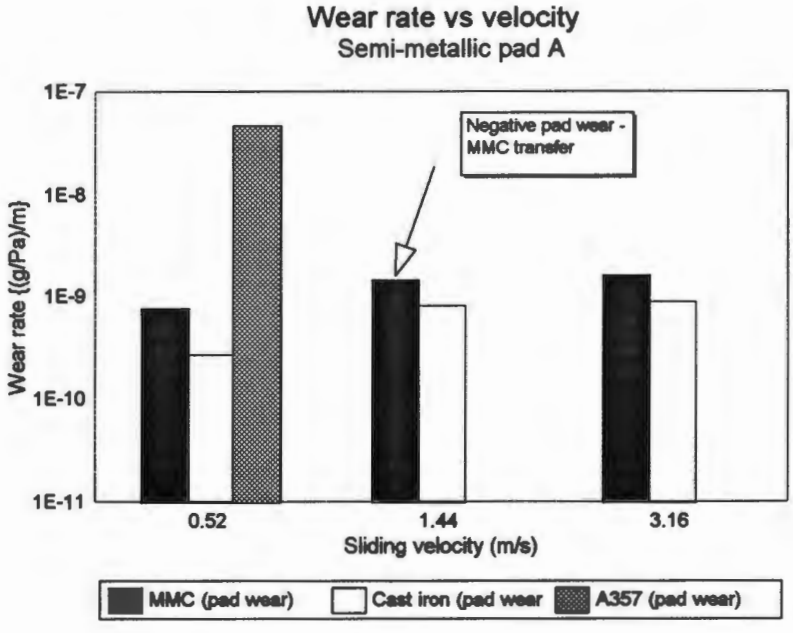

Fig 4.18b: The relationship between pad wear rate and sliding velocity for testing phase-1 rotor materials sliding against semi-metallic pad A. The MMC induced pad wear illustrated at 1.44m/s is a negative pad wear which denotes MMC transfer to pad. Transfer of cast iron or unreinforced A357 to the pad did not occur.

4.4 *Testing phase-2 results:*

* For a review of testing phase-2 materials, consult table 3.4.

4.4.1 *Friction traces for low applied loads (517 KPa)*

Friction traces for rotor materials slid against semi-metallic pad B at 517 KPa load are displayed in fig 4.19. Although semi-metallic pad B has been specifically designed to be compatible with aluminium MMC rotors, the friction traces for the A359 MMC sliding against semi-metallic pad B show little consistency with increasing sliding distance and/or sliding velocity. In fact, fracture of SiC particulates occurs at the lowest sliding velocity at this low load - fig 4.20.

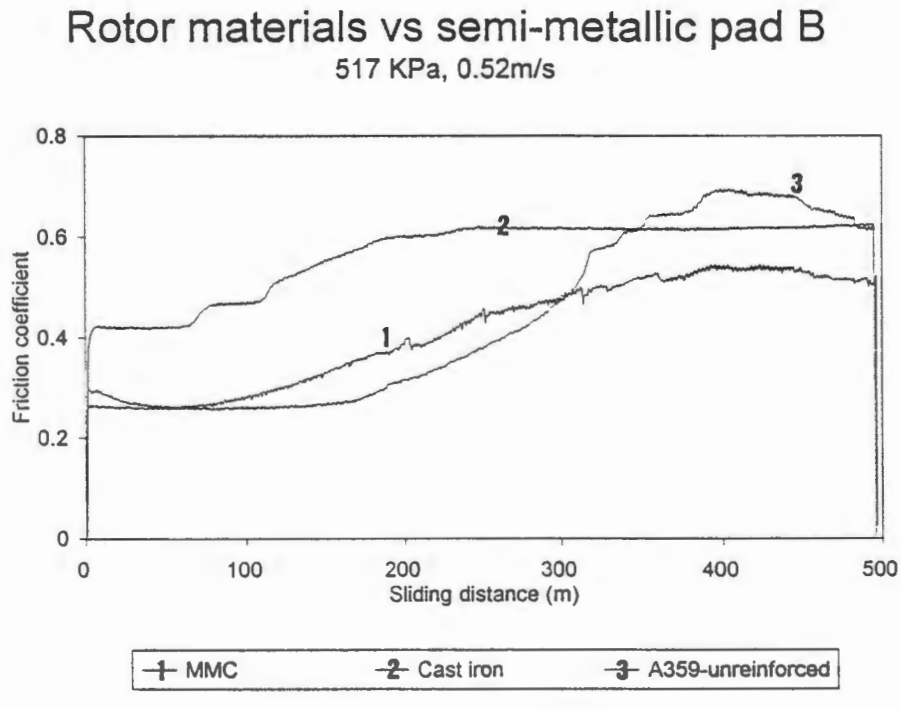

a

Fig 4.19a: Testing phase-2 friction traces of the A359 MMC, cast iron and the unreinforced A359 sliding against semi-metallic pad B under a load of 517 KPa and at a sliding velocities of 0.52 m/s.

Figure 4.19b&c...

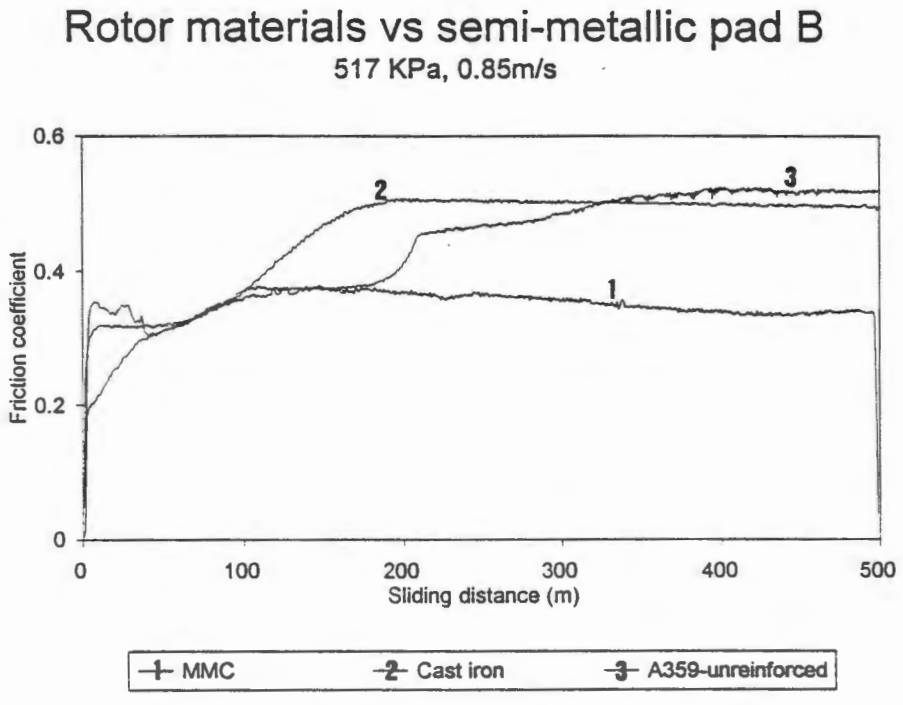

b

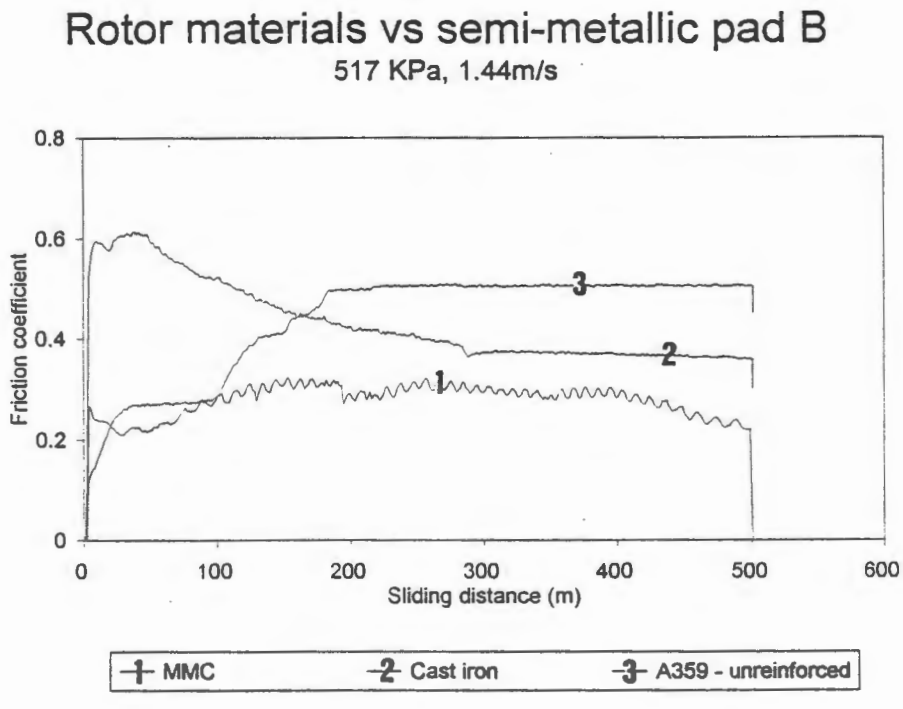

c

Fig 4.19b&c: Testing phase-2 friction traces of the A359 MMC, cast iron and the unreinforced A359 sliding against semi-metallic pad B under a load of 517 KPa and at sliding velocities of: b). 0.85 m/s. c). 1.44m/s

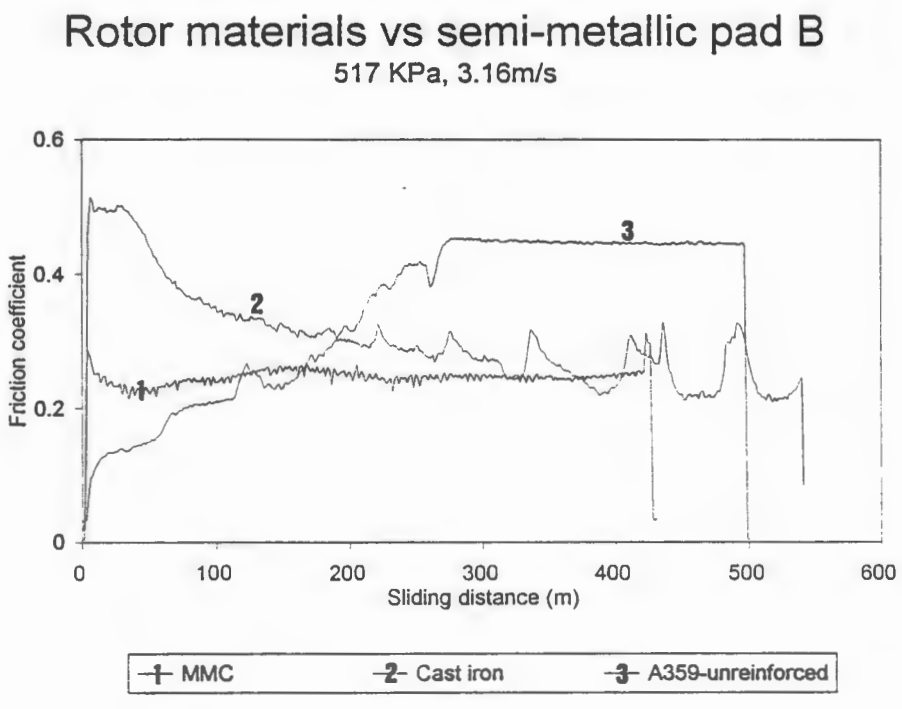

d

Fig 4.19d: Testing phase-2 friction traces of the A359 MMC, cast iron and the unreinforced A359 sliding against semi-metallic pad B under a load of 517 KPa and at a sliding velocities of 3.16 m/s.

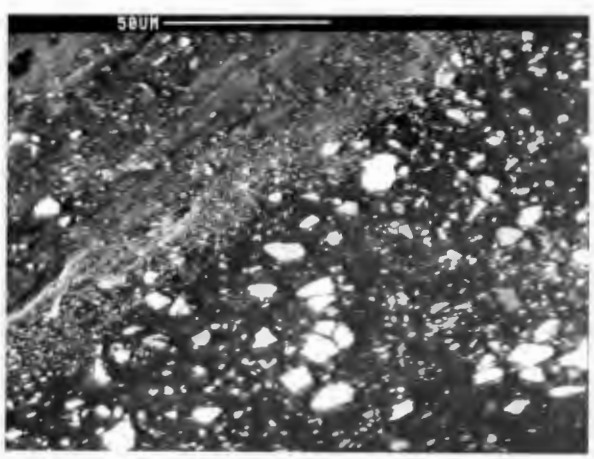

Fig 4.20: Fractured silicon carbide particulate and alumina debris within the thin wear layer formed on the surface of the A359 MMC after sliding against semi-metallic pad B under a load of 517 KPa and at a sliding velocity of 0.52 m/s.

4.4.1.1 *The influence of sliding velocity on wear*

The influence of sliding velocity on wear rate for rotor materials sliding against semi-metallic pad B at 517 kPa is shown in fig 4.21a.

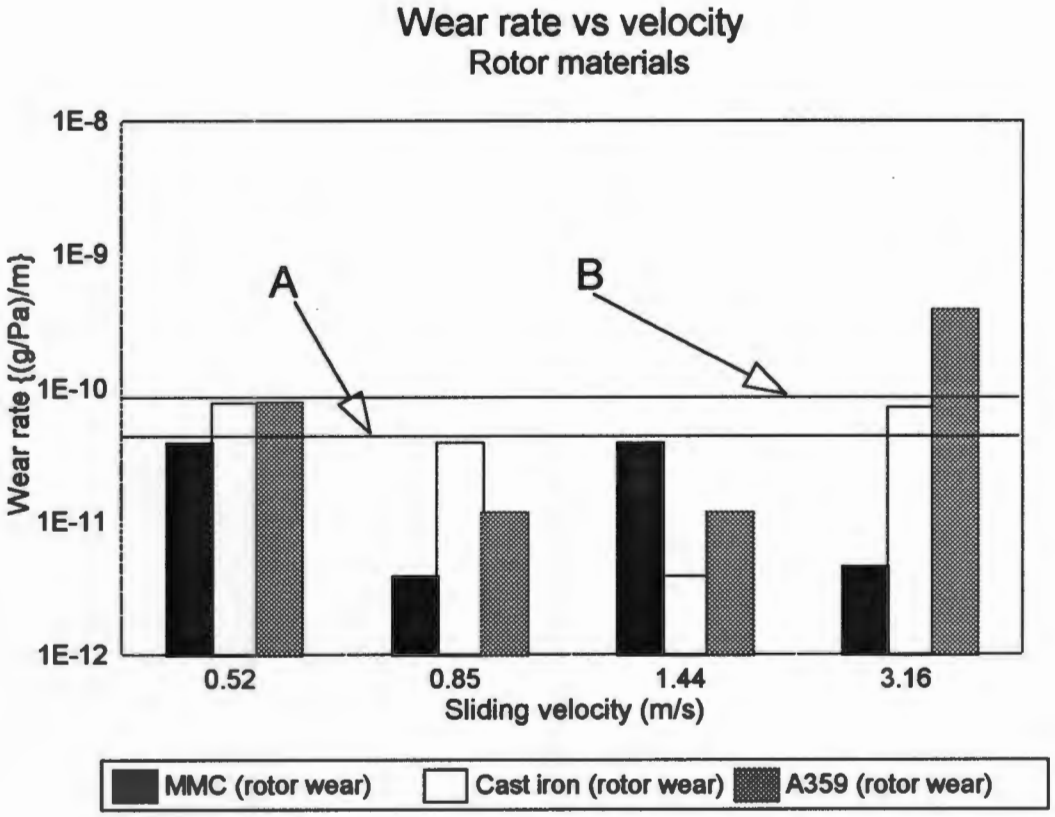

Fig 4.21a: The relationship between rotor material wear rate and sliding velocity for testing phase-2 rotor materials sliding against semi-metallic pad B under 517 KPa load. Note that 1E - 12 on the Y - axis indicates a specific wear of 1×10^{-12} g.Pa^{-1}.m^{-1}. Lines A and B indicate the allowable wear rates of the MMC and cast iron respectively.

The influence of sliding velocity on pad wear rate is shown in fig 4.21b.

Figure 4.21b...

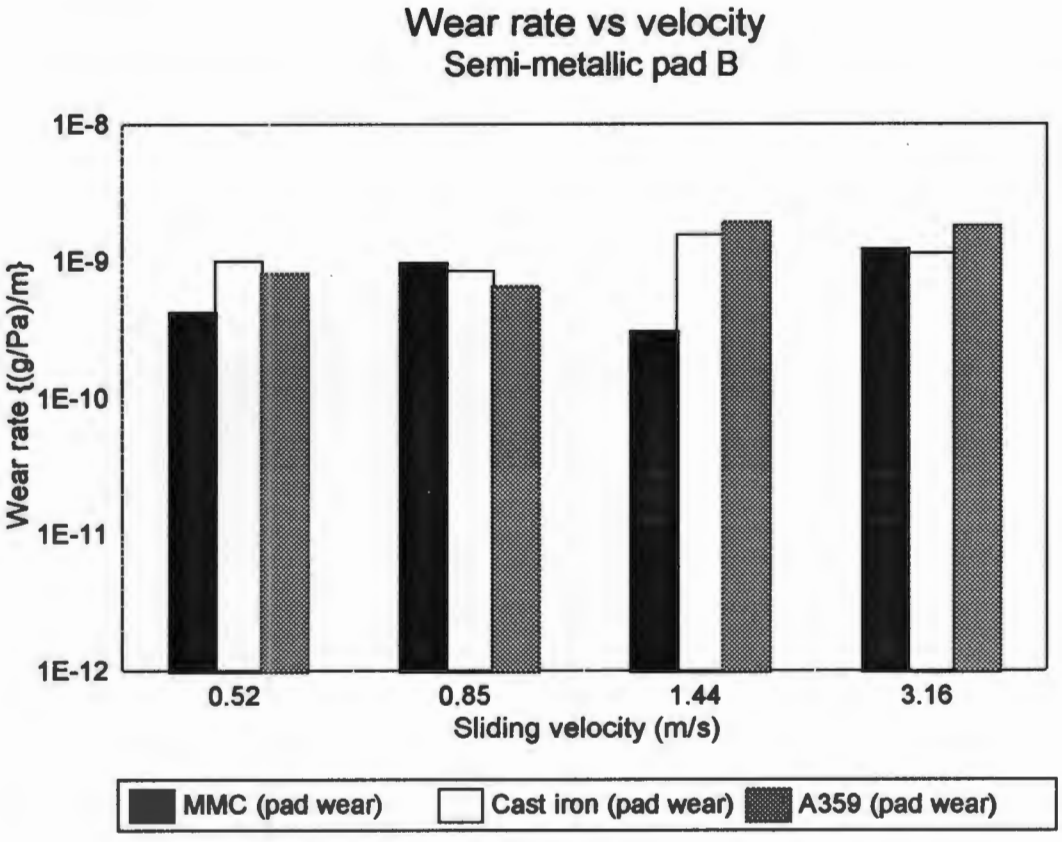

Fig 4.21b: The relationship between pad wear rate and sliding velocity for testing phase-2 rotor materials sliding against semi-metallic pad B under 517 KPa load. Note that 1E - 12 on the Y - axis indicates a specific wear of 1×10^{-12} g.Pa^{-1}.m^{-1}.

4.4.1.2 *The influence of sliding velocity on wear interface temperature*

An increase in sliding velocity leads to an increase in the average rate of wear interface temperature increase with sliding distance - fig 4.22. The average rate of wear interface temperature increase with sliding distance, dT/dS, is defined as the difference between the wear interface temperature at the end of the friction test and ambient temperature divided by the sliding distance for the specific friction test. In equation form:

$$\frac{dT}{dS} = (T_{final} - T_{ambient})/Sliding\ distance \quad \text{.....4.1}$$

Where T = Temperature (°C)
and S = sliding distance (m)

This rate of increase is higher, initially, for the unreinforced A359 but at the highest sliding velocity the rate of wear interface temperature increase with sliding distance is the same for all materials .

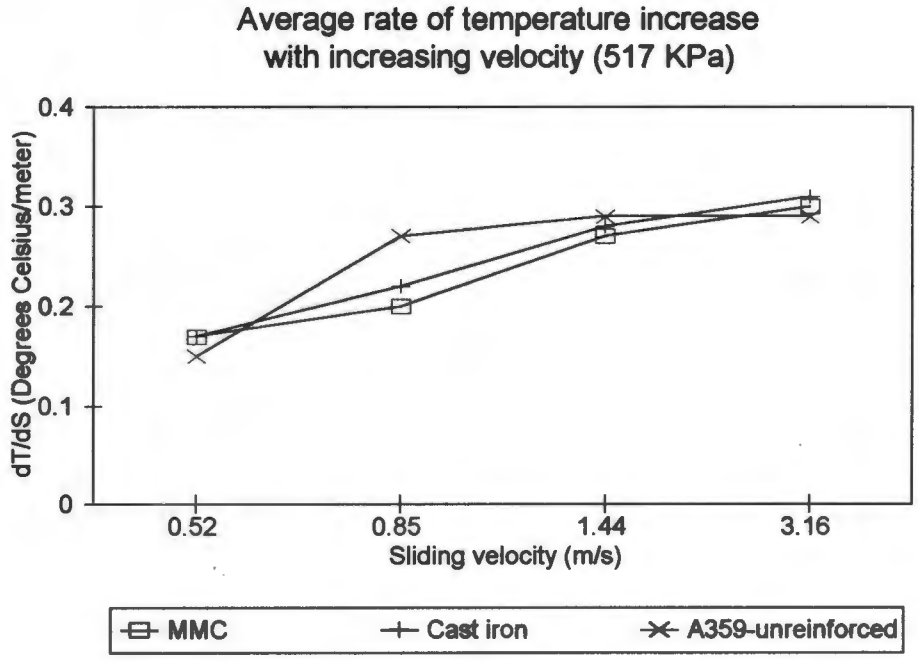

Fig 4.22: Graph of the relationship between sliding velocity and the rate of wear interface temperature increase for low applied loads.

4.4.1.3 *Wear modes*

Figure 4.23 displays A359 MMC matrix, unreinforced A359 alloy and cast iron steadite phase microhardness values in the near wear surface region of these materials worn against semi-metallic pad B at 517 KPa and 0.52m/s.

Figure 4.23...

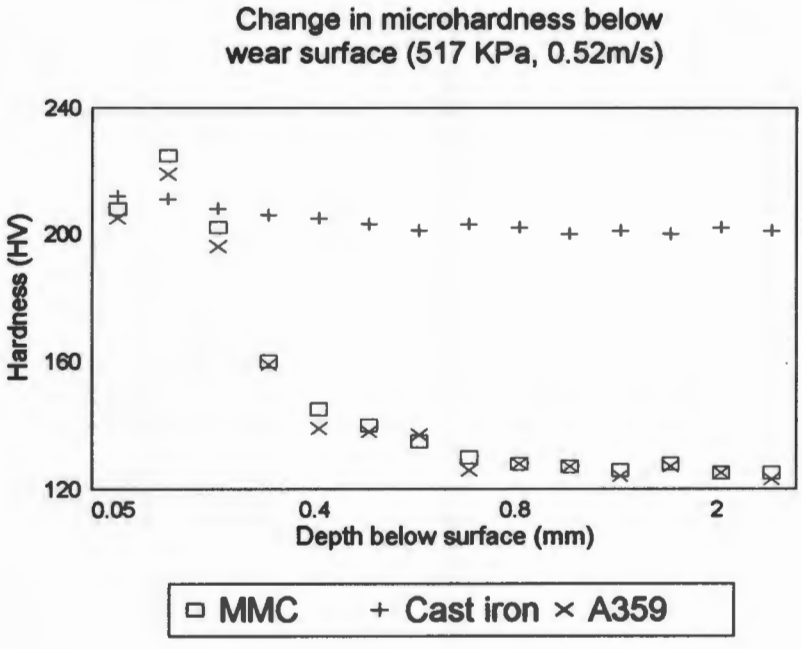

Fig 4.23: Microhardness of A359 MMC matrix, the unreinforced A359 alloy and steadite phase in cast iron.

Using backscattered electron microscopy in the analysis of the A359 MMC sectioned perpendicular to the wear surface, a clustering of copper particles was identified in a region not more than 50μm from the wear surface - fig 4.24. The energy of X-rays reflected from these particles during energy dispersive X-ray analysis corresponded closely with the K-line energy for copper.

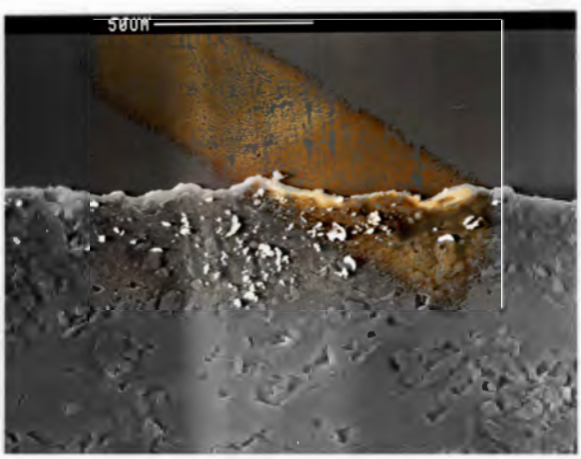

Fig 4.24: Backscattered electron micrograph of copper particles in the deformed near surface wear layer of the A359 MMC - 517 KPa, 0.52m/s.

Figure 4.25 shows the wear track of an alumina particle on the cast iron wear surface after sliding against semi-metallic pad B at 0.52m/s and 517 KPa load.

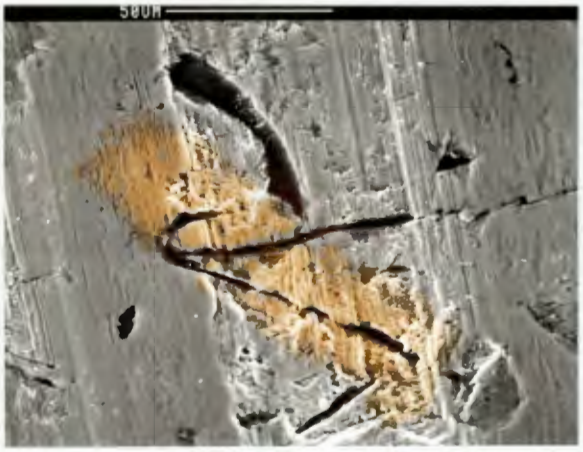

Fig 4.25: Wear track of an alumina particle on the cast iron surface with the brittle cracking as a direct result - 517 KPa load, 0.52m/s sliding velocity.

Wear in the unreinforced A359 occurs through scouring and ductile tearing - fig 4.26a and extrusion at the sides of the wear scar - fig 4.26b.

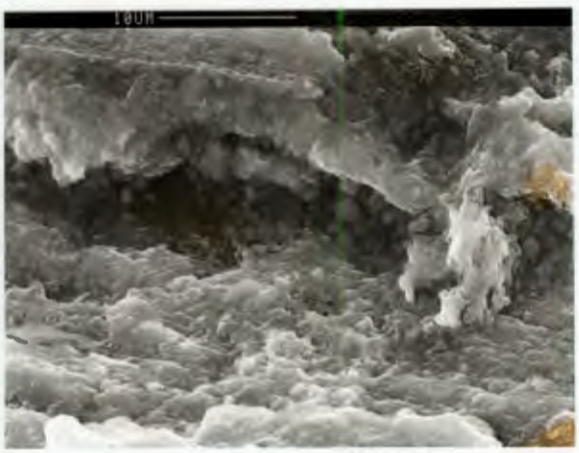

a

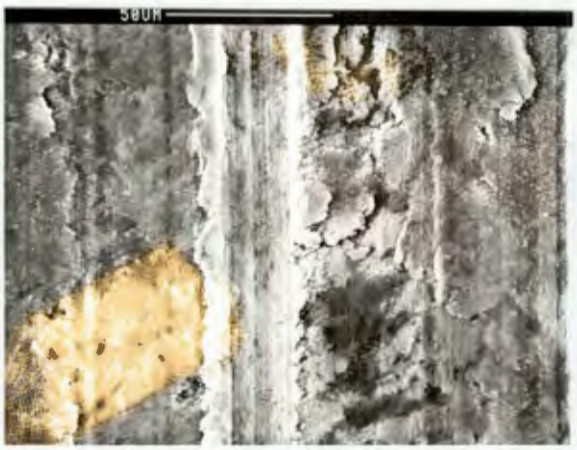

b

Fig 4.26: Wear mechanisms for unreinforced A359 sliding against semi-metallic pad B at low loads. a). electron micrograph of scouring/ductile tearing. b). electron micrograph of extrusion at the sides of the wear scar induced by an alumina particle within the pad.

Due to the low hardness of the unreinforced A359 wear surface, loose copper particles from the pad are often embedded into the A359 alloy wear surface. fig 4.27.

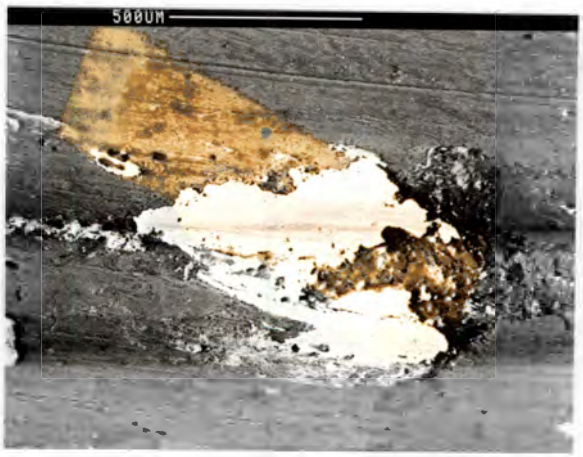

Fig 4.27: Backscattered electron micrograph of copper from the pad embedded in the unreinforced A359 wear surface - 517 KPa, 0.52m/s.

4.4.2 *Friction traces for high applied loads (1.034 MPa)*

Friction traces for rotor materials sliding against semi-metallic pad B at 1.034 MPa are displayed in fig 4.28. The higher load imparts a greater consistency to the friction traces apart for the traces of the A359 MMC and unreinforced A359 at the highest sliding velocity. Although the friction traces in fig 4.28 are irregular (compared with the friction traces in fig 4.10) and the margin of error large (see "Reproducibility of friction traces" - section 4.5), this irregularity, in itself, provides useful information.

Figure 4.28a&b...

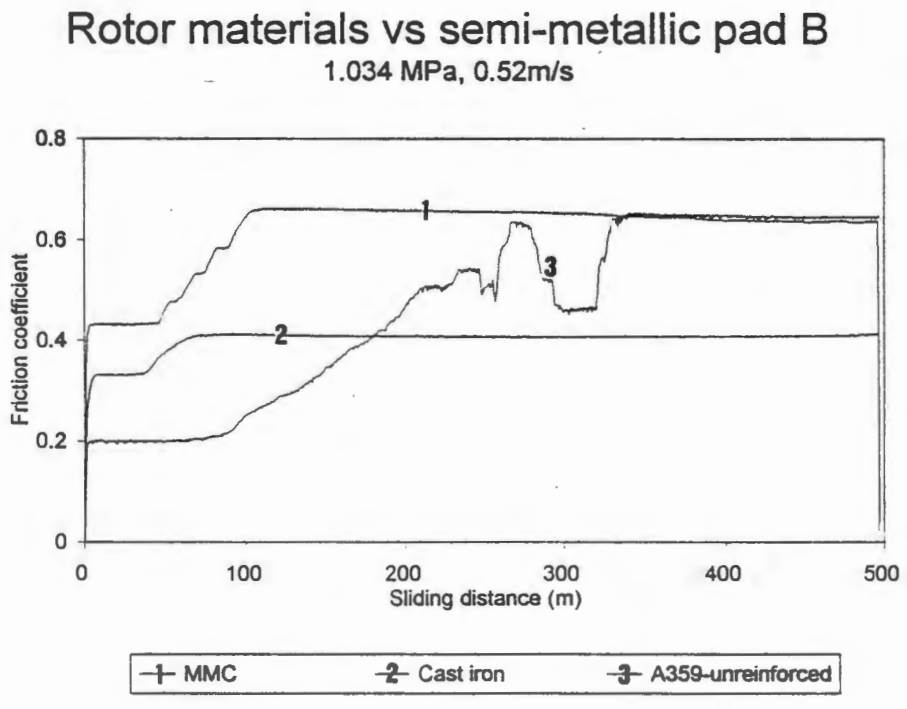

a

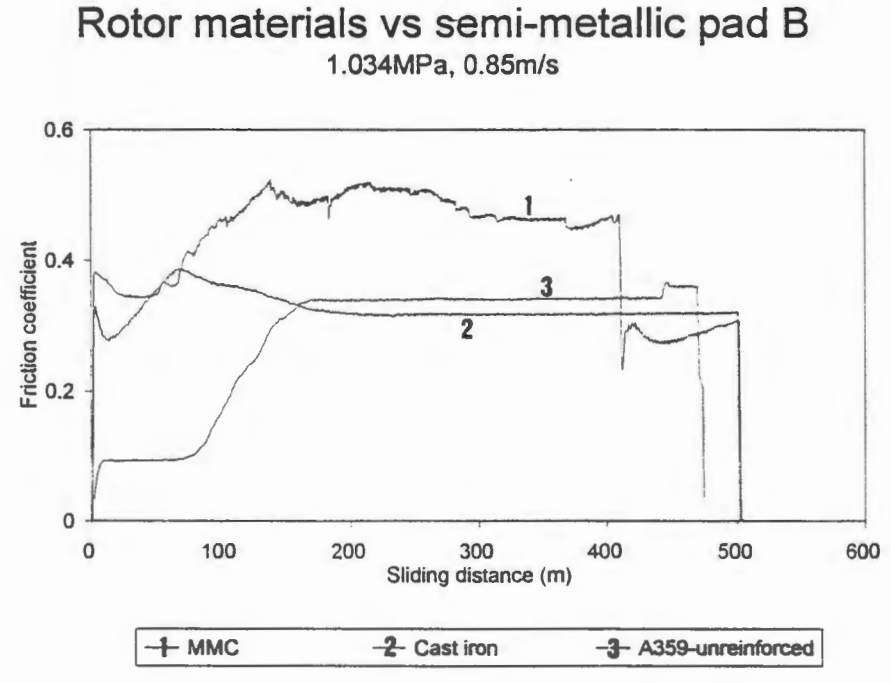

b

Fig 4.28a&b: Testing phase-2 friction traces of the A359 MMC, cast iron and the unreinforced A359 sliding against semi-metallic pad B under a load of 1.034 MPa and at sliding velocities of: a). 0.52 m/s b). 0.85 m/s.

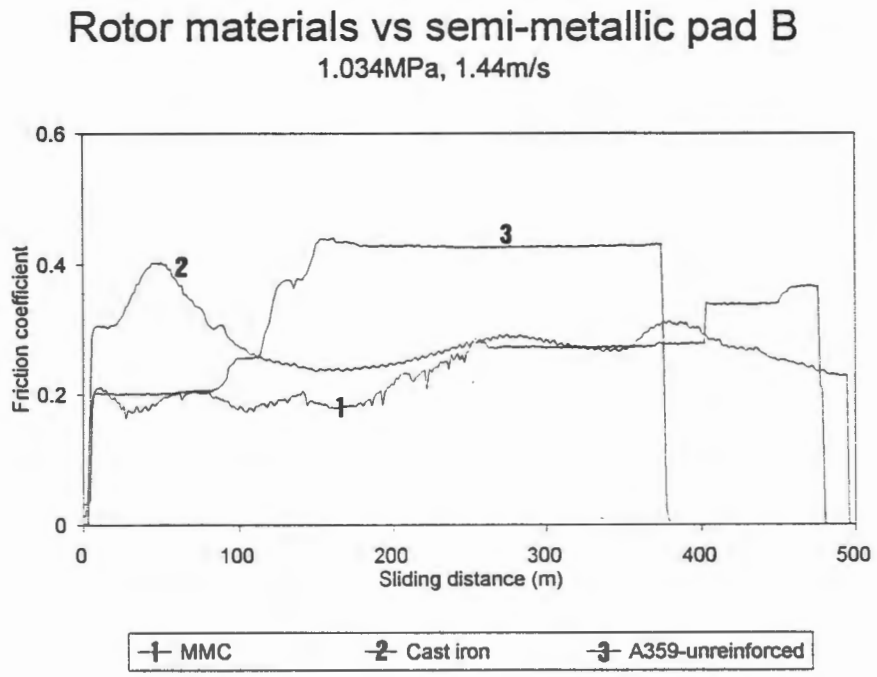

c

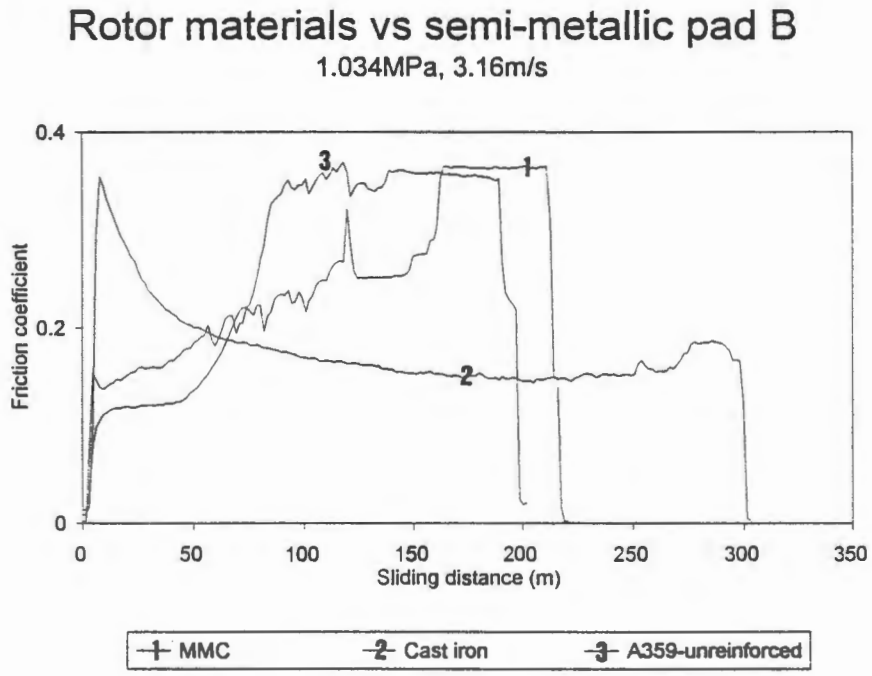

d

Fig 4.28c&d: Testing phase-2 friction traces of the A359 MMC, cast iron and the unreinforced A359 sliding against semi-metallic pad B under a load of 1.034 MPa and at sliding velocities of: c). 1.44 m/s d). 3.16 m/s.

4.4.2.1 *The influence of sliding velocity on wear*

The influence of sliding velocity on wear rate at high loads (1.034 MPa) is shown in fig 4.29. An increase in load leads to a sharp increase in wear rate with sliding velocity for the A359 MMC and the unreinforced A359 alloy whereas the cast iron experiences a decrease in wear rate over the first three sliding velocities and an increase at the highest velocity - fig 4.29a. The A359 MMC has greatly exceeded its allowable wear rate (line A fig 4.29a) at the highest three sliding velocities. The wear rate for cast iron is well below its allowable limit (line B fig 4.29a) for all sliding velocities . At the highest sliding velocity, the wear rate of the A359 MMC is higher than that of its unreinforced matrix the A359 alloy - fig 4.29a.

The A359 MMC and the unreinforced A359 alloy both induce higher pad wear rates than the cast iron over all sliding velocities - fig 4.29b.

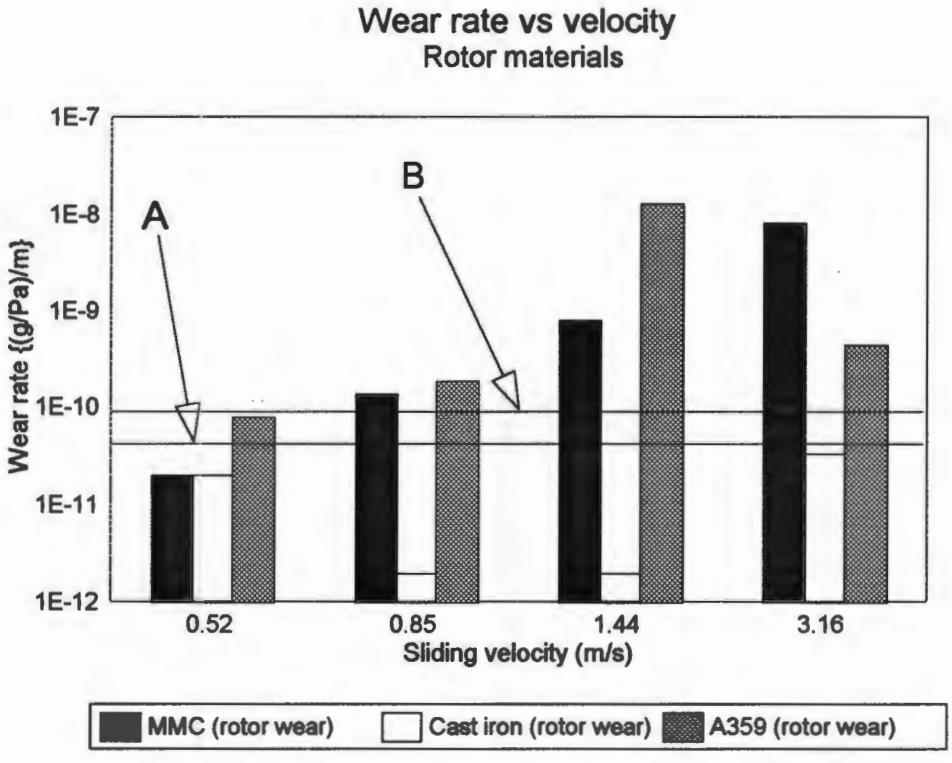

Fig 4.29a: The relationship between rotor material wear rate and sliding velocity for testing phase-2 rotor materials sliding against semi-metallic pad B under 1.034 MPa load. Note that 1E - 12 on the Y - axes indicates a specific wear of $1\times10\text{-}12$ g.Pa^{-1}.m^{-1}. Lines A and B indicate the allowable wear rates of the MMC and cast iron respectively.

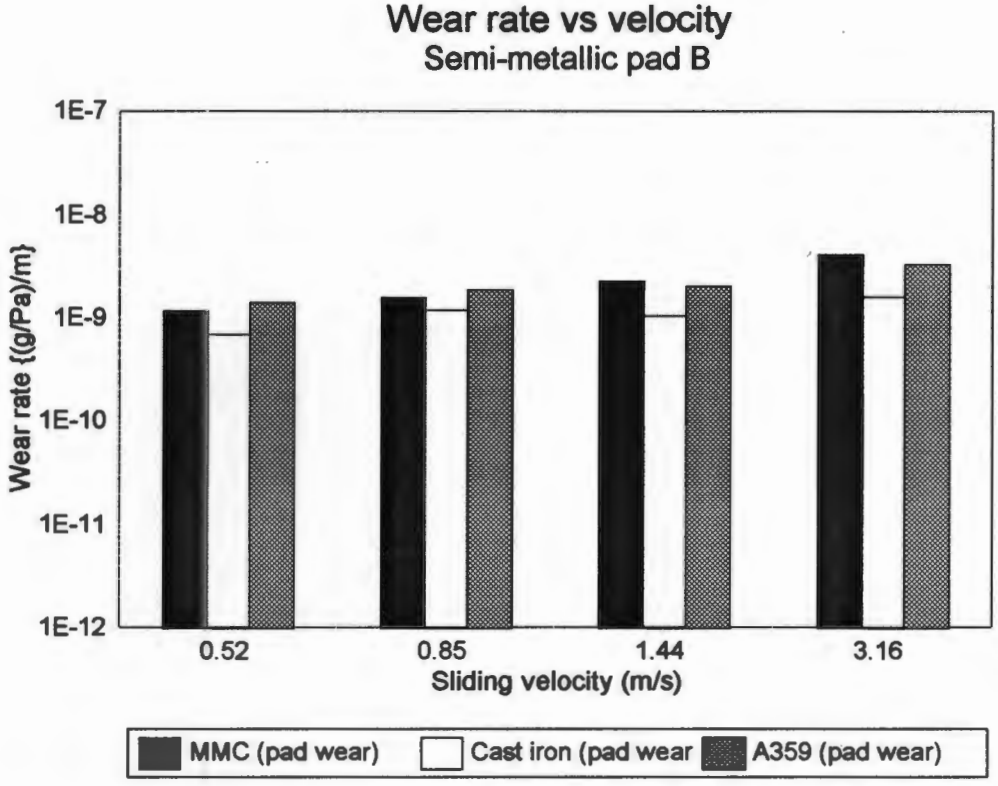

Fig 4.29b: The relationship between pad wear rate and sliding velocity for testing phase-2 rotor materials sliding against semi-metallic pad B under 1.034 MPa load. Note that 1E - 12 on the Y - axes indicates a specific wear of $1 \times 10\text{-}12$ g.Pa^{-1}.m^{-1}.

4.4.2.2 *The influence of sliding velocity on wear interface temperature*

The higher load leads to an increase in the derivative (i.e. an increase in d^2T/dS^2) of the average rate of wear interface temperature increase with sliding distance - fig 4.30. This is true for all testing phase-2 rotor materials sliding against semi-metallic pad B.

Figure 4.30...

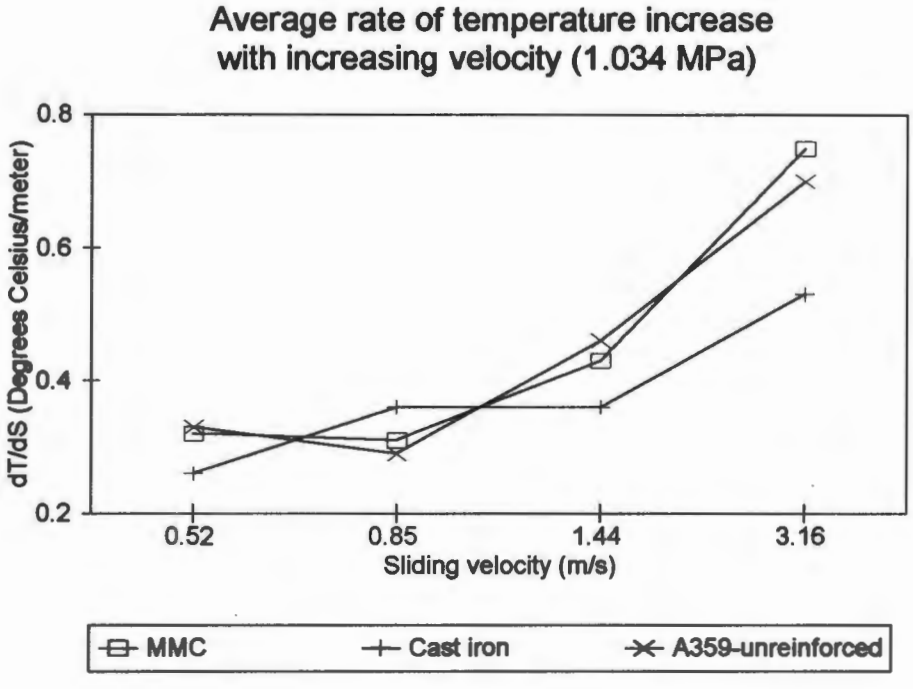

Fig 4.30: Graph showing effect of sliding velocity on the average rate of rotor material temperature increase with sliding distance at 1.034 MPa load.

4.4.2.3 *Wear modes*

The rate and scale of damage in the A359 MMC are greatly increased with an increase in load and at the lowest sliding velocity the A359 MMC experiences severe wear through abrasion by fractured SiC and alumina particulates. Figure 4.31 shows fractured SiC/alumina debris at the foot of partially delaminated A359 MMC wear surface material.

Figure 4.31...

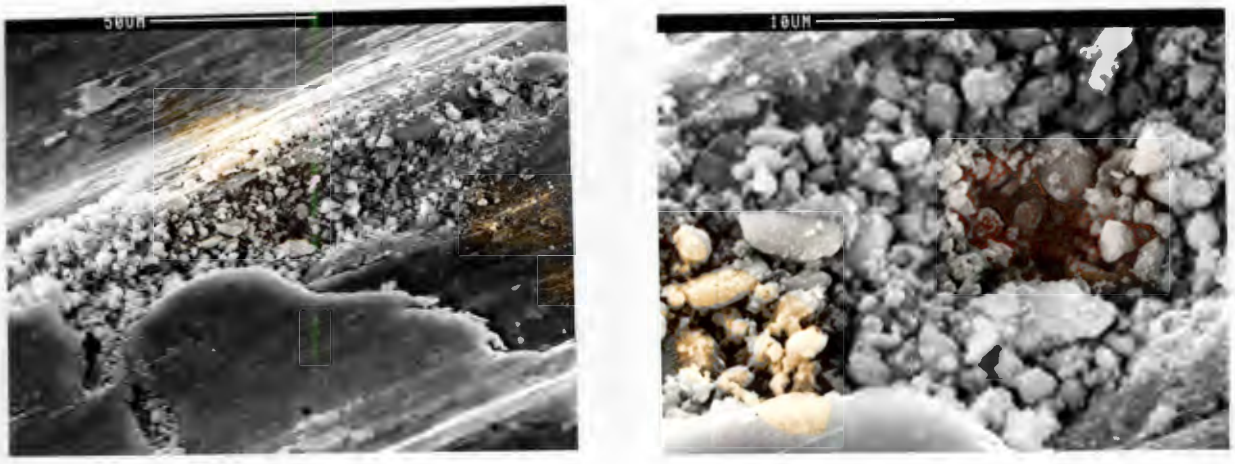

a b

Fig 4.31: Abrasive wear on the A359 MMC wear surface at 1.034 MPa load and 0.52m/s sliding velocity. a). fractured SiC/alumina debris at the foot of partially delaminated surface material. b). magnification of wear debris in (a) showing its sharp, angular and abrasive nature.

At high sliding velocities and high loads, wear in the A359 MMC proceeds through severe subsurface delamination - fig 4.32

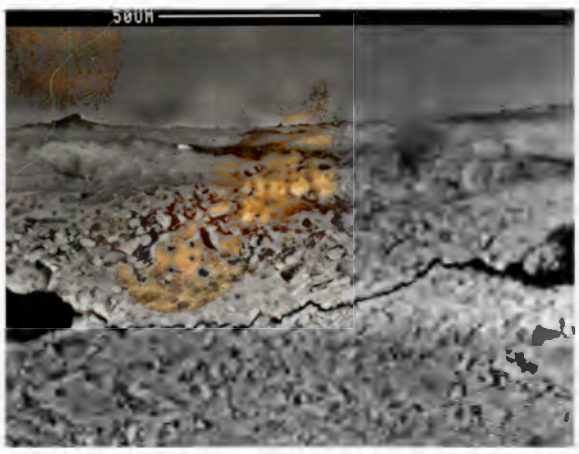

Fig 4.32: Severe subsurface delamination in the A359 MMC after sliding against semi-metallic pad B at 1.034 MPa load and 1.44m/s.

In contrast to the interaction of copper particles from the pad with the unreinforced A359 at lower loads (fig 4.27), these copper particles are not embedded into the A359 MMC wear surface. Instead, they are flattened above the surface of the MMC where they can act as abrasive particles or contribute to the removal of alumina particles from semi-metallic pad B - fig 4.33.

Fig 4.33: Flattened copper from semi-metallic pad B on surface of A359 MMC at 1.034 MPa and 0.52m/s.

At high loads and sliding velocities, melting of the A359 MMC wear surface occurs and SiC particulates are excluded from the melt - fig 4.34.

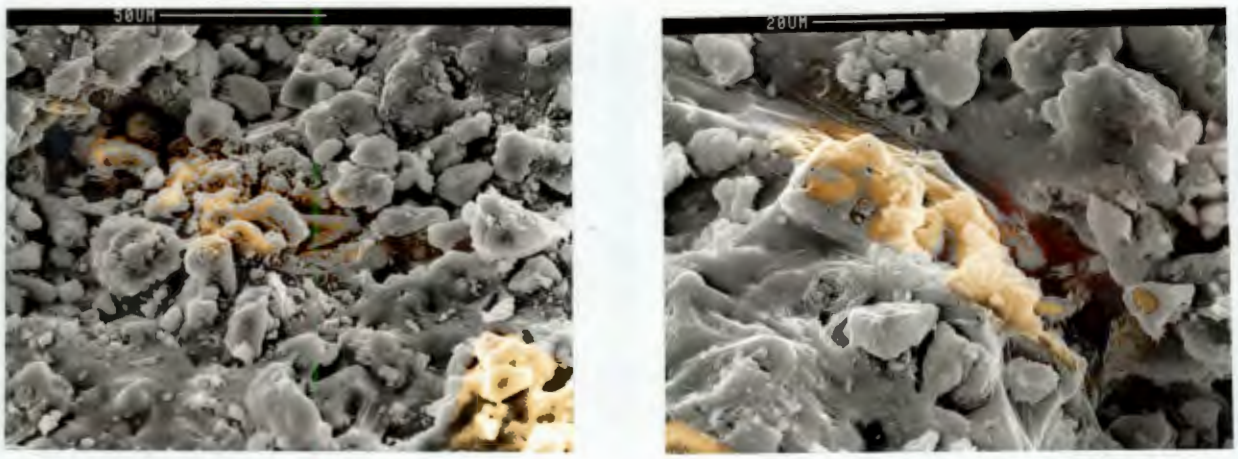

a b

Fig 4.34: Electron micrographs of the A359 MMC wear surface after sliding against semi-metallic pad B under a load of 1.034 MPa and at a sliding velocity of 3.16 m/s. a). Representative view of solidified wear surface showing SiC particulates excluded from the matrix. b). Wear surface under higher magnification showing SiC particulates in the process of being excluded from the matrix before solidification.

The role played by loose alumina particles from the pad in inducing wear on the cast iron surface is illustrated in fig 4.35. When these alumina particles from semi-metallic pad B are driven into the cast iron surface, cracks will radiate outwards on the surface from the areas of highest stress concentration.

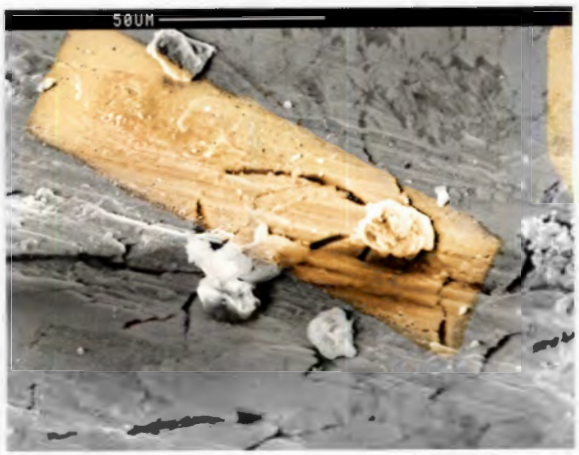

a

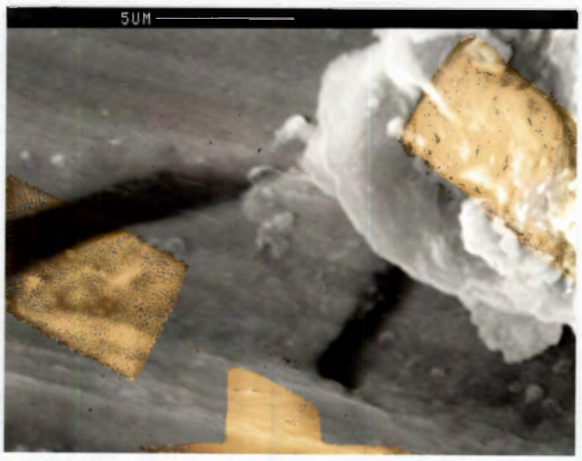

b

Fig 4.35: Wear mode on cast iron surface when worn against semi-metallic pad B under 1.034 MPa load and 0.52m/s sliding velocity. a). alumina particle being driven into the cast iron surface with cracks radiating outwards from the areas of highest stress concentration b). magnification of the wear mechanism in (a).

When these cracks meet on the surface, large sections of cast iron surface material are removed through brittle subsurface cracking - fig 4.36.

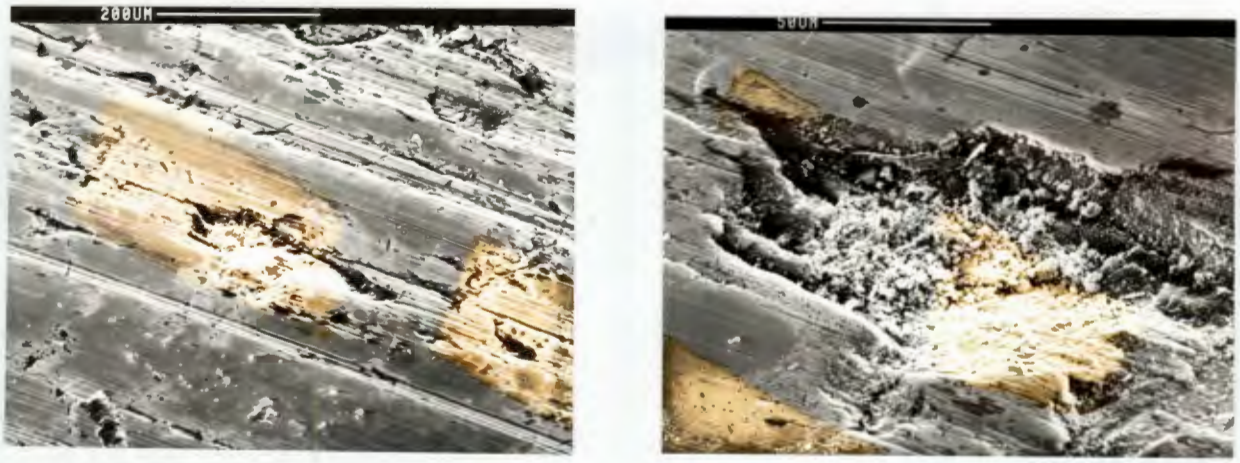

a b

Fig 4.36: Electron micrograph revealing the consequence of the wear mechanism displayed in fig 4.37. a). when surface cracks on the cast iron meet, subsurface brittle cracking results and material is removed in steps from the surface. b). magnification of subsurface cracking in (a).

At the highest sliding velocity, severe surface stresses induce a form of ductile tearing on the cast iron surface - fig 4.37. Also apparent from fig 4.37 is that most of the alumina and other abrasive wear debris particles are concentrated in the wear grooves on the cast iron surface. High lying areas of the wear surface are relatively free of abrasive wear debris.

Fig 4.37: Electron micrograph showing shear bands on the surface of cast iron after sliding against semi-metallic pad B at 1.034 MPa and 3.16m/s.

4.5 *Reproducibility of friction traces*

There are four factors that can influence the reproducibility of friction traces. These are:

1. Reliability of testing apparatus electrical circuitry.
2. Consistency in material properties.
3. Degree of alignment of samples within testing apparatus.
4. Changes in the environment.

The reliability of the testing apparatus was investigated by applying a range of torque to the torque cell and monitoring the degree of voltage scatter in the Status 30 display program. The degree of scatter was found to increase with increasing torque up to a maximum percentage deviation from the mean of 5.7%.

Friction traces demonstrating reproducibility were generated for a sample of material, load and sliding combinations. The smallest percentage deviation from the mean (6%) was measured for the A357 MMC sliding against the organic pad at 1.44m/s (fig 4.38) and the largest percentage deviation from the mean (15%) was measured for the A359 MMC slid against semi-metallic pad B at 1.44m/s sliding velocity and 1.034 MPa load - fig 4.39.

In general, the more stable the friction trace, the greater is its reproducibility. In addition, steady state regimes of friction traces have a higher reproducibility than those approaching steady state - fig 4.39.

Figure 4.38...

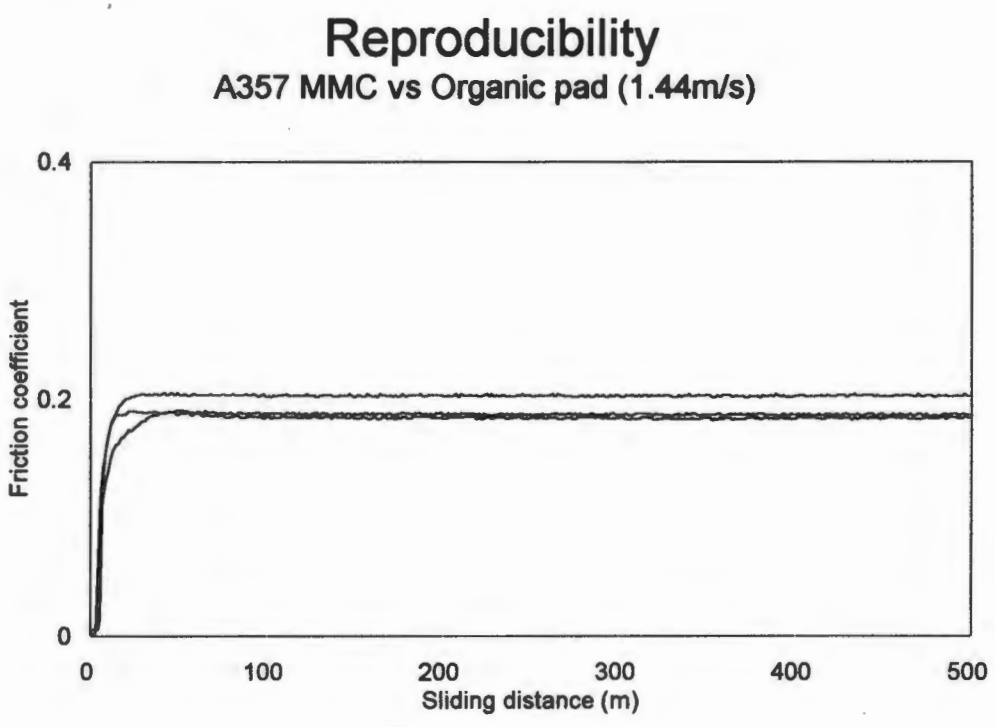

Fig 4.38: Reproducibility friction traces for the A357 MMC sliding against the organic pad at 1.44 m/s.

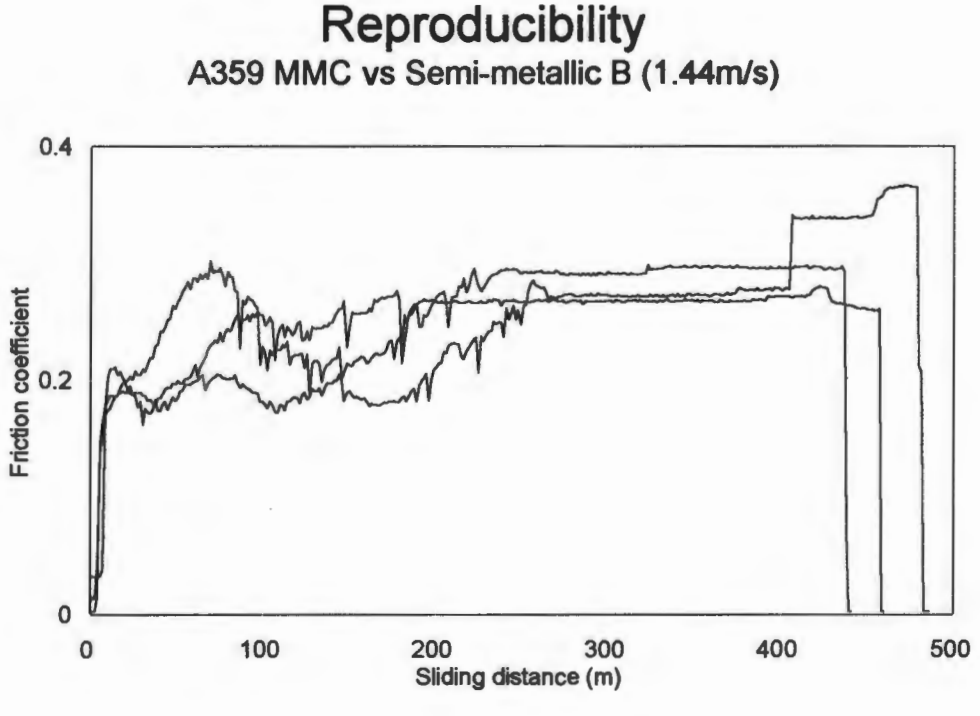

Fig 4.39: Reproducibility friction traces for the A359 MMC sliding against semi-metallic pad B at 1.034 MPa load and 1.44m/s sliding velocity.

Chapter 5

Discussion

5.1 *Interpretation of friction traces*

The interdependence of friction and wear is an important concept that must be understood when friction traces are used in the analysis of wear processes. Is the friction trace an indication of wear processes about to evolve or an indication of wear processes already evolved ?. In other words, does friction determine wear or do wear processes determine friction ?.

Consider two surfaces brought together under a vertical load and relative sliding velocity (fig 3.2). At the onset of sliding there is no wear but there must be a certain value of friction coefficient. With an increase in sliding distance wear will occur through adhesion or abrasion or both and the relationship of interdependence between friction and wear will change. The coefficient of friction will now be dependent on the wear processes occurring at the interface. This relationship of interdependence is shown in the schematic below:

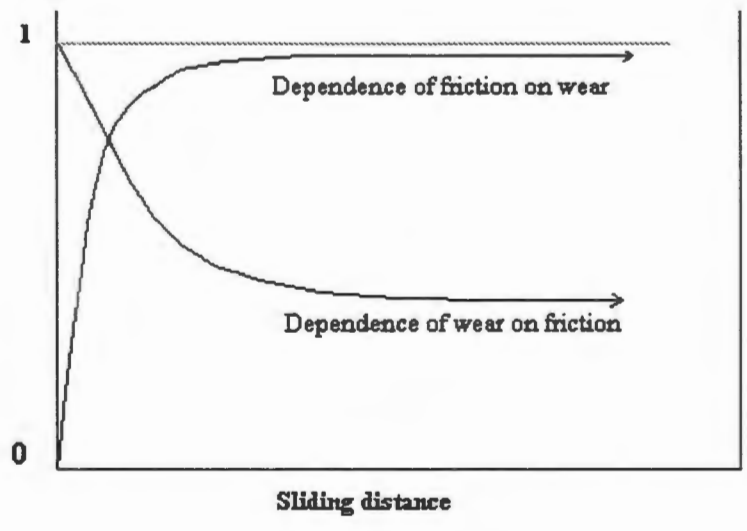

1 - Absolute dependence

0 - Zero dependence

Fig 5.1: Schematic illustrating the relationship of interdependence of friction and wear for sliding surfaces with the geometry shown in fig 3.2.

It can be seen from the schematic above that during early stages of sliding, the friction coefficient will determine the type of wear processes that evolve at the sliding interface. Once these wear mechanisms are established, however, they will determine the value of friction coefficient. Thus, the majority of the friction trace is an indication of the wear processes already evolved and not an indication of the wear processes about to evolve.

In the early stages of sliding where the mechanisms of wear are dependent on the coefficient of friction, cohesive bond strength within the material will be critical in determining the onset of wear. If the value of friction coefficient is a measure of the rate of energy dissipation at the wear interface[94], then if an increase in friction coefficient is not accompanied by an increase in interfacial temperature, this energy must be contributing to the breaking of material bonds. During the early stages of sliding, therefore, a high value of friction coefficient and low interfacial temperatures should indicate a high wear rate for materials with a low cohesive bond strength and a low volumetric specific heat ($C_p \times \rho$).

Another pertinent question in the analysis of friction traces is the following: Does an increase in friction coefficient necessarily signify an increase in wear rate and, similarly, does a decrease in friction coefficient signify a decrease in wear rate ?. This question will be addressed later in this chapter through analysis of the experimental evidence presented in chapter 4.

5.2 *Friction traces (rotor materials vs organic pad)*

The most important observation is that the friction traces for both the A357 MMC and cast iron attain steady state after relatively short sliding distances. These friction traces have a good reproducibility (see section 4.5) and it can be confidently assumed that the requirements for a constant braking torque with sliding distance have been met for both the A357 MMC and cast iron sliding against the organic pad over all sliding velocities.

The effect of silicon carbide reinforcement on the friction coefficient of the unreinforced A357 alloy is clearly discerned from the friction traces in fig 4.11a. At the start of the test, both reinforced and unreinforced A357 have a friction coefficient of approximately 0.33. As the sliding distance increases, however, the friction coefficient of the unreinforced A357 is on the increase while the friction coefficient of the A357 MMC is on the decrease.

The presence of the silicon carbide particles must, therefore, be contributing to the decrease in friction coefficient and a marked decrease in wear. The proposed reason for this divergent behaviour is the following: The mechanism of wear in the unreinforced A357 against the organic pad is similar to the adhesive wear experienced by a perished piece of rubber when rubbed with one's thumb i.e. material is removed in elongated slivers once the strain to fracture of the material is exceeded. These elongated slivers of aluminium contribute to the abrasive component of the coefficient of friction[24] and consequently abrasive wear by plastic deformation (see section 2.3.1) which results in an increase in the overall friction coefficient and wear rate.

In the SiC reinforced A357 MMC, aluminium surface asperities are rapidly worn down through the wear mechanism described for the unreinforced A357 above. This in turn brings more SiC particulates into contact with the friction lining. These SiC particulates become polished, resulting in a lower friction coefficient and decreased wear. On the wear surface of the A357 MMC the SiC particulates are slightly raised above the surface of the matrix, absorbing the load and protecting the matrix from the severe adhesive surface shear strains that would otherwise be experienced in the unreinforced matrix.

There is also some evidence for the formation of a solid lubricant layer on the surface of the A357 MMC - fig's 4.13, 4.14 and 4.15, and the time dependent synthesis of this layer may be a further reason for the difference in frictional behaviour between the A357 MMC and its matrix at the lowest sliding velocity. At the start of the test , no layer exists on the A357 MMC or organic pad wear surface and the friction coefficient will depend on the ploughing/abrasive action of the SiC particulates and adhesive contacts between the matrix material in the MMC and the organic pad surface. With an increase in sliding distance, organic pad debris arising from SiC particulate abrasion will coalesce under pressure and heat to form a layer which will increase in thickness. At sliding distance (S_e) this layer will be an equilibrium thickness (T_e) determined by the sliding velocity. The coefficient of friction is constant from the time the layer reaches equilibrium thickness. Sliding velocity will, therefore, also determine the sliding distance required to reach a constant coefficient of friction- fig 4.10.

The dependence on sliding velocity of the equilibrium thickness of the layer and the sliding distance required to reach this equilibrium thickness may be qualitatively understood from the schematic in fig 5.2.

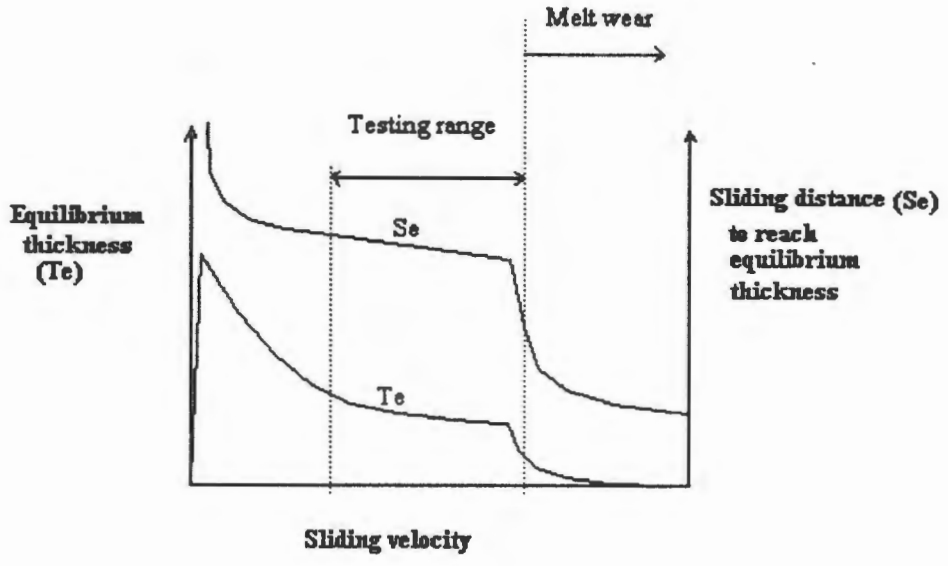

Fig 5.2: Schematic displaying the relationship between the thickness of the solid lubricant layer in addition to the sliding distance required to reach this equilibrium thickness, and sliding velocity.

As sliding velocity increases, the solid lubricant layer becomes thinner and less effective in preventing direct contact between the A357 MMC and organic pad wear surfaces. Thus at a certain sliding velocity, SiC particles in the MMC will be brought into direct contact with the organic pad and abrasive wear of the pad will ensue, resulting in a rapid increase in the friction coefficient. At high sliding velocities and interface temperatures, this wear mechanism is complimented by a 'matrix yielding' wear mechanism mentioned in the literature[71].

When matrix yielding (flow) occurs, SiC particulates experiencing direct load on the MMC wear surface will 'sink' into the matrix thus bringing the matrix into direct contact with the pad surface. Wear will then proceed through a combination of the adhesive slivering mechanism explained above and three body abrasion induced by excluded SiC particulates from the melt.

Differences in geometry between braking systems and testing apparatus may influence the formation and maintenance of this solid lubricant layer on the MMC wear surface. For instance, wear surfaces of specimens in the testing apparatus are in perpetual contact with no opportunity for wear debris dispersal whilst wear surfaces in automobile braking systems are in periodic contact with

opportunity for wear dispersal through brake pad leading edge impingement or contact with the environment. Thus, it may be argued that in automobile braking systems, the solid lubricant layer may not have a chance to form or reach equilibrium thickness (proviso for a constant coefficient of friction). The solid lubricant layer formed on the surface of the A357 MMC after sliding against the organic pad retained its integrity during ultrasonic cleaning in alcohol of post friction tested specimens. This observation suggests that the layer should retain its integrity in automobile braking systems, although the time taken to reach equilibrium thickness (proviso for constant braking torque) may be lengthened. The decrease in friction coefficient and wear rates resulting from the formation of solid lubricant graphitic layers has been reported by Das et al[60] and Rohatgi et al[61]. Figure 5.3 is a schematic illustrating the mechanism of wear and effect of solid lubricant layers on wear for the three testing phase-1 rotor materials sliding against the organic pad.

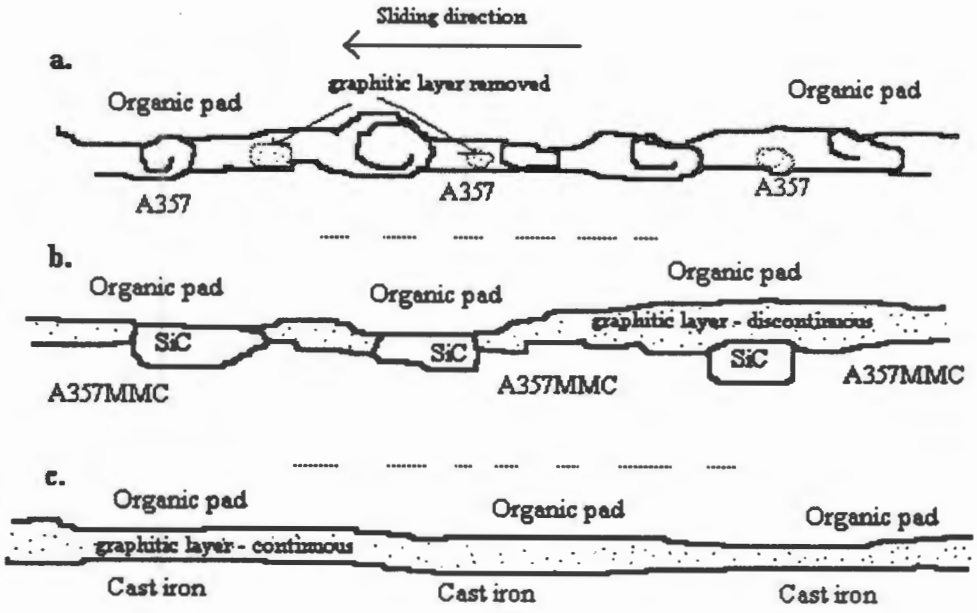

Fig 5.3: Schematic illustrating the mechanism of wear when testing phase-1 materials are worn against the organic pad. a). Due to the large adhesive shear strains, material on the surface of the unreinforced A357 is removed in slivers which impede the formation of a protective graphitic layer. b). SiC particulates in the A357 MMC constrain the A357 matrix thus preventing strain to fracture and the formation of unreinforced slivers which remove the graphitic layer. The SiC particulates also prevent direct adhesive contact between the pad and unreinforced matrix material. c). A thin graphitic layer is maintained at the interface of cast iron sliding against organic pad.

5.2.1 *The influence of sliding velocity on friction and wear*

The fact that the A357 MMC experiences an increase in friction coefficient at the highest sliding velocity and cast iron a decrease (fig 4.11), but both materials experience an increase in wear rate (fig 4.12a) suggests a complex relationship between the coefficient of friction and wear of materials.

An increase in friction coefficient will increase the rate of energy dissipation at the wear interface. This may result in an increase in temperature of the interface materials only or the breaking of bonds (molecular/atomic) only or both. An increase in interface temperature will not necessarily result in increased wear whereas the breaking of bonds certainly would. In the same light, a decrease in friction coefficient will not necessarily indicate decreased material wear at the sliding interface. It follows that mechanical and thermal properties will to a large extent dictate the relationship between friction and corresponding wear rates.

The friction coefficient will more rapidly realise its dependence on wear processes with an increase in sliding velocity (fig 5.1). The decrease in friction coefficient for cast iron and increase in friction coefficient for the A357 MMC, therefore, are a direct result of a change in wear processes at the respective interfaces. At low sliding velocities, cast iron wear surface temperatures are low, but with an increase in sliding velocities surface temperatures increase rapidly. The cast iron thus expands and graphite is released from the graphite flakes on the surface. This released graphite contributes to the solid lubricant layer at the wear interface which dissipates shear with a resulting decrease in friction coefficient and an increase in wear.

Wear of the pearlite and steadite phases within the cast iron is minimal and the wear monitored is almost entirely a result of graphite removal from the flakes on the surface. This was confirmed through energy dispersive X-ray analysis of wear debris. Apart from the mechanism of graphite release, the evolution of gases at the wear interface and the release of the friction material's internal lubricant could be co-responsible for the decrease in friction coefficient.

As mentioned previously, for the A357 MMC, an increase in sliding velocity decreases the thickness and protective effectiveness of the solid lubricant layer - fig's 4.13 & 5.2. Silicon carbide particulates will thus be brought into direct contact with the pad resulting in an increase in friction coefficient and wear.

5.3 *Friction traces (rotor materials vs semi-metallic pad A)*

In fig 4.17, friction traces for the 357 MMC are characterised by sharp non linear increases in friction coefficient with sliding distance. This is due to increasing concentrations of fractured SiC particulate debris from the MMC surface and loose metal chips from the pad surface arising at the wear interface through two body abrasion. These hard debris particles perpetuate wear through three body abrasion with the pad and MMC wear surfaces.

Ultimately subsurface delamination occurs in the MMC accelerated by the formation of adhesion welds at the wear interface. These adhesion welds are similar to those observed by A. Somi Reddy et al[45]. Subsurface delamination is accompanied by a large instantaneous increase in friction coefficient and consequent melt wear.

Cast iron displays a very stable friction coefficient at low sliding velocities (fig 4.17a&b). It is interesting to note, however, that the friction coefficient of cast iron sliding against semi-metallic pad A is characterised by fade at high sliding velocities (fig 4.17c) while fade of the cast iron friction coefficient against the organic pad at high sliding velocities, is absent - fig 4.10c.

5.3.1 *The influence of sliding velocity on wear*

Subsurface delamination in the MMC occurs at shorter sliding distances with an increase in sliding velocity and usually with melt wear in the MMC, a layer of molten MMC will be trapped between the surface of unmolten MMC and the semi-metallic brake pad surface as in the last 100m of the MMC friction trace in fig 4.17b.

Under these conditions, pad wear is minimised and a stable and relatively low coefficient of friction is obtained, although this would not be desirable in automobile braking systems since the interface would seize or lock on cooling. During melt wear, large scale material transfer of MMC material occurs onto semi-metallic pad A - fig 4.18b.

Figure 5.4 illustrates the three stages of wear for the A357 MMC sliding against semi-metallic pad A:

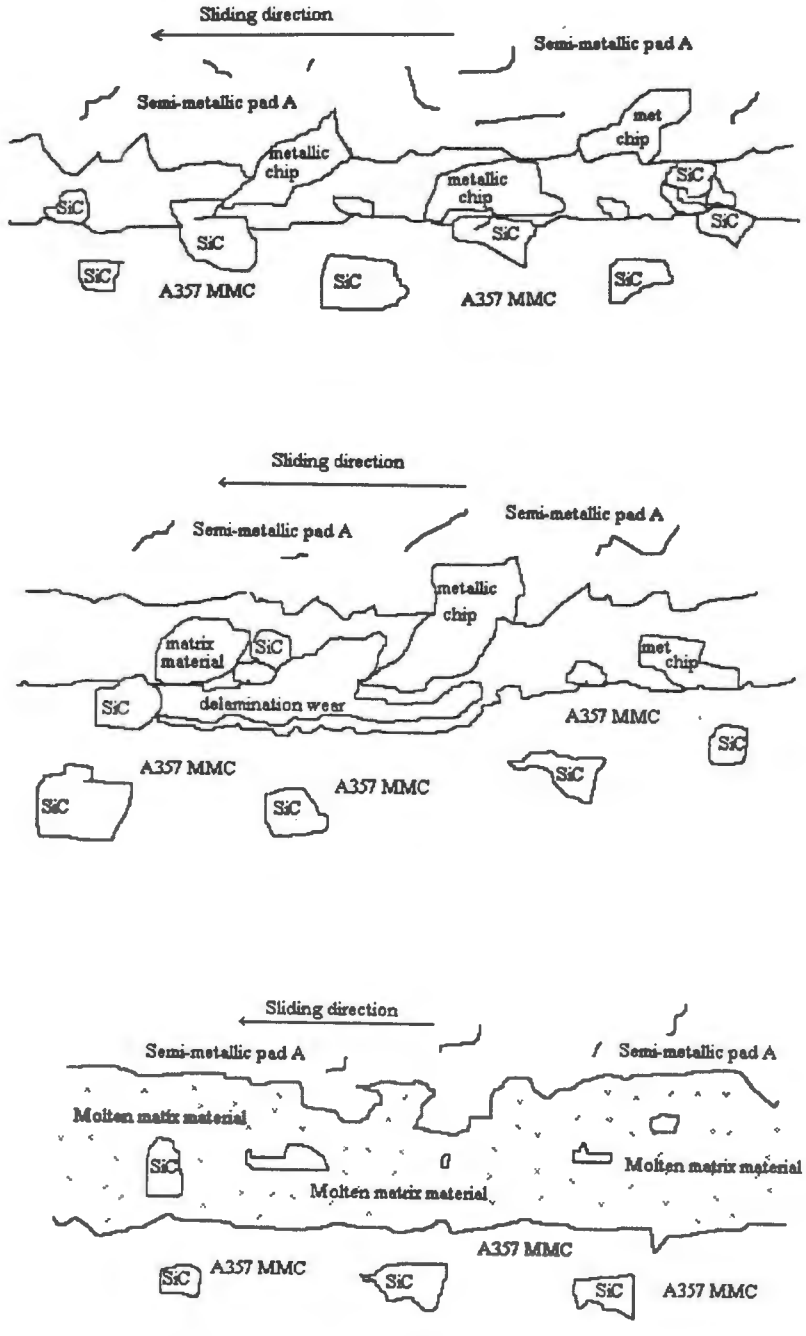

Fig 5.4: Schematic illustrating the three stage wear mechanism for the A359 MMC during dry sliding against semi-metallic pad A. Stage 1 - rapid build up of abrasive fractured SiC particle and metallic chip debris at wear interface with high wear rates due to abrasion. Stage 2 - severe damage through subsurface delamination accompanied by an instantaneous increase in friction coefficient and extremely high wear rates. Stage 3 - layer of molten aluminium forms at wear surface with constant coefficient of friction and minimal wear rates.

The wear of cast irons against semi-metallic pad A at low sliding velocities is also a three stage process. During early stages of sliding the cast iron wear surface is at a relatively low temperature. During this stage of sliding the friction coefficient is constant and reflects a combination of the levelling of asperities on the cast iron wear surface and abrasion of this surface by loose metallic particles from the pad.

At a certain sliding distance, however, the cast iron surface will have reached a critical temperature characterised by the rapid formation of an iron oxide layer at the wear interface and at the perimeter of the cylinder which leads to an increase in friction coefficient.

This oxide formation was macroscopically observed in situ during testing. The rate of formation of this oxide layer is determined by equation 2.8 (section 2.3.3). Wear interface temperature will increase with an increase in sliding velocity. Equation 2.8 predicts an increase in oxidation rate with an increase in temperature. This prediction is confirmed by the cast iron friction traces in fig's 4.17a&b where the oxidation regime is steeper in fig 4.17a than in fig 4.17b.

As the volume of the oxide layer increases so will the number of adhesive and cohesive bonds within the layer that need to be broken increase. This will lead to an increase in the rate of energy dissipation at the wear interface which will be reflected by an increase in friction coefficient.

The final stage is characterised by a levelling off of the friction coefficient once an equilibrium is reached between the formation of this oxide layer and its incorporation into the wear layer at the interface. Although this third stage is characterised by a higher friction coefficient due to strong adhesion and cohesion of the oxide layer, it does not have a significant effect on the wear rate.

This statement is confirmed by the fact that cast iron has the same wear rate (fig 4.18a) for both the 0.52m/s and 1.44m/s sliding velocities even though stage 3 is reached sooner at 1.44m/s than at 0.52m/s - fig 4.17. This phenomenon provides evidence that a higher coefficient of friction does not necessarily indicate an increase in wear rate. Similar observations have been made by A. Verma et al[92]. At high sliding velocities stages 1 and 2 are absent and although oxide formation is observed, its effect on friction and wear is minimal compared with the mechanism of graphite release from the graphite

flakes on the cast iron wear surface (described in section 5.2.1). This mechanism can be considered a fourth stage in the wear of cast iron against semi-metallic pad A, only occurring at high sliding velocities. During this stage, wear of steadite and pearlite in the cast iron occur due to the impingement of metallic chips into the cracks vacated by the graphite and "crazy paving" cracks induced by thermal fatigue. This stage is characterised by a relatively high wear rate for cast iron (fig 4.18a) and a high degree of fade - fig 4.17c. Figure 5.5 is a schematic of the fourth stage of wear for cast iron sliding against semi-metallic pad A.

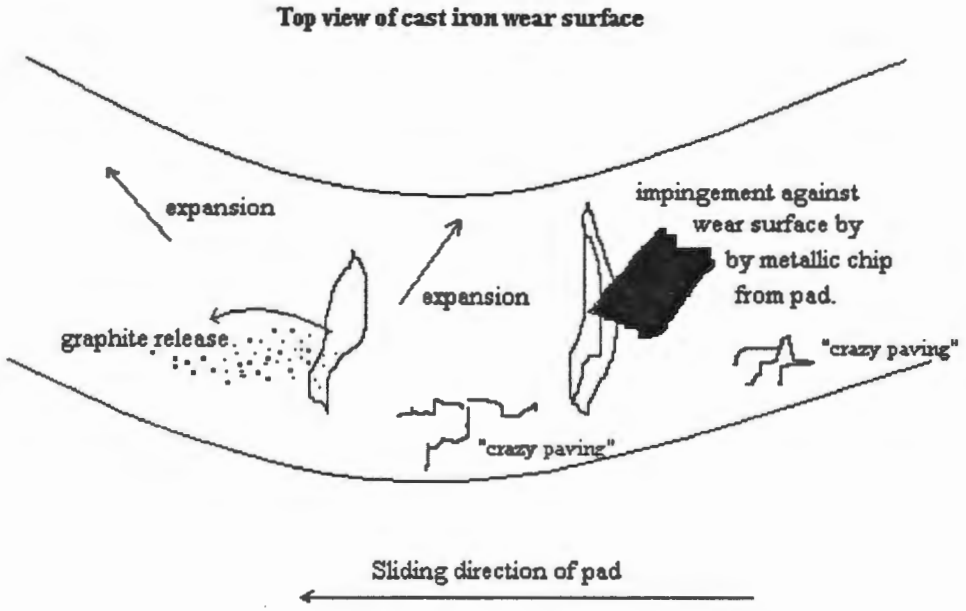

Fig 5.5: Schematic illustrating the fourth stage of sliding wear for cast iron against semi-metallic pad A. This stage is characterised by a low coefficient of friction but high specific wear.

Wear of the unreinforced A357 Alloy against semi-metallic pad A is characterised by the formation of a thick, powdery graphitic layer containing large volumes of fine aluminium and silicon phase wear debris. Cohesion and adhesion in this graphitic layer is extremely weak and the constant coefficient of friction (fig 4.17a) is as a result of an equilibrium between the rapid removal of this layer and its rejuvenation through heavy wear of the A357 alloy and semi-metallic pad A - fig 4.18.

Due to the poor cohesion and adhesion of graphitic layers formed on the unreinforced A357 and A357 MMC wear surfaces when worn against semi-metallic pad A, these layers do not contribute to their wear resistance.

5.4 *Friction traces (rotor materials vs semi-metallic pad B @ 517KPa)*

Fiction traces for the A359 MMC and the unreinforced A359 alloy are irregular and it is difficult to identify any relationship between friction coefficient and sliding distance or sliding velocity for these materials. The irregularity of these friction traces points towards the instability of contacting materials at the wear interface in which the alumina particles from the pad and the fractured SiC particulates from the MMC play a major role - fig 4.20.

The fractured SiC particulates and the abrasive alumina particles disturb the formation of a protective layer on the MMC wear surface and although a thin discontinuous layer was observed on the A359 MMC surface at the lowest load and sliding velocity, no solid lubricant wear surface layers were detected for any of the materials at any higher load and sliding velocity combinations.

The friction traces of cast iron worn against semi-metallic pad B at low loads show similarities to those of cast iron when worn against semi-metallic pad A. Certainly, oxidation of the cast iron was observed in situ during sliding against semi-metallic pad B and the onset of oxidation corresponded closely with the marked increases in friction coefficient at the two lowest sliding velocities - fig 4.19a&b. At the highest sliding velocity cast iron displays excessive fade in friction coefficient - fig 4.19d. The degree of fade is higher for cast iron sliding against semi-metallic pad B than it is for the same material sliding against semi-metallic pad A (compare friction trace 2 in fig's 4.17c and 4.19d).

Friction traces generated by sliding the unreinforced A359 alloy against semi-metallic pad B at low loads show little consistency except at the two highest sliding velocities where the friction coefficient attains a constant level after approximately 200m of sliding - fig 4.19. A thick, powdery layer similar to that generated during the sliding unreinforced A357 against semi-metallic pad A was detected at the interface at these sliding velocities.

5.4.1 *The influence of sliding velocity on wear*

All rotor materials first show a decrease in wear rate and then an increase at the highest sliding velocity - fig 4.21a. The anomaly for the wear rate of the A359 MMC at 1.44m/s (fig 4.21a) could be the result of misalignment.

In their study of the abrasion resistance of MMCs, S. Wilson et al[1] found that the hardness of abrasive particles against which the composite is loaded plays an important role in the MMC's wear behaviour. On abrading SiC reinforced MMCs with alumina grit they found that the alumina abrasive particles and the SiC reinforcing particulates were involved in a process of mutual microfracture as they moved across each other. This is precisely the dominant wear mechanism for the A359 MMC sliding against semi-metallic pad B at low loads and sliding velocities. Distribution of SiC particulates in the composite may also have an effect on this mutual microfracture of particles explained above. In their work on damage initiation in aluminium metal matrix composites, Y. Brechet et al[93] found that both the size and distribution of SiC particulates influence the fracture behaviour in the composite.

Upon inspection of the A359 MMC wear surface for the lowest load and sliding velocity the majority of SiC particulates were unfractured. This suggests that the critical load for SiC particulate fracture has not been exceeded (see section 2.6.3) and that the SiC debris arises primarily due to the mutual microfracture of alumina particles from the pad and SiC particulates on the MMC wear surface. Alpas and Zhang's hypothesis[82] (section 2.6.3) indicates that once a critical load is exceeded, all SiC particulates experiencing this load will fracture. At loads significantly lower than the critical load, however, alumina particles in semi-metallic pad B will either be dislodged from the pad or will induce fracture of SiC particulates in their path. Both possibilities will lead to an increase in surface roughness and further possibility of SiC particulate fracture.

There is little difference in the evolution of microhardness towards the wear surface between the matrix material in the A359 MMC and the A359 alloy at low loads - fig 4.23 This is in contrast to observations in the literature[1] where an increase in SiC reinforcement was found to increase matrix microhardness and decrease the strain to fracture with a resultant increase in wear rate.

The wear mode for cast iron sliding against semi-metallic pad B is identical to that for cast iron sliding against semi-metallic pad A with the metallic chip wear inducing particles in semi-metallic pad A replaced by the hard alumina particles in semi-metallic pad B. This assumption is supported by the cast iron friction trace in fig 4.19d where the jagged peaks could reflect alumina particle build up and impingement in the cracks vacated by the graphite on the cast iron wear surface. Figure 2.3, section 2.3.2 can be used to explain the brittle nature of cracking of the cast iron wear surface in fig 4.25. Most importantly, however,

the wide vacant hole at the top of the micrograph (fig 4.25) corresponds closely in size and shape to the graphite flake in the centre of the optical micrograph in fig 4.5a. Since graphite is electrically conductive, the use of secondary electrons during electron microscopy would not induce such a sharp contrast in the micrograph (fig 4.25) were the hole filled with graphite. The hole must therefore be vacant which lends credence to the author's hypothesis for increased wear with decreased friction coefficient and decreased friction coefficient with increased temperature (cast iron wear surface expansion). Of course, the evolution of gases at the wear interface may also contribute to the decrease in friction coefficient[7].

In contrast to the adhesive slivering wear mechanism described for the unreinforced A357 alloy sliding against the organic pad in section 5.2, wear for the unreinforced A359 alloy against semi-metallic pad B occurs primarily through the tearing/scouring of material and extrusion at the sides of the wear scar - fig 4.26 (also observed by D. A. Rigney et al[44]). Loosened copper strips from the pad may also contribute to the wear resistance of the unreinforced A359 alloy when they are embedded into the wear surface - fig 4.27. They may, however, contribute to pad wear through abrasion.

There is no evidence of surface melting of the A359 MMC or the unreinforced A359 alloy at low loads. This is due to the low rate of wear interface temperature increase at low loads - fig 4.22. It is interesting to note that even though the A359 MMC and the unreinforced A359 alloy possess higher thermal conductivities and diffusivities than cast iron (table 1.1), they have similar rates of wear interface temperature increase - fig 4.22. This may be a result of the small volume of material contained in the friction test samples (between 8 and 12 cubic centimetres). If the sample size had been larger e.g. the dimensions of a brake rotor, the rate of wear interface temperature increase may have been lower for the aluminium based materials than for the cast iron.

5.5 *Friction traces (rotor materials vs semi-metallic pad B @ 1.034MPa)*

Instability of the A359 MMC and unreinforced A359 alloy at the wear interface at the higher load is more pronounced and this is reflected in friction traces 1 and 3 of fig 4.28. It is clear from friction traces 1 and 3 in fig 4.28 that the friction coefficient of the A359 MMC tends towards that of the unreinforced

A359 alloy as sliding distance increases, suggesting that little friction stabilising benefit is obtained from the reinforcing silicon carbide particulates at the high load. Cast iron shows stable frictional properties for the two lowest sliding velocities and friction trace 2 in fig 4.28a is a very good example of a typical cast iron friction trace for semi-metallic pads where the three stages in the friction trace (described in section 5.3.1) are shown. At the two highest sliding velocities excessive fade of the cast iron friction coefficient is evident - friction trace 2, fig 4.28c&d. This fade could be the result of the polishing of alumina particles on the pad surface.

5.5.1 *The influence of sliding velocity on wear*

The rate and scale of damage for the A359 MMC and the unreinforced A359 alloy are greatly increased with an increase in load. This is reflected in fig 4.29a over all sliding velocities (compare with fig 4.21a). The decrease in wear rate for the unreinforced A359 alloy at the highest sliding velocity is due to the formation of a thick powdery wear debris layer similar to that described for the A357 MMC sliding against semi-metallic pad A (section 5.3.1). The wear rate for cast iron first decreases with increased velocity and then increases - fig 4.29a. This relationship is thus an inversion of that displayed for cast iron sliding against steel in fig 2.8c.

At high loads and low sliding velocities, two and three body abrasion mechanisms are the dominant wear processes in the A359 MMC - fig 4.31. At higher sliding velocities , subsurface delamination occurs at a very early stage in the A359 MMC and melt wear occurs after approximately 150m of sliding - fig 4.28d and fig 4.32. In addition, cohesiveness of materials within the pad is extremely poor at high sliding velocities and loads and large sections of brittle pad material are removed from the pad surface where they accelerate subsurface delamination in the A359 MMC.

At all sliding velocities, no evidence of interfacial SiC particulate/aluminium matrix debonding was found and all failure mechanisms detected within the A359 MMC initiated from within the matrix material. At high sliding velocities where surface melting occurs in the A359 MMC, interfacial debonding may occur due to the embrittling effects of $MgAl_2O_4$ spinel formation[67-71] at the bonding interface. Certainly, as displayed in fig 4.34, SiC particulates were

found to be excluded, and in the process of being excluded from the matrix after sliding at the highest velocity against semi-metallic pad B. This phenomenon has been attributed to melt-out rather than to embrittling effects at the bonding interface.

In the investigations of Martinez et al[73], the transition from mild abrasive wear to severe subsurface delamination wear was found to occur at temperatures in excess of 150°C. The temperature recorded for the A359 MMC surface after sliding against semi-metallic pad B at 1.034 MPa and 3.16m/s was 195.33°C. It must be stressed, however, that this temperature is that of the bulk surface material. Flash point temperatures of contacting surface asperities can be up to five times higher[70]. It is thus reasonable to conclude that the mechanism of wear for the A359 MMC for this load and sliding velocity is likely to be a combination of severe subsurface delamination and abrasion by SiC particulates which are excluded from the molten contacting surface asperities.

At the lowest sliding velocity at the high load of 1.034 MPa, the frictional force and wear behaviour of cast iron follows the same pattern described in section 5.3.1. The increase in load, however, leads to a decrease in friction coefficient for cast iron at all sliding velocities - fig 4.19 & 4.28. This phenomenon was also observed during the experiments of Y. Zhang et al[91]. Wear rate for cast iron sliding against semi-metallic pad B also decreases with increased load - fig 4.21a & 4.29a.

It is possible that the higher load is more effective in driving loose alumina particles into the cast iron wear surface at high sliding velocities. These alumina particles may then become polished and flush with the surface resulting in decreased friction coefficients and wear rates. This assumption is supported by the studies on abrasion conducted by A. Misra et al[95] where it was found that SiC abrasive particles would be embedded into tool steel during three body abrasion tests and that these SiC particles then contribute to the tool steel's sliding wear and abrasion resistance.

Wear mechanisms for cast iron at low sliding velocities are characterised by surface cracking where alumina particles from the pad are driven into the cast iron surface - fig 4.35. These cracks radiate outwards on the surface from the areas of highest stress concentration and when they meet on the surface, material is removed through subsurface brittle cracking - fig 4.36.

Wear at high sliding velocities is characterised by ductile shear band tearing - fig 4.37. Abrasive wear debris concentrates in wear fissures on the cast iron wear surface whilst high lying areas in contact with the pad are relatively free of wear debris. Thus, it may be that as the concentration of these shear bands increase, so the concentration of abrasive wear debris on the surface of cast iron in actual contact with the pad will decrease. This mechanism combined with the graphite release mechanism and the evolution of gases described in earlier sections may be responsible for decreased friction coefficient levels and wear rate with increasing load.

With regard to temperature effects, it is useful to consider the units of the product of load and velocity i.e. the PV factor. With the Newton per square metre the unit for load (pressure) and metres per second the unit for sliding velocity, the unit for the PV factor will be Joules per second i.e. the energy fed into the wear interface per unit second. Thus, an increase in either sliding velocity or applied load should theoretically result in an increase in temperature at the wear interface unless all the energy is used to break material bonds.

The higher load, therefore, in the above discussion should induce greater levels of expansion on the cast iron wear surface. This expansion leads to an increased rate of graphite release and consequently a drop in friction coefficient. The above argument is supported by the information revealed in fig's 4.22 and 4.30 where the effect of sliding velocity on the average rate of temperature increase (°C per meter of sliding distance) of testing phase-2 rotor materials is investigated. An increase in sliding velocity will increase the rate of temperature increase at the sliding interface. An increase in load will shift the graphs in fig 4.22 upwards and change their shape closer to that of a hyperbolic function - fig 4.30.

This means that an increase in sliding velocity will increase the influence of wear mechanisms dependent on elevated temperatures. An increase in load will greatly accelerate the rate at which these levels of influence will be attained at each sliding velocity. Both an increase in load and sliding velocity will lead to a decrease in friction and wear for cast iron sliding against semi-metallic pad B.

Wear modes for the unreinforced A359 alloy at high loads do not differ from those at low loads. These wear modes are, however, more pronounced at high loads. The unreinforced A359 alloy experiences severe melt wear at the highest sliding velocity.

CHAPTER 6

CONCLUSIONS

Dry sliding wear mechanisms of particulate reinforced MMCs, the unreinforced matrices of the aluminium MMCs and cast iron against automobile friction materials have been investigated. Friction traces, optical microscopy and electron microscopy have been used to develop models of these wear modes.

6.1 *Wear modes for MMCs sliding against automobile friction linings*

The wear modes for aluminium MMCs are two body abrasion, three body abrasion, subsurface delamination and exclusion of SiC particulates from molten wear surface material. Of these wear mechanisms, subsurface delamination is responsible for the highest wear rates. Sliding velocity, applied load, counterface surface roughness, cohesion of materials within the counterface, hardness of load bearing particulates in the counterface and the formation of solid lubricant layers at the wear interface will all determine the dominant wear mode for the specific MMC - friction material combination. In general, an increase in either sliding velocity or applied load, will lead to an increase in wear rate.

6.2 *Wear modes for unreinforced aluminium alloys against automobile friction linings*

Wear in unreinforced aluminium alloys occurs through extrusion at the exit side of the wear scar, adhesive slivering, scouring/tearing and surface melting. Wear rates of unreinforced aluminium against automobile friction materials are extremely high in comparison with those for cast iron.

6.3 *The influence of SiC particulate reinforcement on the wear resistance of aluminium MMCs against automobile friction linings*

Whether SiC particulate reinforcement of aluminium alloys improve these alloys' wear resistance will depend entirely on the material properties of the friction lining counterface. If the friction lining has strong cohesive bonding, a low surface roughness and does not contain particles of similar hardness to the

reinforcing particulates then the wear resistance of aluminium MMCs can be up to 300 times as high as that of their unreinforced matrices. If, on the other hand, cohesive bonding in the friction lining is weak, its surface topography rough and it contains particles of similar hardness to the reinforcing particulates in the MMC, then the wear rate of aluminium MMCs can be inferior to that of their unreinforced matrices.

6.4 *Wear modes for cast iron sliding against automobile friction linings*

Wear modes for cast iron include two body abrasion, graphite release from graphite flakes on the wear surface, thermal fatigue, subsurface brittle cracking and ductile shear band tearing. The dominant wear mode for a specific cast iron - friction material combination will be determined primarily by the applied load and sliding velocity. Increases in load and sliding velocity lead to a decrease in friction coefficient, but this decrease in friction coefficient need not necessarily indicate a decrease in wear rate nor does an increase in friction coefficient necessarily indicate an increase in wear rate. The relationship between friction coefficient and wear rate for cast iron sliding against automobile friction materials will be determined by the type of wear mode/s at the sliding interface.

6.5 *Friction and wear performance comparisons between aluminium MMCs and cast iron*

If the structure and composition of friction linings are arranged correctly, the wear resistance and frictional performance of aluminium MMC brake rotors are superior to those of cast iron brake rotors. In addition, the lower density of aluminium MMCs provides for an economic advantage over cast iron with respect to efficient use of fuel, and fabrication expenses.

REFERENCES

1 S. Wilson and A. Ball in *Tribology of Composite Materials*, P.K. Rohatgi, P. J Blau and C. S. Yust (eds), ASM, Materials Park, 1990, pp. 103-112.T.

2 P. Rohatgi, *Advanced Materials and Processes*, February 1990, pp. 39-44.

3 A. Vasudavan, R. D. Doherty (eds), *Treatise on Materials Science and Technology*, Vol 31, Academic Press, San Diego, 1989.

4 M. Hunt, *Materials Engineering*, January 1989, pp. 37-40.

5 A. Watanabe, Y. Sugai, T. Tsiyimura, K. Takao, E. Nishii, T. Khikawa, *Japan Institute of Light Metals,* Proc. Conf. Raselm, 1991, pp. 525-530.

6 S.K. Rhee, *Society of Automotive Engineers Transactions*, 1974, paper 740415.

7 S.K. Rhee and J.E. Byers, *Society of Automotive Engineers Transactions*, 1972, paper 720930.

8 J. M. Herring, *Society of Automotive Engineers Transactions*, 1967, paper 670146.

9 N. Mohan, *Society of Automotive Engineers Transactions*, 1980, paper 800782.

10 R. Limpert, PhD Thesis, University of Michigan, 1972

11 R.M. Rusnak, H.W. Schwartz and W.P. Coleman, *Society of Automotive Engineers Transactions*, 1970, paper 700137.

12 J. Sadanandam, G Bikshamaiah, B. Gopalakrishna, Y. R. Mahajan, *Journal of Materials Science Letters*, Vol 11, 1992, pp. 1518-1520.

13 A. L. Geiger, D. P. H. Haselman and K. Y. Donaldson, *Journal of Materials Science Letters*, Vol 12, 1993, pp. 420-423.

14 Duralcan Aluminium Composites Commercialisation Update, December 1992.

15 M. Jennings, *Industrial Diamond Review*, Vol 53, No 554, Jan 1993, pp. 1-3.

16 P. H. S. Tsang, M. G. Jacko and S. K. Rhee, *Comparison of Chase and Inertial Dynomometer Testing*, in K. C. Ludema (ed), Proc. Int. Conf. on

17 W. R. Hoover and M. G. Jacko, Proc. Conf. *Light Materials for Transportation Sytems*, N. J. Kim (ed), Kyongju, Korea, June 1993.

18 E. Rabinowicz, Proc. Int. Conf. on Wear of Materials, St Louis, MO, *American Society for Mechanical Engineers*, New York, 1977, pp. 36-40.

19 N. P. Suh, *Wear* , 25 (1973), pp. 111-124.

20 F. P. Bowden and D. Tabor, *Friction and lubrication of solids*, Clarendon Press, Oxford, Part 1, 1950, pp. 90-121, part 2, 1964, pp. 52-86.

21 H. Ernst and M. E. Merchant, *Proc. Special Summer Conf. on Friction and Surface Finish*, 1940, Massachussetts Institute of Technology Press, Cambridge, MA, 1969, pp. 76-101.

22 M. C. Shaw and E. F. Macks, *Analysis and lubrication of bearings*, McGraw Hill, New York, 1949, pp. 457-461.

23 E Rabinowicz, *Friction and Wear of Materials*, Wiley, New York, 1965, pp. 51-108.

24 N. P. Suh and H. C. Sin, *Wear*, 69, 1981, pp. 91-114.

25 P. E. Fowles, *J. Lub. Technol*, 97, 1975, pp. 311-315.

26 A. Majumder and B. Bhushan, *J. Tribol.*, 113, 1991, pp. 1-4.

27 H. M. Stanley, I. Etsion and D. B. Bogey, J. Tribol., 112, 1990, pp. 98-102.

28 T. N. Ying and S. M. Hsu, *Wear*, 169, 1993, pp. 33-41.

29 M. Sawa and D. A. Rigney, Wear, 119, 1987, pp. 369-390.

30 D. A. Rigney, L. H. Chen and M. Sawa in *Metal transfer and Galling in Metallic Systems*, H. Merchant and K. Bhansali (eds), TMS-AIME, 1987,pp. 87-102.

31 T. Kjer, *Proc. Int. Conf. on Wear of Materials*, ASME, New York,1987, pp. 191-198.

32 K. C. Ludema, *Wear*, 100, 1984, pp. 315-331.

33 A. W. Batchelor, G. W. Stachowiak and A. Cameron, *Wear*, 113, 1986, pp. 203-223.

34 D. A. Rigney and J. Schell, *Wear*, 75, 1982, pp. 205-220.

35 I. M. Hutchings, *Tribology - Friction and Wear of Engineering Materials*, St Edmundsbury Press Ltd, Bury, St Edmunds, Suffolk, 1992, pp. 103-171.

36 J. F. Archard, *Wear*, 2, 1958/9, pp. 438-455.

37 A. D. Sakar, *Wear*, 31, 1975, pp. 331-335.

38 J. Clarke and A. D. Sakar, *Wear*, 54, 1979, pp. 7-11.

39 K. Okabayashi and M. Kawamoto, *Bull. Univ. Osaka Prefect.*, A17, 1968, pp. 199-202.

40 G. Meyer-Rodenbeck, T. Hurd and A. Ball, *Wear*, 154, 1992, pp. 305-317

41 J. B. Andrews and M. V. Sereveratne, *AFS Trans.*, 92, 1984, pp. 209-212.

42 N. Han, G. Pollard, and R. Stevens, *Mater. Sci. and Technol.*, Vol 8, Jan 1992, pp. 52-56.

43 C. Chiu, J. D. Embury and T. Castillo, *Metallography*, 20, 1987, pp. 99-112.

44 D. A. Rigney and S. M. Kuo, *Materials Science and Engineering*, A157, 1992, pp. 131-143.

45 A. Somi Reddy, B. Pramila Bai, K.S.S. Murthy and S. K. Biswas, *Wear*, 171, 1994, pp. 155-127.

46 H. Torabian, J. P. Pathak and S. N. Tiwari, *Wear*, 172, 1994, pp. 49-58.

47 J. Yang and D. D. Chung, *Wear*, 135, 1989, pp. 53-75.

48 L. H. Chen and D. A. Rigney, *Wear*, 105, 1985, pp. 46-71.

49 D. A . Rigney, L. H. Chen, M. G. S. Naylor and A. R. Rosenfield, *Wear*, 100, 1984, pp. 195-219.

50 P. Helman, J. Don, T. C. Sun, D. A. Rigney and W. A. Glaeser, *Wear*, 91, 1983, pp. 171-190.

51 C. P. You, W.T. Donlon, J. M. Boileau, in P. K. Rohatgi, C. S. Yust, P. J. Blau (eds), *Proc. Conf. Tribology of Composite Materials*, Oakridge TN, May 1-3, 1990, ASM Int., 1990, pp. 157-167.49

52 C. A. Caracostas, W. A. Chiou, M. E. Fine, and H. S. Cheng, *Scripta Metall. et Mater.*, 27, 1992, pp. 167-172.

53 A. T. Alpas and J. Zhang, *Materials Science and Engineering*, March 1993, pp. 273-284.

54 Y. Pan, M. E. Fine, H. S. Cheng in *Tribology of Composite Materials*, P. K. Rohatgi, P. J. Blau, C. S. Yust (eds), ASM, Materials Park, 1990, pp. 93-101.

55 K. Anand and T. Kishore, *Wear*, 85, 1983, pp. 163-169.

56 B. P. Krishnan, N. Raman, K. Narayanaswamy and P. K. Rohatgi, Wear, 60, 1980, pp. 205-215.

57 D. Nath, S. K. Biswas and P. K. Rohatgi, Wear, 60, 1983, pp. 61-73.

58 P. R. Gibson, A. J. Cleg and A. A. Das, Mater. Sci. and Tech., July, 1985, pp. 559-567.

59 A. K. Jha, S. V. Prasad and G. S. Upadhaya, Trib. Int., 22, 1989, pp. 321-327.

60 S. V. Prasad and P. K. Rohatgi, *Journal of Metals*, 26, November 1987, pp. 22-26.

61 P. K. Rohatgi, S. Roy and Y. Liu, in *Tribology of Composite Materials*, P.K. Rohatgi, P. J Blau and C. S. Yust (eds), ASM, Materials Park, 1990, pp. 1-14.

62 S. Das, S. V. Prasad, T. R. Ramachandran, *Mater. Sci. Eng.* A138, 1991, pp. 123-132.

63 P. K. Rohatgi, Y. Liu and T. L. Barr, *Metall. Trans.*, 22A, 1991. pp. 1432-1441.

64 T. Iseki, T. Kameda and T. Maruyama, *J. Mater. Sci.*, 19, 1984, pp. 1692-1698.

65 D. J. Lloyd and B. Chamberlain, in S. G. Fishman and A. K. Dingra (eds), *Proc. Int. Symp. on Advances in Cast Reinforced Metal Composites*, Chicago, Sept 24-30, 1988, Asm Materials Park, OH, 1988, pp. 263-271.

66 J. C. Viala, P. Fortier, C. Bernard and J. Bioux in A. R. Bunsell, P. Lamicq and A. Massiah (eds), *Proc. 1st Eur. Conf. on Composite Materials*, ECCM-1, Bordeaux, France, Sept 1985, EACM, Bordeaux, France, pp. 583-588.

67 N. Wang, Z. Wang and G. L. Weatherley, in J. Masounave and F. G. Hamel (eds), *Proc. Fabrication of Particulate Reinforced Metal Composites*, Montreal, ASM International, Metals Park, OH, 1990, pp. 145-153.

68 L. Salvo, G. L. Esperance, M. Suery and J. G. Legoux, *Mater. Sci. and Eng.*, A177, 1994, pp. 173-183.

69 K. S. Prasad and Y. R. Mahajan, *Script. Metall. et Mater.*, Vol 30 No 8, 1994, pp. 1049-1054.

70 H. J. Dudek, A. Kleine, R. Borath and G. Neite, *Mater. Sci. and Eng.*, A167, 1993, pp. 129-137.

71 D. J. Lloyd, *International Materials Reviews*, Vol 39 No 1, 1994, pp. 1-23.

72 S. C. Lim and M. F. Asby, *Acta Metall.*, Vol 35 No 1, 1987, pp. 1-24.

73 M. A. Martinez, A. Martin and J. LLorca, *Scripta Metallurgica et Materialia*, Vol 28, 1993, pp. 207-212.

74 M. Taya and R. J. Arsenault, *Metal matrix Composites: Thermomechanical Behaviour*, Pergammon Press, New York, 1989, pp. 157-159.

75 S. Suresh, T. Christman and Y. Sugimura, *Scripta Metallurgica et Materialia*, 23, 1989, pp. 1599-1608.

76 Z. Y. Ma, X. G. Ning, Y. X. Lu and L. S. Wen, *Scripta Metallurgica et Materialia*, Vol 31 No 2, 1994, pp. 131-135.

77 M. Suery, C. Teodosiu and L. F. Menezes, *Mater. Sci. and Eng.*, A167, 1993, pp. 97-105.

78 M. Ferry and P. R. Munroe, *Scripta Metallurgica et Materialia*, Vol 31 No 2, 1994, pp. 143-148.

79 M. P. Thomas and J. E. King, *Scripta Metallurgica et Materialia*, Vol 31 No 2, 1994, pp. 209-214.

80 S. F. Corbin and D. S. Wilkinsin, *Acta metall. Mater.*, Vol 42 No 4, 1994, pp. 1311-1318.

81 A. Ball, The Mechanisms of Wear and the Performance of Engineering Materials, J. South African Institute of Mining and Metallurgy, 86, 1986, pp. 1-13.

82 A. T. Alpas and J. Zhang, *Wear*, 155, 1992, pp. 83-104.

83 M. D. Kulkarni, P. S. Robi, R. C. Prasad and P. Ramakrishnan, *Scripta Metallurgica et Materialia*, Vol 31 No 3, 1994, pp. 237-242.

84 R. O. Ritchie and J. K. Shang, *Metallurgical Transactions*, Vol 20 A, May 1989, pp. 897-907

85 H. J. Kim, T. Kobayashi and H. S. Yoon, *Mater. Sci. and Eng.*, A154, 1992, pp. 35-41.

86 A. Wang, H. J. Rack, *Wear*, 146, 1991, pp. 337-348.

87 S. Corbin and D. S. Wilkonsin, Acta Metall. et Mater., Vol 42 No 4, 1994, pp.1319-1327.

88 S. Corbin and D. S. Wilkonsin, Acta Metall. et Mater., Vol 42 No 4, 1994, pp. 1329-1335.

89 A. R. Rosenfield, *Wear*, 116, 1987, pp. 317-328.

90 A. Blomberg, M. Olsson and S. Hogmark, *Wear*, 171, 1994, pp. 77-89.

91 Y. Zhang, Y. Chen, R. He and B. Shen, *Wear*, 166, 1993, pp. 179-186.

92 A. P. Verma, B. Vishwanath and C. V. Kameswara Rao, *Wear*, 167, 1993, pp. 93-99.

93 Y. Brechet, J. D. Embury , S. Tao and L. Luo, *Acta Metall. et Mater.*, Vol 39 No 8, 1991, pp. 1781-1786.

94 T. W. Clyne and P. J. Withers, *An Introduction to Metal Matrix Composites*, E. A. Davis and I. M. Ward (eds), Cambridge University Press, Cambridge, 1993, pp. 294-302.

95 A. Misra and I. Finnie, *Wear*, 85, 1983, pp. 57-68.

APPENDIX 1

A1: Derivation of allowable wear rates.

Consider an automobile disc brake rotor with the following dimensions:

ϕ (diameter) = 260mm

ϕ of inside edge of wear track = 140mm

ϕ of outside edge of wear track = 250mm

Then: Area of wear track (one side) = $\pi(125mm)^2 - \pi(70mm)^2$

$= 0.034m^2$

$= 0.068m^2$ (both sides)

Allowable wear depth = 2mm (1mm per side)

$\therefore$ allowable wear volume = $0.068m^2 \times 0.002m$

$= 1.36 \times 10^{-4}m^3$

The allowable wear mass then, for the

aluminium MMCs, = $2800\ kg.m^{-3} \times 1.36 \times 10^{-4}m^3$

= 381 grams

Similarly, the allowable wear mass for cast iron = 938 grams

For a replacement interval of 40 000 km and an

average breaking pressure of 300 kPa:

allowable wear rate for aluminium MMCs = $381grams/(4 \times 10^7 m \times 3 \times 10^5 Pa)$

$= 3.18 \times 10^{-11}$ g. Pa-1. m-1

Similarly, the allowable wear rate for cast iron = 7.82×10^{-11} g. Pa^{-1}. m^{-1}

APPENDIX 2

Matrices and reinforcements – selected thermophysical properties

Material	Diameter (μm)	Young's modulus (GPa)	Poisson ratio	Tensile strength (GPa)	Density (Mg/m^3)	Melting point (K)	CTE (με/K)	Thermal conductivity (W/mK)
Matrices								
Al (1100)	–	70	0.33	0.17	2.7	933	23.6	230
Al–Cu (2024)	–	73	0.33	0.47	2.8	915	23.6	190
Al–Mg–Si (6061)	–	70	0.33	0.38	2.7	925	23.6	180
Al–Zn (7075)	–	72	0.33	0.57	2.8	925	22.0	130
Al–Li (8090)	–	80	0.33		2.55	930		
Cu (C10100)	–	117	0.34	0.22	8.9	1356	17.0	391
Mg	–	45	0.35	0.13	1.8	922	26.6	107
Fe (mild steel)	–	208	0.28	0.43	7.8	1810	17.2	60
Ti	–	110	0.36	0.24	4.5	1940	9.5	22
Ti–6Al–4V	–	115	0.36	0.95	4.4	1920	9.0	6
Zn	–	105	0.35	0.12	7.1	693	31.0	120
Ni	–	214	0.31	0.30	8.9	1728	13.0	89
Ni superalloy	–	214	0.31	1.30	7.9	1550	12.0	11
Pb	–	14	0.36	0.02	11.3	600	30.0	25
Reinforcements								
Single crystals (particles and whiskers)								
Al_2O_3	1–50	430	0.24		3.8	2313	7	~100
B_4C	1–50	480		2.1	2.5	2623		
Diamond		1000	0.07–0.25		3.2		0.5	600
SiC	1–50	450	0.17		3.2		4.0	~100
TiB_2		350–570	0.13–0.19		4.5		8.1	~100
TiC		230–400	0.19		4.9			
WC		>530			15.7			
SiC_w	0.1–1	450, <700	0.17	3.1, <21.0	3.2		4.0	>16
Si_3Ni_{4w}	0.1–10	350–385		2–4, <14	3.1	1600*		

APPENDIX 2 - CONT.

Material	Diameter (μm)	Young's modulus (GPa)	Poisson ratio	Tensile strength (GPa)	Density (Mg/m^3)	Melting point (K)	CTE (με/K)	Thermal conductivity (W/mK)
Reinforcements *(cont.)*								
Metallic wires								
Patented steel	100	220	0.28	4.2, <13.0	7.9	1800	13.3	29
W wire	25–380	405	0.29	1.7–3.9	19.3	3660	4.5	168
Spun fibres (multifilaments and staple fibres)								
Al_2O_3 (Saffil®)	3	285		1.5	3.5	1600*/ 2313	7.7	
Al_2O_3 (DuPont FP)	20	380		1.3–2.1	4.0	1650*/ 2313	8.3	
C pitch	5–13	380–690		2.0	2.0	700*/ 3950	−1.4 (axial) 10 (trans)	355 (axial)
C PAN (high strength)	7	230		4.8	1.9	700*/ 3950	−1.2 (axial)	
C PAN (high modulus)		412		2.4			10 (trans)	
SiC (Nicalon)	15	180		>2.4, 8.3	2.55	1095*/ 2700†	3.0	
Monofilaments (CVD fibres)								
B (CVD W core)	50–100	400		2.7–7.0	2.6	2300	5.0	~38
Borsic (CVD)	100	415		2.93	2.77	2600	5.0	38
SiC (C core CVD)	150	345		3.8	3.29	2700†	4.0	16
SiC (W core CVD)	100	415		3.8	3.29	900*/ 2700†	4.0	16